

The copyright of this thesis vests in the author. No quotation from it or information derived from it is to be published without full acknowledgement of the source. The thesis is to be used for private study or non-commercial research purposes only.

Published by the University of Cape Town (UCT) in terms of the non-exclusive license granted to UCT by the author.

**A descriptive analysis of the genesis and
translation of a dipole vortex from the
Agulhas retroflection region**

Christo Peter Whittle

Submitted in fulfilment of the requirements of
the Master of Science degree

Department of Oceanography
University of Cape Town

2000

Abstract

An anomalous leakage of Agulhas Current water into the south-east Atlantic Ocean, exhibiting a mushroom-like shape, was observed during routine observations of AVHRR satellite imagery in early December 1996. The development of this anomaly was followed on the sea surface temperature (SST) imagery and it was tentatively identified as a consequence of filament interaction between the Agulhas retroflection and an occluding Agulhas ring. This interpretation prompted a cruise onboard the F.R.S. Africana with the objective of conducting a hydrographic survey of the Agulhas ring and the associated filament near Cape Town.

A descriptive analysis, gleaned from AVHRR satellite imagery and in situ data, of the hydrographic characteristics of a vortex dipole, surveyed during this cruise, is presented in this thesis. An analysis of water mass properties and geostrophic flow patterns determined that an Agulhas ring and a cyclonic eddy, containing Benguela Current water in its core, constituted a dipole vortex in the south-eastern Atlantic Ocean. During the period of the hydrographic survey, the secondary vortex exhibited an anticlockwise rotation of $8.6^\circ/\text{day}$ around the Agulhas ring. A warm filament, originating from the western Agulhas Bank, was entrained between the two counter-rotating eddies, thus resulting in the mixing of Agulhas Bank water into the South Atlantic Ocean.

Satellite altimetry and AVHRR imagery were used to “backtrack” the vortex dipole to its origin at the Agulhas retroflection. By combining interpretations from the altimetry and AVHRR imagery, it was possible to describe the complex interactions the dipole displayed with the retroflection and the Agulhas Bank as it translated in a north-westerly direction. The mushroom configuration, identified earlier on SST imagery, betrayed the presence of an adjacent pair of circulatory features of opposing spin. As the dipole translated northward, it interacted with the Agulhas Bank and the cyclone was strained, becoming a filament as it was forced between the Agulhas ring and the Agulhas Bank. West of Cape Town the dipole was re-established when the cyclone redeveloped, changing the orientation of the dipole so that a filament was drawn directly from the Agulhas Bank.

Establishing the origin and translation of the dipole allows for the possibility to speculate on the impact that the presence of this vortex dipole might have had on the oceanography of its immediate surroundings.

Acknowledgements

Sincere appreciation is extended to my supervisor, Prof. Frank A. Shillington of the Department of Oceanography (U.C.T.), for his constructive criticism, guidance, financial support and continued assistance during the development of this thesis. Special thanks are extended to my co-supervisor, Dr. Chris M. Duncombe Rae of the Directorate of Marine and Coastal Management, for the provision of the hydrographic data and helpful hints in the processing thereof. Scarla Weeks of Oceanspace is also thanked for the training and assistance she provided in the processing of remotely sensed sea surface temperature data. I would also like to thank Prof. Johann R. E. Lutjeharms of the Department of Oceanography (U.C.T.) for insightful discussions about the Agulhas Current and Agulhas rings.

Finally, I would like to express my heartfelt thanks to Tracy-Lee and my family for their continuous patience, support and encouragement throughout the period of this study.

Contents

	Page No.	
Abstract	<i>i</i>	
Acknowledgements	<i>ii</i>	
Contents	<i>iii</i>	
List of Figures	<i>iv</i>	
Chapter 1	Rationale and Introduction	1
Chapter 2	Introduction to vortex dipoles	9
Chapter 3A	The Agulhas Retroflexion and associated features	21
Chapter 3B	Applications of Satellite Remote Sensing	33
Chapter 4	Instrumentation and Methods of Data Analysis	46
Chapter 5	Structure of surveyed dipole	53
Chapter 6	Origin of the dipole vortex	86
Chapter 7	Conclusions	106
	References	111
	Appendix I	127
	Appendix II	129
	Appendix III	133

List of Figures

Figures	Page No.
1.1 A conceptual image of the Agulhas retroflection and environment	3
1.2 A thermal infrared image portraying the dipole vortex and the associated filament being drawn from the Agulhas Bank.	5
1.3 A portrayal of the bathymetry around Southern Africa, showing the 200m, 500m and 1000m isobaths.	6
1.4 A thermal infrared image depicting a dipole vortex interacting with a Benguela upwelling filament.	7
2.1 Diagram of the initial velocity distribution in the upper ocean during the development of a localized momentum pulse into a dipole vortex.	12
2.2 A graph depicting the results of numerical experiments to simulate the evolution of a surface tracer in response to a localized momentum pulse.	13
2.3 The angular position of the secondary vortex with respect to WCR 82-B as a function of time.	16
2.4 A detailed rendering of dipole ring 82-B during the third rotation of the cyclone around the anticyclone.	18
2.5 Simulated deformation of surface isotherms due to a translating dipole.	19
3.1 Section depicting potential vorticity superimposed on the potential density for a cyclonic ring.	28
3.2 Schematic showing the functions of different classes of sensors used in satellite oceanography.	34
3.3 Outline of the procedures required for processing data received from satellites.	36
5.1 AVHRR SST Image of vortex dipole on 19 December 1996.	54
5.2 AVHRR SST Gradient Image on 19 December 1996.	56
5.3 AVHRR SST Image of vortex dipole on 20 December 1996.	57
5.4 AVHRR SST Gradient image on 19 December 1996.	58
5.5 Xcel diagram of relevant CTD and XBT stations.	63

5.6	Isotherms in 1°C intervals at 500m depth for the region surveyed by the F.R.S. <i>Africana</i> .	65
5.7	Depth of the 27kg/m ³ σ_θ surface in 50m contour intervals.	66
5.8	Vertical temperature and salinity sections for Transect 1.	68
5.9	Vertical potential density and geostrophic velocity sections for Transect 1.	69
5.10	Vertical temperature and salinity sections for Transect 2.	71
5.11	Vertical potential density and geostrophic velocity sections for Transect 2.	72
5.12	Vertical temperature and salinity sections for Transect 3.	74
5.13	Vertical potential density and geostrophic velocity sections for Transect 3.	75
5.14	Vertical temperature and salinity sections for Transect 4.	77
5.15	Vertical potential density and geostrophic velocity sections for Transect 4.	79
5.16	T-S diagram from CTD stations representative of the dipole.	82
6.1	AVHRR image showing the Agulhas Current and retroflexion region on 5 December 1996.	87
6.2	AVHRR SST image showing a meander in the retroflexion region on 4 December 1996.	89
6.3	AVHRR SST image showing ‘mushroom-shape’ in retroflexion region on 5 December 1996.	90
6.4	AVHRR SST image showing collapse of mushroom structure on 7 December 1996.	91
6.5	AVHRR SST image showing occluding Agulhas ring and filament interactions on 9 December 1996.	92
6.6	AVHRR SST image showing Agulhas ring entraining a cool filament (deformed cyclone) on 10 December 1996.	93
6.7	AVHRR SST image showing Agulhas ring and redeveloping cyclone on 13 December 1996.	94
6.8	Sea surface height anomaly for the southeast Atlantic region on 2 December 1996.	96
6.9	Sequence of SHA images for the southeast Atlantic region.	98

Chapter 1

Rationale and Introduction

Rationale

A considerable, but not as yet unambiguously quantified (e.g. *Rintoul 1991*), exchange of oceanic water takes place between the subtropical gyres of the South Indian and South Atlantic oceans. It has been shown that the major part of this exchange is through the transfer of warm salty, Subtropical Surface Water from the southern termination of the Agulhas Current (*Gordon et al., 1987*).

Routine observation of sea surface temperature satellite imagery resulted in the discovery of an anomalous leakage of Agulhas Current water from a meander in the Agulhas retroflexion region. This feature could be interpreted as an anomalous formation of an Agulhas retroflexion eddy. The development of this feature was monitored by scientists from the University of Cape Town and the Department of Marine and Coastal Management (also based in Cape Town). During mid-December 1996 a circular eddy structure, as well as the associated removal of water from the Agulhas Bank region, could be discerned. On 19 December 1996 the FRS *Africana*, a Marine and Coastal Management research vessel, left Cape Town on a four day journey under the leadership of chief scientist Dr Chris Duncombe Rae. By then the anomalous feature, identified in early December 1996, had developed into an Agulhas ring, exhibiting complex filament interactions with the Agulhas Bank region (*Figure 1.2*). The aim of the cruise was to conduct a hydrographic survey of an Agulhas ring and a related warm filament.

An analysis of the cruise data and scrutiny of the sea surface temperature satellite imagery alluded to the presence of an Agulhas ring and an adjacent cyclonic ring west of Cape Town. Such an eddy pairing would be an example of a dipole vortex in the south-east Atlantic Ocean. The main objective of this thesis is to use satellite remote sensing data and *in situ* cruise data to understand the evolution of an Agulhas Ring into a dipole

pairing. During the course of this investigation the following hypotheses will be examined:

1. Can the hydrographic data from the cruise establish that the dipole structure observed in *Figure 1.2* is reflected in the water column? This question will be answered by investigating vertical temperature, salinity, density and geostrophic flow sections along the cruise track.
2. Can infrared satellite SST (sea surface temperature) imagery reveal structure that is not evident from the *in situ* data? Is there an interaction of the dipole with an Agulhas Current filament and also with Agulhas Bank water?
3. Can selected daily infrared SST satellite imagery from the three-week period preceding the cruise, trace the origin and translation of the dipole?
4. Can altimetry imagery be trusted to provide a reliable representation of features around the retroflexion region, and hence provide some insight into the questions left after the examination of the AVHRR data?

Once the origin and translation of a dipole from the retroflexion region has been established, it will be possible to speculate on the impact that the presence of a vortex dipole would have on its surrounding oceanographic environment and the biota resident in that environment.

Introduction

This section will provide a brief overview of the Agulhas Current and its associated features, as well as a description of the features surveyed by the FRS *Africana*. It will also provide some insight into the relevance of Agulhas eddy and shelf water interaction to the biota of the West Coast.

The Agulhas Current (*Figure 1.1, feature A*) is the western boundary current of the South Indian Ocean and it forms an important conduit in the global ocean circulation, linking the Indian and Atlantic Oceans (*Gordon et al., 1992*). It flows along the south-

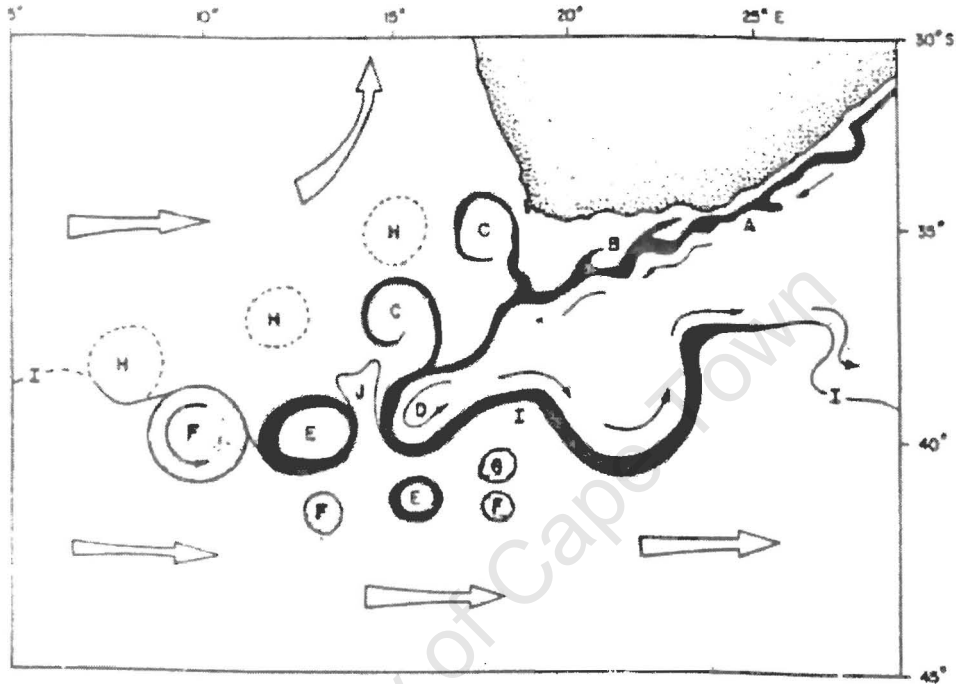


Figure 1.1: *A conceptual image, based on 7 years of satellite imagery and XBT sections, of the Agulhas retroflexion and environment. Broad open arrows show mean drift patterns, while solid arrows show the current direction in the southern reaches of the Agulhas Current. Lettered features are explained in the text. (From Lutjeharms and Van Ballegooyen 1988a.)*

eastern coast of Africa from Mozambique, guided by the continental shelf. Near 36°S, at the Agulhas Bank, it separates from the continental shelf as a free jet, develops oscillations of increasing amplitude (*Lutjeharms, 1981a*) (**feature B**) and turns eastward in a great anticyclonic loop, named the Agulhas retroflexion (**feature D**) by *Bang (1970b)*. In general, the retroflexion occurs between 20°E and 15°E (*Lutjeharms, 1996*) and the current then returns to the Indian Ocean as the Agulhas Return Current. The

retroflexion loop is unstable and the loop occludes (**feature J**) at intervals of about two months (*Lutjeharms and Van Ballegooyen, 1988a; Feron et al., 1992*), thus pinching off rings of warm water (**feature E**) that drift into the South Atlantic Ocean (**feature F**). **Features H** represent older Agulhas rings no longer evident by surface thermal expressions and **feature I** represent the Subtropical Convergence. Agulhas rings not only transfer warmer and saltier waters into that region, but are also a source of kinetic and potential energy (*Olson and Evans, 1986*). In addition, they affect their immediate surroundings in the Southeast Atlantic Ocean through interaction with filaments (*Duncombe Rae et al., 1992b*).

A minor contribution to the inter-basin exchange of the water at the retroflexion region is made by the advection of Agulhas current filaments (**feature C**) into the South Atlantic (*Lutjeharms and Cooper, 1996*). As seen in *Figure 1.1*, Agulhas filaments can delineate Agulhas rings that have lost their thermal expression providing some insight into the ring's location and dimensions (*Lutjeharms and Gordon, 1987*). Agulhas filaments are long streaks or tendrils of warm water formed from the Agulhas Current (*Lutjeharms and Cooper, 1996*). Their genesis is a consequence of the horizontal shear between the Agulhas Current and the relatively quiescent water over the Agulhas Bank (*Lutjeharms and Cooper, 1996*).

Figure 1.2 is an infrared image that represents the sea surface temperature, in false colour, and the cruise track of the FRS *Africana* for the period 19 to 23 December 1996. This image provides an overview of the Southern Benguela Upwelling region, the South-east Atlantic Ocean and the Agulhas Bank, thus visually illustrating the impact this particular Agulhas ring had on these three regions. Over the temperature range of 18°C to 21°C the colour palette applied to this image has been divided into quarter degree bins, thereby highlighting the eddy-filament interaction. Due to the scope of the area represented in the image, only certain CTD stations could be illustrated here. The positions of all CTD and XBT stations are accurately depicted in Chapter 5. It is evident from the cruise track that the northern edge of the anticyclonic Agulhas eddy, the entrained filament and a cyclonic eddy to the north of the Agulhas eddy were surveyed.

Together, the Agulhas ring and the cyclonic eddy form a dipole vortex that is drawing a warm filament from the western Agulhas Bank region. Plankton was also sampled during the cruise to aid in the determination of the origin of the filament water. The data from the hydrographic survey was then used to investigate the influence of the Agulhas eddy and shelf water interaction on the biota of the West Coast.

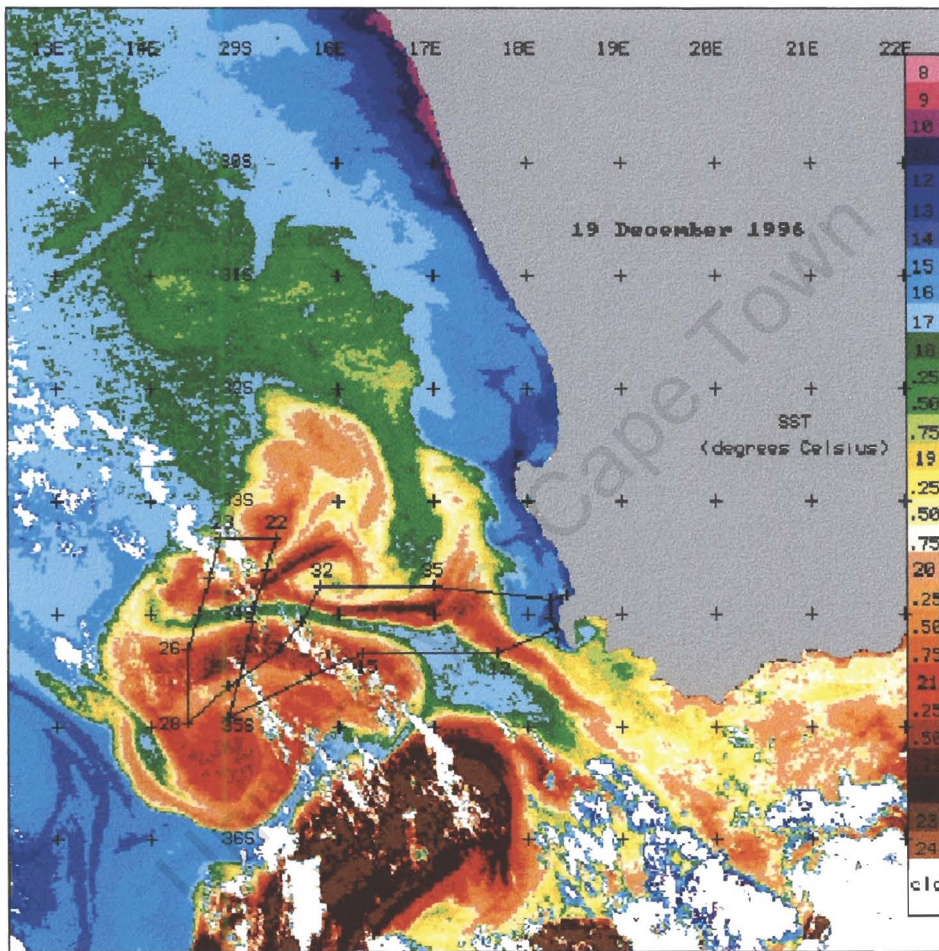


Figure 1.2: *A portrayal of the surface expression (SST) of the dipole vortex and the associated filament being drawn from the Agulhas Bank. It is a thermal infrared image for 19/12/1996 from the AVHRR on board NOAA 14.*

Pelagic fish (e.g. Anchovy) in the Southern Benguela Upwelling region (water $<14^{\circ}\text{C}$ on the West Coast in *Figure 1.2*) spawn on the Agulhas Bank, are hatched and the larvae transported north along the West Coast shelf in narrow shelf-edge currents. The larvae

develop and grow in the vicinity of the Orange River mouth and St Helena Bay, and eventually return inshore to the Agulhas Bank to breed again. *Figure 1.3* provides the locations of these three regions. Six-month-old juveniles recruit to the West Coast fisheries in the St Helena Bay region (*Armstrong and Thomas, 1989*). Spawning success of Cape anchovy *Engraulis capensis* is influenced by food availability on the western Agulhas Bank (*Cochrane and Hutchings, 1995*) where copepods serve as their major food source (*James 1987*). Advective losses off the western Agulhas Bank, similar to the scenario depicted in *Figure 1.2*, may influence the biomass of copepods (*Richardson et al., 1998*). In some instances the advective loss from the western Agulhas Bank may be greater than the advective input from the eastern Agulhas Bank (*Largier et al., 1992, Peterson et al., 1992*). It is thus reasonable to suggest that a scenario similar to that depicted in *Figure 1.2* could impact negatively on the spawning success of Cape anchovy.

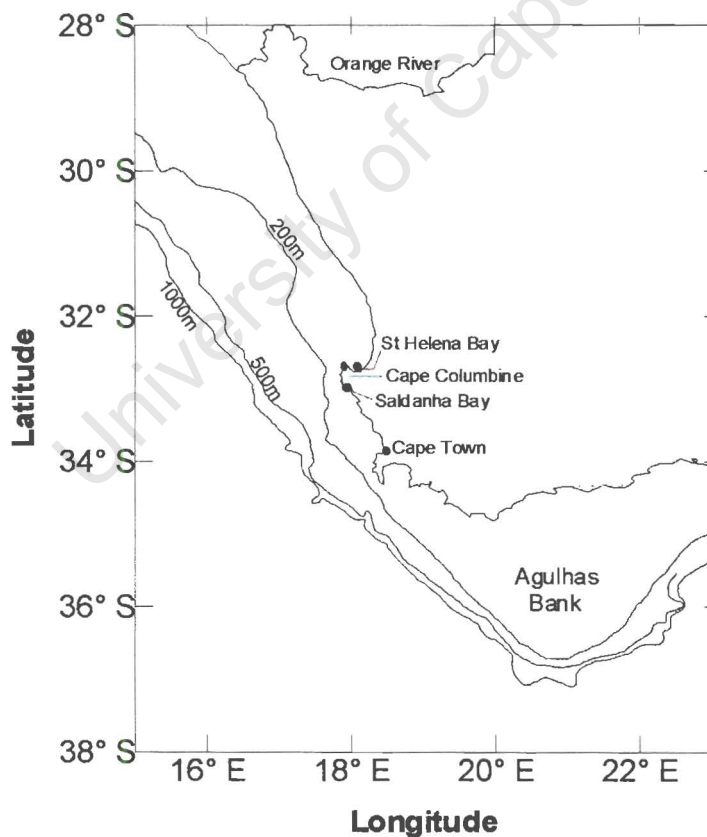


Figure 1.3: *A portrayal of the bathymetry around southern Africa, showing the 200m, 500m and 1000m isobaths.*

Duncombe Rae et al. (1992a, b) investigated an eddy-filament interaction in the Benguela upwelling regime. Using satellite remote sensing resources, they were able to determine the Agulhas origin of the anticyclonic eddy. The AVHRR image (*Figure 1.4*) used in their study illustrates a remarkably similar sea surface tracer (sea surface temperature)

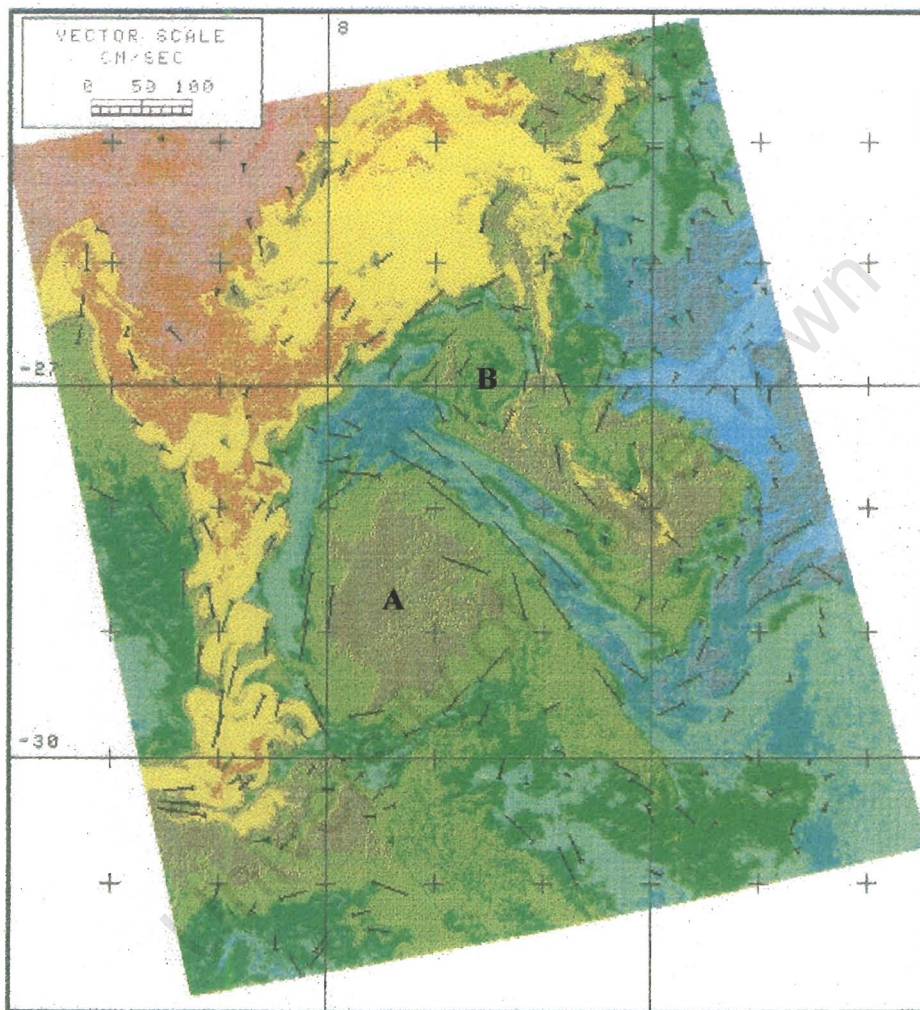


Figure 1.4: NOAA-11 single channel infra-red image for 15 June 1989 with surface current vectors from feature tracking with two images approximately 24 hours apart. Blue to green represents lower temperatures and yellow to red represents higher temperatures. (From Duncombe Rae et al., 1992b)

pattern to *Figure 1.2*. Although the location is further north, the image in *Figure 1.4* also depicts an Agulhas Ring (marked **A**) with a concomitant cyclonic eddy (marked **B**), as

well as a filament, originating from the Benguela Upwelling system, being drawn between them. A “mushroom-shaped” or “T-shaped” structure is formed by the filament as it envelops both eddies. *Mied et al. (1991)* describe dipole vortices as exhibiting a “mushroom-shaped” structure in the presence of a surface tracer (such as sea surface temperature). The “mushroom-shaped” structure, identified in *Figure 1.4*, thus infers the presence of a dipole vortex, with an Agulhas Ring as the primary vortex, in the South-east Atlantic Ocean. *Duncombe Rae et al. (1992a)* contend that this particular eddy-filament interaction could have contributed to anchovy recruitment failure in 1989.

Figure 1.4 illustrates the point that dipole vortices could easily go unnoticed on an AVHRR image in the absence of a delineating warm or cool filament. Far from the retroflection region, the surface water of an Agulhas ring would have cooled considerably and often the rings are indistinguishable from their surroundings when looking at their sea surface temperature alone. *Hooker et al. (1995b)* used remote sensing and *in situ* data to examine the dipole nature of a warm core Gulf Stream Ring and found that the observed dipole was a coherent structure that was stable despite interactions with the Gulf Stream and the continental shelf. They also suggested that dipoles should occur, under favourable conditions for their formation, in other major current systems.

In the ensuing chapters a literature review is presented of scientific investigations and observations relevant to dipole vortices. A review of information concerning the Agulhas retroflection and associated features, as well as the examination of the Agulhas retroflection region and Southern Benguela upwelling regime using satellite imagery, is also presented. This is followed in Chapter 4 by a description of the instruments that were used to collect the data analysed for this project and the methods employed for processing of the data. In Chapter 5 hydrographic and satellite evidence is presented which confirm the hypothesis that a dipole vortex was indeed surveyed by the scientific team onboard the FRS *Africana* in December 1996. AVHRR and altimeter data are used in Chapter 6 to trace the translation of the dipole from its origin. Finally the conclusions drawn from the analysis of the data presented in this thesis are put forward.

Chapter 2

Introduction to Vortex Dipoles

Visible and infrared satellite remote sensing of the ocean surface has allowed for the production of false-colour images that have provided large-area synoptic views unavailable with previous ship-borne *in situ* sampling techniques. It was found that ocean colour, floating ice, and sea surface temperature (SST) served as convenient tracers that delineate the motion of the fluid at the top of the water column. Dipole vortices are an example of surface features that are not easily detected using *in situ* surveys, but have been observed on satellite imagery. This chapter provides background information on dipoles with respect to their geographical occurrence, their genesis and their dynamics.

Geographical Occurrence

Ocean dipole vortex structures have a wide spread occurrence and many observations of these phenomena have been made. In all cases strong gradients in surface variables made their identification in satellite imagery feasible. *Simpson and Lynn (1990)* observed a vortex dipole near the California Current, while *Johannesen et al. (1989)* observed a similar eddy pair in the Norwegian Coastal Current. Paired vortices have also been found in such diverse locations as near Vancouver Island (*Ikeda and Emery, 1984*), off the Santa Barbara Channel (*Sheres and Kenyon, 1989*), north of the Gulf Stream (*Kenelly et al., 1985; Hooker and Brown, 1994*), in the Alaska Coastal Current (*Ahlnas et al., 1987*), and in the marginal ice zone (*Federov and Ginzburg, 1986*). Observations of vortex dipoles have also been made in the Benguela Upwelling Front (*Stockton and Lutjeharms, 1988*), as well as in the so-called Mozambique Ridge Current (*Gründlingh, 1988*). These structures have also been observed delineated by warm Agulhas Filaments penetrating the South Atlantic Ocean (*Lutjeharms and Walters, 1985*). In all cases strong gradients in surface variables made their identification in satellite imagery feasible.

Genesis of dipole vortices

According to *Mied et al. (1991)* the fundamental paired eddy structures and their surface signatures can have at least two causes:

- Closely spaced eddies with opposite-signed vorticity can emerge from the baroclinic instability of a coastal current (*Ikeda et al., 1984*).
- The occurrence of dipoles could be a universal reaction of a rotating fluid to an impulse that introduces relative angular momentum of both signs into the upper ocean (*Federov and Ginsourg, 1986*). Examples of such momentum sources would be local dynamic instabilities of frontal currents, local winds that are channeled by coastal geometry and topography, and water exchange through straits.

Several other researchers have also sought to explain the physics responsible for vortex dipole generation by investigating the results of laboratory experiments and numerical simulations. The impulsive injection of fluid in rotating tanks has been shown to generate paired vortices in the laboratory (*Flierl et al., 1983; van Heijst and Flor, 1989; Kloosterziel et al., 1983*). Numerical simulations offer considerably more flexibility in the design of experiments, however, and robust dipoles have been generated in various ways:

- through non-linear interaction (*McWilliams and Flierl, 1979; Mied and Lindemann, 1979, 1982; McWilliams, 1983*),
- by current instability (*Flierl et al., 1987; Smith and Bird, 1991*),
- by the interaction of currents with topography (*Haidvogel et al., 1991; Hofmann et al., 1991; Signell and Geyer, 1991*), and
- by impulsively applied stress, either to the water directly (*Mied et al., 1991*) or in the marginal ice zone (*Ikeda, 1991*).

These citations illustrate the variety of physical situations that can be responsible for the observations of dipoles in the ocean.

Mied et al. (1991) describe the surface signature of a vortex dipole, in the presence of a surface tracer like SST, as “mushroom-like”. Similar second-generation structures

originating from the basic mushroom shape have also been observed. For example, *Ahlnas et al. (1987)* have observed smaller off-spring mushrooms being generated on the cyclonic branch of the vortex pair. Similarly, both *Federov and Ginsberg (1986)* and *Ahlnas et al. (1987)* show examples of dipoles that are so densely packed that two adjacent vortex pairs share an eddy and thus respective mushroom caps are interlocked.

A mature dipole is a nearly steady-state flow structure [i.e., a modon (*Stern, 1975; Larichev and Reznik, 1976*)] that carries its interior fluid with it as it propagates. This implies that the tracer pattern representing a mature dipole will be either lobes (the recirculating fluid in the interior) or streamers (the exterior fluid being swept around the advancing dipole), not mushrooms with a stem and cap. Thus mushroom-like patterns seem more likely to result from the immature, or generation stages of a dipole and its tracer advection.

The evolution of a mushroom-like formation can be illustrated by an impulse-generation scenario; where the vortices arise from momentum of the near surface stratified ocean. *Federov and Ginzburg (1986)* note that there are two stages of evolution of these dipole flows. The first is a rapid phase of geostrophic adjustment, and the second represents a slower time-scale expansion of the newly formed vortex pair. Geostrophic balance might still not be achieved after the adjustment period because the cyclostrophic term could be important in the balance as well (*Johannessen et al., 1989*).

Mied et al. (1991) investigated the development of a localized momentum impulse, with no balancing density field, into a pair of eddies of opposite sign via a nonlinear geostrophic adjustment process. *Figure 2.1* illustrates the initial conditions considered by the authors. They employed both analytical techniques and numerical calculations on a two-layer periodic channel on an f -plane. The concomitant evolution of the surface tracer (which could represent sea surface isotherms as they appear on a remote sensing image) into a configuration which can resemble a mushroom was examined. Four parameters governing this process were found:

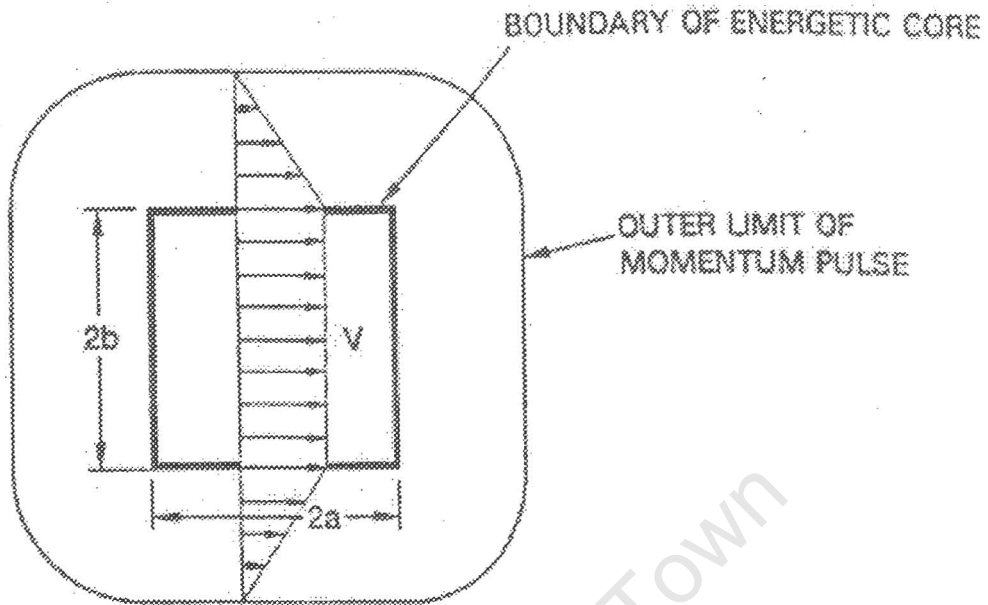


Figure 2.1: *The initial velocity distribution $u_1(x, y, 0)$ in the upper ocean. At the beginning of the experiment, the lower layer is at rest and the interface displacement is at zero.*

- The aspect ratio (α) of the initial momentum patch, i.e. $\alpha = b/a$ (refer to figure 2.1). The authors discovered that the mushroom formation process was associated with the forward portion of the momentum patch. Changing the aspect ratio had little qualitative effect upon the process, so $\alpha = 1$ was adopted for the results reported in *Mied et al. (1991)*.
- The ratio of the layer thickness (H_1/H_2). The authors made the assumption that typical mushroom currents are confined to the region above the seasonal thermocline (≤ 100 m) and hence made the modeling choice that $H_1/H_2 \ll 1$. As a result of this assumption, the model operates in the reduced gravity regime (i.e., where the flow in the lower layer is not of primary importance).
- The initial Rossby number (R_0), where

$$R_0 = \frac{U}{2bf}$$

- The ratio of the patch length scale to the deformation radius (λ), where

$$\lambda = \frac{2b}{R_d},$$

$$R_d = \frac{1}{f} \left(\frac{g'H_1H_2}{H_1+H_2} \right)^{1/2}, \text{ and}$$

$$g' = g \frac{(\rho_2 - \rho_1)}{\rho_2}$$

The latter two parameters have been varied in experiments, and the tracer response can be markedly different, depending on the values of R_0 and λ . Three regimes were observed (Fig. 2.2).

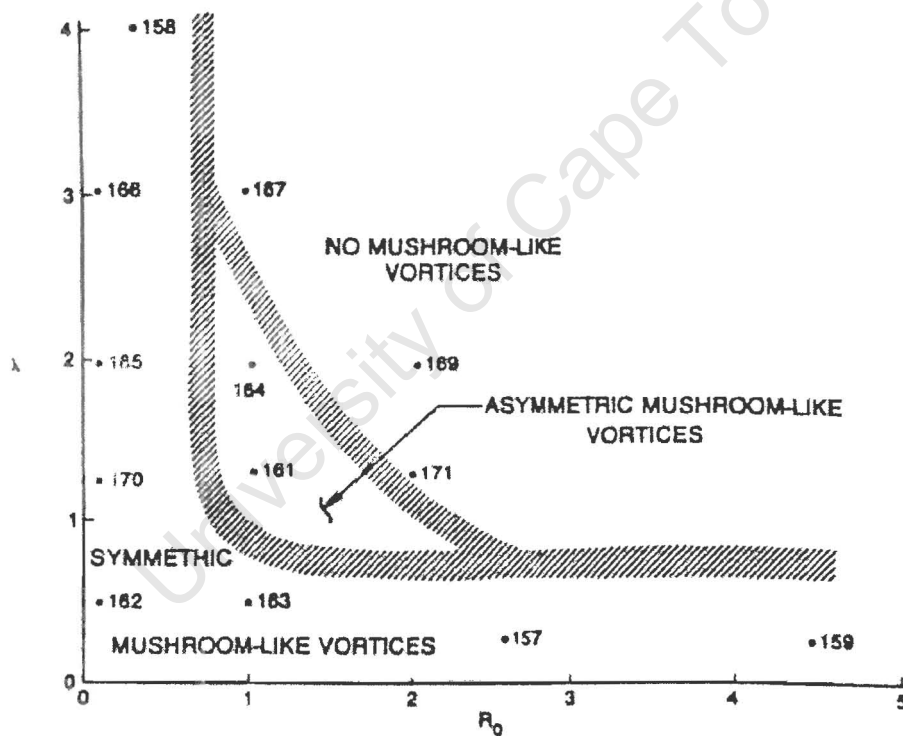


Figure 2.2: The distribution of experiments in the λ, R_0 plane. The aspect ratio is fixed at $\alpha = 1$ and $H_1 \ll H_2$ always. The lines separate the regions of symmetric and asymmetric mushroom formation from that where mushrooms are not formed. (From Mied et al., 1991.)

- *Symmetric mushroom currents.* These occur for $R_0 \leq 1$ or $\lambda \leq 0.5$. The smallness of λ indicates that gravity-wave radiation is important and that the balance is geostrophic versus gradient wind because centripetal forces are negligible.
- *Asymmetric mushroom forms.* These occur for $R_0 \geq 1$ and $\lambda \geq 1$. Large λ implies that potential vorticity (q) is dominated by h_1 , which is symmetric. Potential vorticity is defined as being equal to

$$q_1 = \frac{\nabla \times v_1 + f}{h_1},$$

in the upper layer. Since the gradient wind balance then requires the vorticity (hence the tracer) to be asymmetric, the mushroom is asymmetric. In addition, the asymmetry in the tracer pattern is augmented because radiated gravity waves preferentially modulate the cyclonic vorticity centre so that no persistent cyclonic vortex to advect the tracer can be identified during the period $T \leq 1$.

- *Non-stationary behaviour without a mushroom response.* Stationary, nonlinear solutions do not seem to exist for the upper right hand portion of the R_0 , large λ plane. Large R_0 , large λ cases frequently reduce the upper layer thickness to zero.

The authors have also compared the dynamics of both linear and nonlinear adjustment problems after initiation. They reached the following conclusions:

- The radiated waves have a spiral appearance in both cases, but the advective terms present in the nonlinear case steepen the waves significantly compared with the linear case.
- The eddies in the linear solution lack the ability to advect one another so that they experience a shape change in interface displacement (but not in potential vorticity) and exhibit no bulk motion while the adjustment occurs. In contrast, the nonlinear vortices can advect one another before the adjustment is complete.
- The linear solutions always have equal and opposite circulations. Conversely, the anticyclonic vortex can be stronger in the nonlinear simulations, with implications for vortex pair motion, and tracer advection.

The work of *Mied et al. (1991)* focused on the generation and evolution of single mushroom forms from momentum patches, but a further investigation of cyclonic/anticyclonic interaction, after complete dipole formation, is required.

Dipole Vortex Dynamics

The Gulf Stream ring 82-B was the principal subject of the Warm Core Rings Experiment (WCRE) during the northern hemisphere spring and summer of 1982 [*Warm Core Rings Executive Committee, 1982*]. Satellite imagery collected during the WCRE showed that secondary vortices around the periphery of the ring are a common feature of the slope water (*Evans et al., 1984*). The combination of the WCRE and other studies (*Thompson and Gotthardt, 1971*) assisted in the characterization of the behaviour and structure of these secondary cyclones or ringlets (*Kennelly et al., 1985; Nof, 1983*).

The then existing information on cyclonic ringlets were presented by *Hooker and Brown (1994)* as follows:

- Cyclonic ringlets seem to be generated by instabilities in the warm core ring or result from encounters between the ring and its environment: bottom topography, the continental shelf and the Gulf Stream. After formation, the eddy is entrained in the ring's circulation field and swept around the periphery of the ring, modifying the ring's translation and evolution.
- Secondary vortices vary in size, but they are roughly circular with a diameter of 40 - 50 km and swirl velocities of approximately 50 cm/s.
- Ringlets appear to have lifetimes less than the period of time required to make one revolution around the warm core ring. The ring and ringlet represents a dipole system, and this dipole configuration enhances the entrainment of neighboring fluid between eddy centres. Entrained fluid is then taken up by the large-scale circulation of the vortical system.

Hooker and Brown (1994) used SST satellite imagery, from data collected by NOAA's AVHRR on board the NOAA 7 satellite, drifter trajectories, and hydrographic profiles to

reinterpret the dynamics of warm core ring 82-B. Their method of analysis included the use of a hybrid zebra palette. The zebra palette combines a rainbow palette with a high-frequency, grey scale sinusoid centred on the colour transitions to provide distinct boundaries between temperature regimes. This technique was applied to a time series collection of SST satellite imagery that depicted the life history of ring 82-B. Observations concerning flow field rotation, or evidence for closed circulation, were made from the examination of this time series.

The authors tested the applicability of a dipole model by estimating the center of the cyclone as a function of time in a translating reference frame. If the dipole model is applicable, the angular rotation rate ($\Delta\theta/\Delta t$) of the cyclone around the anticyclone should be a constant (Fig. 2.3).

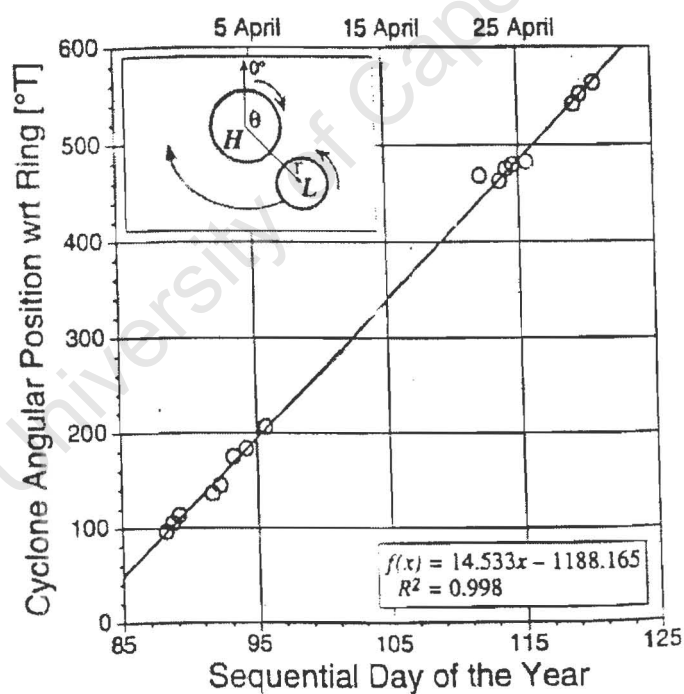


Figure 2.3: *The angular position of the cyclone with respect to the anticyclone (θ) as a function of time. (From Hooker and Brown, 1994.)*

This condition was found to hold for the ring *Hooker and Brown (1994)* were investigating. The primary conclusion from their investigation was that warm core ring 82-B is a dipole for much of its existence. This dipole nature is not due to episodic shelf break interactions which produce a cyclone that is captured then lost, but rather it is due to 82-B being fundamentally a dipole.

Vortex modeling by *Hooker and Brown (1994)* indicated that the weaker eddy in an unequal dipole, free from the influence of a boundary, will undergo a cycle of filamentation followed by axisymmetrization, which is repeated twice for each revolution of the secondary vortex around the primary. Axisymmetrization refers to the cyclone and anticyclone exhibiting unequal symmetry about a common axis. During the cycle of filamentation the cyclone is strained to the point where it has lost much of its eddy structure, i.e. it is drawn into a filament (*Figure 2.4(d)*). If an unequal dipole is initialized close to a boundary with the cyclone opposite the anticyclone and furthest from the boundary, the double cycle of filamentation and axisymmetrization is broken. The proximity of the boundary forces the filamentation of the cyclone when it is pulled through the gap between the anticyclone and the boundary. Ultimately the cyclone is thus only visible 25% of the time and the primary effect of the boundary, then, is to increase the expression of filaments.

Ring 82-B was observed to rotate over a time interval of two months and it was sufficiently robust to survive at least one interaction with the Gulf Stream, and several interactions with the continental shelf. *Hooker et al. (1995b)* suggest that the phenomena's resistance to disruption indicates that the observed dipole is a coherent structure that is stable to large-amplitude perturbations. Upon the re-examination of the data concerning warm core ring 82-B for the period April 22-30 1982, *Hooker et al (1995b)* showed how a barotropic rotating dipole could be constructed from the remote and *in situ* data. The authors incorporated the theory devised by *Mied et al. (1992)* to calculate a material line distribution (surface tracer) for a translating and rotating dipole. They found that a rotating barotropic modon (*Mied et al., 1992*) can be constructed with the same dipole rotation rate, centre-to-centre vortex separation distance, and peak

anticyclonic vorticity as that of warm core ring 82-B (see *figures 2.4 and 2.5*). The resulting tracer pattern is remarkably similar to that seen in the imagery. Note the compression of the isotherms in both figures, causing the primary vortex to have a slightly “D-shaped” appearance with the flattened edge facing the secondary vortex.

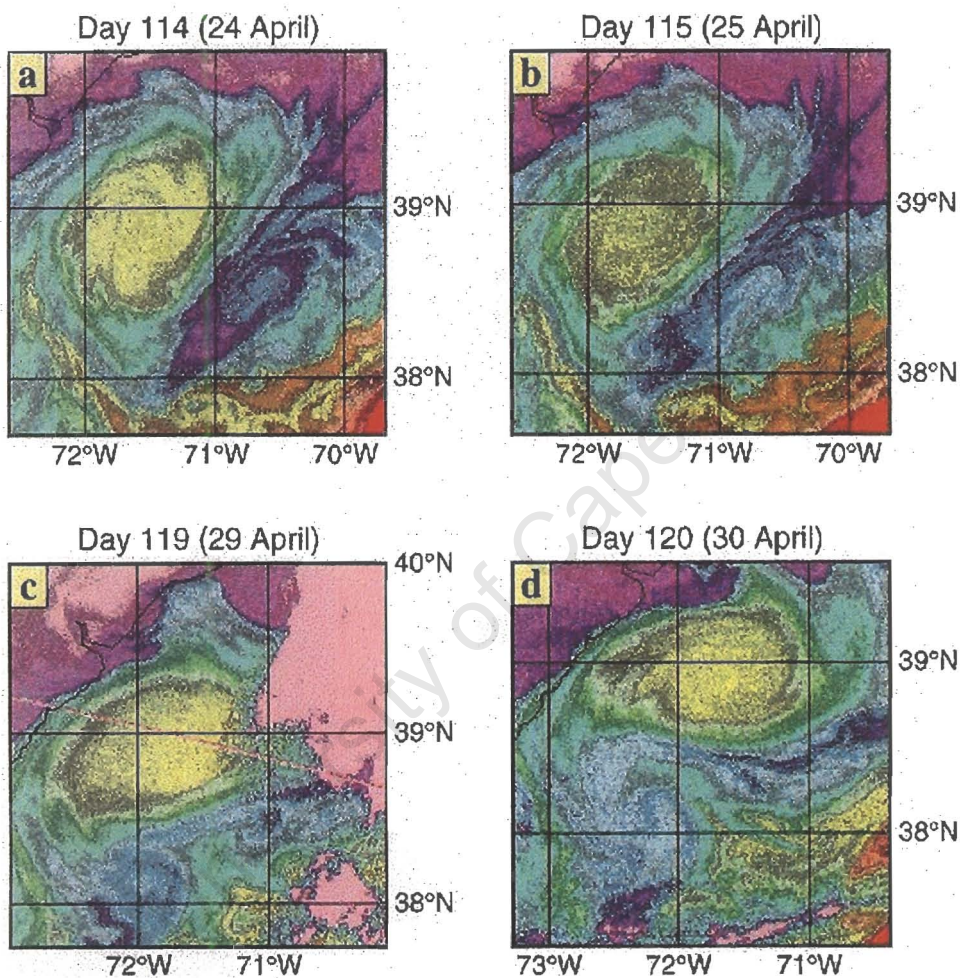


Figure 2.4: *A detailed rendering of dipole ring 82-B during the third rotation of the cyclone around the anticyclone. The sequence begins right after the start of the axisymmetrization phase (a and b) and ends during the latter part of the deformation phase (c and d), just before filamentation. The sea surface temperature is represented by the zebra palette; blue and green representing cooler water, and red and yellow representing warmer water. (From Hooker et al., 1995b.)*

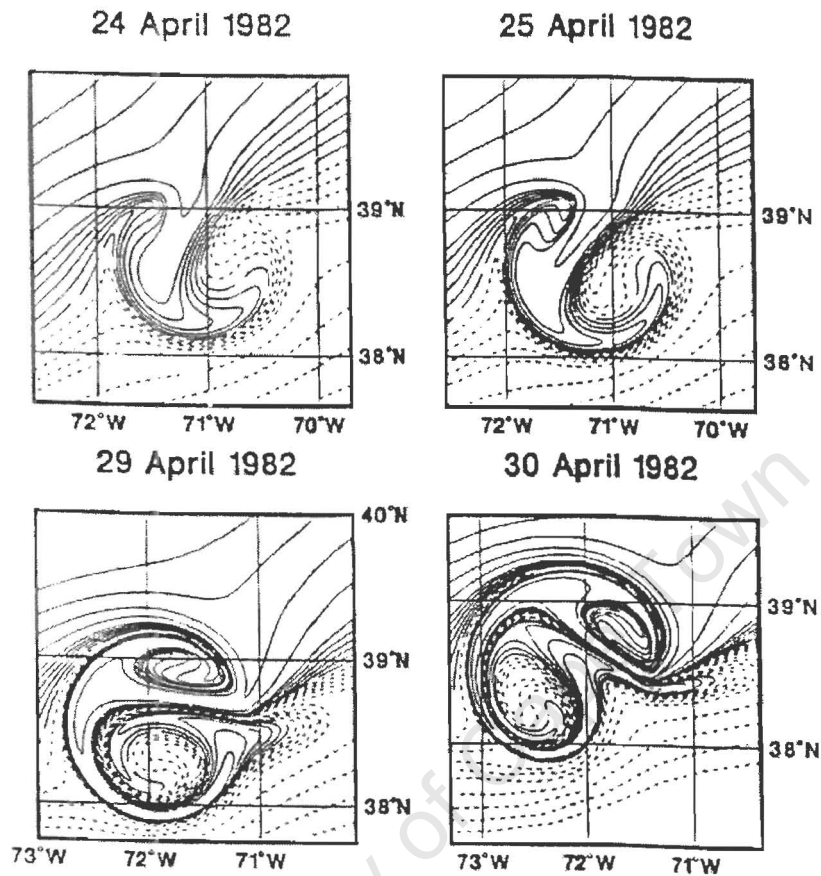


Figure 2.5: *Deformation of the isotherms (surface tracer pattern) due to a translating dipole. The times of the simulation are in keeping with the images portrayed in Figure 2.4. On April 24 the anticyclone is the eddy to the west, and the cyclone is to the east. The line weights for the isotherms were arbitrarily chosen to divide the fluid into onshore (shelf) and offshore (slope) components, showed by solid and dashed lines respectively. (From Hooker et al., 1995b.)*

The authors concluded that the combination of shape, trajectory and material line deformation observations constituted a body of evidence which would mitigate against the interpretation of the cyclone as a transient Rossby wave wake by a monopole, i.e. the cyclone on the periphery of ring 82-B is inherent to the dipole vortex structure of 82-B. Their work demonstrates the potential of using image data to quantify surface flow

characteristics for use in feature models and suggests that some rather simple dynamics may be responsible for some of the more complicated features seen in the images.

Furthermore *Hooker et al (1995b)* suggest three possibilities for the origin of the vortex dipoles:

- If the warm core ring were monopolar and unstable at birth, ample theoretical evidence exists to suggest that a mode of instability could be a pair of dipoles (e.g., *Ikeda, 1981; McCalpin, 1987; Flierl, 1988; Helfrich and Send, 1988*).
- If the detached monopole is in the vicinity of the Gulf Stream, *Smith and Davis (1989)*, and *Bell and Pratt (1992)* have shown examples of a monopole detaching a pool of oppositely signed vorticity from the jet to create a dipole.
- *Flierl et al. (1987)* have discovered that dipoles can result directly from the instability of a barotropic β plane jet.

Although specific initial conditions are required for all three of the origin possibilities, they do indicate that a number of situations can readily produce a dipole. *Hooker et al. (1995b)* showed that both cold core and warm core dipole rings exist and further suggested that the presence of cold core dipole rings would imply that topography is not responsible for dipole configuration. However, they still maintain that topography does play an important role in the interaction with an already existing dipole.

Although the examples of possible dipole formation and dynamics cited in this chapter refer mostly to Gulf Stream rings, it is important to bear in mind the similar formation processes of rings in other western boundary currents. It is thus reasonable to expect that, under favorable conditions, dipole vortices should occur in other major current systems such as the Agulhas, Kuroshio, Brazil and East Australian Currents.

Chapter 3

This chapter is divided into two sections. Section A is devoted to the provision of background information about the Agulhas Retroflection region and its associated features. It is followed by Section B that covers a short overview of the processes involved in obtaining remotely sensed data, as well as the use of such data in the investigation of the Agulhas Retroflection region and Southern Benguela upwelling regime.

Section A

The Agulhas Retroflection and associated features

In order to analyze the satellite and hydrographic data used in this project, a thorough background knowledge of the kinematics and nature of the Agulhas retroflection region and its associated features is required. This review serves to summarize current knowledge of Agulhas rings with respect to their source, formation and impact on the local oceanography.

The Retroflection

The Agulhas Current retroflection essentially consists of the anti-cyclonic loop formed by the Agulhas Current westward of the southernmost tip of the Agulhas Bank. The retroflecting behaviour of the current may be modeled as a free inertial jet (*Lutjeharms and van Ballegooyen, 1984*). This simple model suggests that the volume transport of the current is the decisive factor that regulates the position of the retroflection, with low volume transports producing greater westerly penetrations of the retroflection into the Atlantic.

Modeling

De Ruijter and Boudra (1985) showed that a strong retroflection could be produced with a high Rossby number in a one-layer model of the current, whereas low Rossby numbers produced little or no retroflection. *Boudra and de Ruijter (1986)* extended this model to two and three layers and showed that the change in vorticity balance when the current separates from the shelf was responsible for the retroflection. The model of *Ou and de Ruijter (1986)* included the β -effect, inertia and the curvature of topography. It demonstrated a separation from the coast and a retroflection strongly dependent on the volume flux of the current. *Boudra and Chassignet (1988)* determined that vertical stretching of the vorticity was as important as the planetary component in generating the retroflection. They also showed that representing the shape of the Agulhas Bank more realistically produced greater leakage and ring formation in the model.

Observations

Using satellite infrared imagery, *Lutjeharms and van Ballegooyen (1988a)* demonstrated that the Agulhas retroflection loop progresses westwards until an Agulhas ring is spawned. This event returns the retroflection to an eastward position. They also concluded that the rate of the westward penetration of the retroflection increases until an Agulhas ring is spawned and that the mean duration of each event is 39 days. In general the Agulhas Current retroflection seems to be located between 15°E and 20°E (*Lutjeharms and van Ballegooyen, 1988a*). *Lutjeharms and van Ballegooyen (1988b)* speculate that early retroflection, which occurs at about 25°E, and is triggered by the “Natal Pulse”, may cause a dramatically reduced flow downstream, fewer ring shedding events, or alternatively smaller rings and as a result less leakage of Indian Ocean water into the Atlantic. However, these speculations have yet to be proven conclusively because the depths to which these early retroflections extend are not known (*de Ruijter et al., 1999*). The occasional occurrence (two or three times a year) of a bifurcation of the Agulhas Current resembling an early retroflection, located just south of Port Elizabeth,

was noted by *Lutjeharms and van Ballegooyen (1988b)*. “Natal Pulses” are large cyclonic meanders of the Agulhas Current that originate in the Natal Bight at about 29°S (*Gründlingh, 1979; Lutjeharms, 1981a; Lutjeharms and Roberts, 1988*). Theoretical considerations indicate that the shelf-slope configuration alongside the northern Agulhas Current inhibits instabilities in the current trajectory, except at the Natal Bight north of Durban, at about 30°S (*De Ruijter et al., 1999*). Here the weaker gradient in the continental slope allows instabilities intermittently leading to the initiation of a pulse. Recent analyses of a variety of satellite data have indicated that most “Natal Pulses” that reach the Agulhas retroflection precede a ring shedding event (*Van Leeuwen et al., 1999*).

The average diameter of the retroflection loop is about 340 ± 60 km, based on data for a four year period (*Lutjeharms and van Ballegooyen, 1988a*). According to *Gordon et al. (1987)* the Agulhas Current introduces about 70 Sv of water (relative to 1500 dB) into the Agulhas retroflection within the upper 1500 m. A small part of this flow, about 10 Sv, combines with 5 Sv of South Atlantic Water (which is derived from the blend of South Atlantic thermocline and subantarctic water) to flow into the South Atlantic. Most of the Agulhas transport returns to the Indian Ocean. The Agulhas introduces several Indian Ocean water types into the Retroflection region which include: (a) South Indian Ocean subtropical thermocline water, which includes a form of Subantarctic Mode Water; (b) tropical thermocline water from the western Indian Ocean; (c) saline low oxygen Red Sea water; (d) Antarctic Intermediate Water. Mode waters are formed at the sea surface during winter overturning, and are capped during spring by surface warming of the upper layer, allowing them to enter the thermocline (*McCartney, 1977*). The subantarctic Mode Water present in the Agulhas system originates in the south-western Indian Ocean. Within the Agulhas Retroflection Indian Ocean water masses are modified in two ways: (a) The upper thermocline water upon exposure to the colder atmosphere forms water which is anomalously salty relative to the Agulhas inflow. This water is confined for the most part within the cores of the main retroflection and the warm eddies. (b) The deeper thermocline waters mix with South Atlantic water, which enters the retroflection region by being swept in by the anticyclonic circulation of the warm-core eddies. This “contamination” of the Agulhas Retroflection thermocline with South Atlantic Water

increases with depth, until density levels are reached at which no contribution from the Indian Ocean is evident. The above description of the water types present in the retroflexion region was provided by *Gordon et al. (1987)* from the analysis of data collected by the RV *Knorr* and RV *Meiring Naude* during October-December 1983.

Agulhas Rings

As mentioned before, the retroflexion loop of the Agulhas Current periodically pinches off and sheds an Agulhas Ring (*Lutjeharms, 1981a; Lutjeharms and Gordon, 1987*). *Olson (1991)* defines rings as intense eddies or vortices that represent a wrapped-up piece of a major ocean current. This phenomenon is not isolated to this region and rings have been associated with other western boundary currents as well. The Gulf Stream sheds both cold- (*Fuglister, 1972*) and warm-core rings (*Joyce, 1985*); the Kuroshio forms rings in a manner similar to that of the Gulf Stream (*Solomon, 1978*); the East Australian Current produces two rings per year (*Nilsson and Cresswell, 1981*) and the Brazil Current produces one every two months (*Legeckis and Gordon, 1982*).

In the above-mentioned current regimes, the rings are pinched off from meanders in the currents and remain in the ocean in which they were formed, often being re-absorbed into the main current again (*Gulf Stream Ring Group, 1981; Kuroshio Solomon, 1978; East Australian Nilsson and Cresswell, 1981*). Rings may also coalesce (*Cresswell, 1982*). Coalescence of rings and reabsorption into the current also occur in the Agulhas system. *Duncombe Rae (1994)* mentions that coalescence may be a feature of Agulhas Rings constrained within the Cape Basin by the Walvis Ridge. Hydrographic data taken within the region between the Agulhas Current and the Agulhas Return Current showed evidence of reabsorption of rings into the Agulhas circulation (*Gordon et al., 1987*). *Duncombe Rae (1994)* suggests that these features may not be common in Agulhas rings because the rings are not constrained by topography or dynamics to the proximity of the mother current and can move great distances from their source into the South Atlantic.

History

The study of the existence, origin and oceanographic interaction of Agulhas rings have commanded ever-greater scientific scrutiny over the last three decades. Rings were found hydrographically near the retroflection before their true nature was realized. *Duncan (1968)* detected a large eddy, probably from Agulhas origin, but was in some doubt as to the mechanism responsible for it. A major three-ship survey in March 1969 (*Bang, 1970a, b; Harris and Van Foreest, 1978*) resulted in the production of the first clear picture of the retroflection region, as well as the eddy field west of the retroflection region. *Bang (1970a)* suggested that these eddies might move into the South Atlantic. *Harris and Van Foreest (1978)* presented the vertical sections from the cruises and described a deep-reaching eddy which had the characteristics of an Agulhas ring situated at a position similar to various “Cape Town Eddies” described in later literature.

Lutjeharms (1981a) used satellite thermal infra-red data to demonstrate the instability of the Agulhas retroflection and its ability to form rings. The first concentrated hydrographic study of rings undertaken at the Agulhas retroflection was during the Agulhas Retroflection Cruise in November 1983. Three vessels (RV *Knorr*, MV *SA Agulhas*, and RV *Meiring Naudé*) surveyed the Agulhas Current system from the Eastern Cape coast to west of Cape Town. Two recently spawned rings were detected, the Cape Town and Retroflection eddies (*Olson and Evans, 1986*).

In subsequent years more rings in the vicinity of the retroflection region and Cape Town were detected and surveyed hydrographically. In 1985 the RV *Thomas Washington* surveyed an anticyclonic ring south-west of Cape Town (*Bennett, 1988*). A third large-scale study, the Subtropical Convergence and Agulhas Retroflection Cruise (SCARC) during February 1987, found at least five rings in the retroflection area whose isothermal depressions suggested that they were of Agulhas origin (*Lutjeharms, 1987; Valentine et al., 1988*). *Shannon et al. (1989)* presented the upper-layer sections from this cruise. The most recent interest in the retroflection region and its associated features, focuses on the

manner in which the products of the Agulhas Current leak into the South Atlantic and distribute their excess heat and salt in this ocean basin (*Lutjeharms et al., 2000*).

Serendipitous measurements

Agulhas rings move into the South Atlantic, representing an input of heat and salt into the cool eastern arm of the South Atlantic gyre. The presence of these Agulhas rings were detected by chance observations made by vessels such as the *Oceanus*, which crossed an Agulhas ring in the mid-Atlantic in 1983 (*McCartney and Woodgate-Jones, 1991*), and the *Discovery*, which crossed an Agulhas ring near Vema Seamount in 1987 (*Gordon and Haxby, 1990*). In this same area the FRS *Africana* encountered a ring in 1989, and this discovery led to the expedition aboard the RS *Benguela* which set out to examine this ring a month later (*Duncombe Rae et al., 1989; Duncombe Rae et al., 1992b*). These cruises represent the first intensive hydrographic examination of a ring within the South Atlantic, away from the immediate vicinity of the retroflexion. The data collected from the Vema ring consisted of two cruises of hydrographic measurements, NOAA satellite sea surface temperatures and GEOSAT altimetry. During the South Atlantic Ventilation Experiment cruise (SAVE-4) in January 1990, two Agulhas Rings were crossed (*Gordon et al., 1992*). One of the two rings surveyed during this expedition may have been the Vema ring which has been delayed by the Walvis Ridge, because the estimated time of shedding of both rings was the end of 1988 (*Duncombe Rae, 1994*). In September 1997, during the Benguela Current Experiment cruise on the RV *Seward Johnson*, XBTs and CTD/O2/LADCP stations were used to survey three anticyclonic rings in the South Atlantic (*Roubicek et al., 1998*). Seven RAFOS floats and six surface drifters were launched in the rings in order to follow their paths, and to measure their rotation rates.

Formation

Lutjeharms and Van Pallegooyen (1988a) described the process of ring separation from the retroflexion based on their investigation of satellite infrared imagery and selected hydrographic measurements. Each progradation sequence of the retroflexion is

concluded with the shedding of a warm-core Agulhas ring, accompanied by the flow of Subantarctic or South Atlantic water into the gap separating the ring and the retroflexion. Depending on the position of the shedding event, rings may move southward, westward or northward.

Boudra and De Ruijter's (1986) and *Boudra and Chassignet's (1988)* multi-layer modeling studies of the wind-driven South Atlantic/Indian Ocean circulation and Agulhas retroflexion region showed the formation of rings at the retroflexion. *Chassignet and Boudra (1988)* concluded that, at high Rossby numbers, ring formation, in their model domain, is associated with mixed barotropic instability. Experiments in which rings formed showed a greater transfer of mean kinetic to eddy kinetic energy. The instability required for ring formation depended on the shape of the Agulhas Bank shelf-break. In a further refinement of the model (*Boudra et al., 1989*), ring formation was simulated even more realistically.

Anatomy

The influence that rings have on their environment is determined by their intensity. The strength of the flow around the ring, i.e. the swirl velocity, determines the extent to which the ring disturbs the properties of the waters in its surroundings as well as the volume of the fluid that the ring actually traps and carries with it as it translates [*Flierl, 1981; Nof, 1983; Davey and Killworth, 1984*]. Swirl velocity depends on the energy initially imparted to the ring at its formation for its continued strength in dissipative processes. After its formation, the instantaneous ability of the ring to affect its surroundings is determined by the conversion of available potential energy in the initial mass field to kinetic energy in the flow around it (*Olson et al., 1985*). Soon after the shedding event rings rapidly lose their distinctive surface thermal expression due to heat-loss to the atmosphere in the South Atlantic. This rapid heat loss drives deep convective overturning and causes the generation of deep isothermal surface layers, particularly during winter (*Duncombe Rae, 1994*). The loss of heat to the atmosphere diminishes the amount of heat transferred by the rings to the South Atlantic (*Olson et al., 1992*).

Flierl (1981) calculates two types of paths followed by fluid particles as an eddy moves through a region: closed loops representing particles trapped in and moving with the eddy, and meanders corresponding to a wave-like disturbance induced by the passage of the eddy. The non-dimensional parameter ϵ , the ratio of the maximum azimuthal speed at a depth to the eddy drift speed, determines whether a trapped region exists at a given depth. For depths where $\epsilon > 1$, there is no trapped region in the eddy and the water column is only ‘stirred’, eventually leaving the fluid particles behind. For $\epsilon < 1$, the trapped region is a teardrop shape centered equatorwards of the (anticyclonic warm-core) eddy centre, which moves along with the eddy at the eddy drift speed. Therefore, although the expression (e.g. depressed isotherms) of Agulhas rings extends throughout the water column (> 4000 m; *Gordon and Haxby, 1990*), only the upper water masses (i.e. Intermediate, Central and Surface waters) may be expected to translate with the ring.

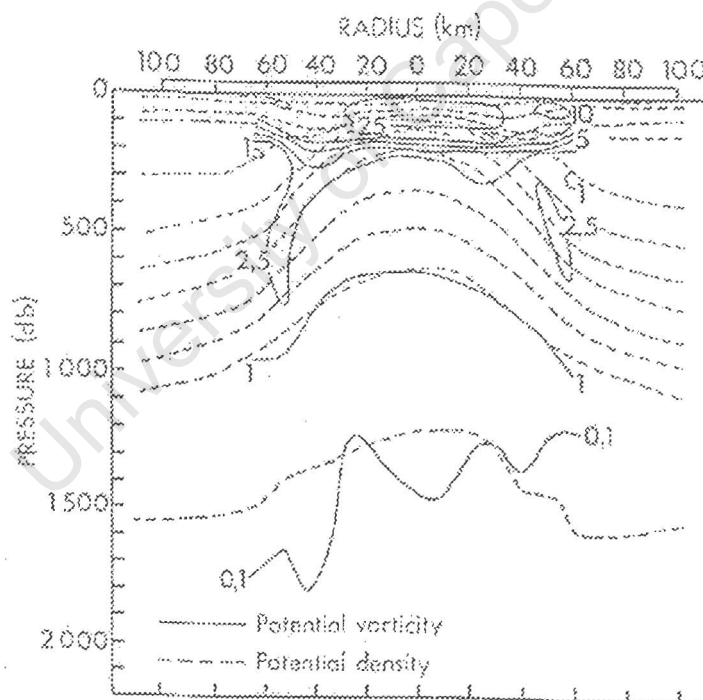


Figure 3.1: *The potential vorticity superimposed on the potential density for a cyclonic ring. Preferred mixing paths along isopycnals are blocked by bands of high potential vorticity, confining the water to the ring centre. (From Olson, 1980.)*

The potential vorticity structure of a ring, and the medium in which it is embedded, also places a constraint on the long-term evolution of the ring. The potential vorticity constrains both the rate at which the ring converts and releases energy and the ability of the ring to transport mass (*Olson et al., 1985*). *Kamenkovitch et al. (1986, p. 221)* provide an interpretation of how potential vorticity is involved in trapping fluid within an eddy. *Figure 3.1* is an illustration of the potential vorticity superimposed upon the potential density for a cyclonic eddy. The situation would be similar for an anticyclonic eddy (*Duncombe Rae, 1991*). For mixing to take place between the core and the surroundings of the eddy, a fluid parcel must move along isopycnals. Conservation of potential vorticity implies that the fluid parcel must maintain a constant potential vorticity. It is clear, from the figure, that the fluid would be blocked in its path along isopycnals by the lobes of high vorticity along the ring edges.

Duncombe Rae (1991) compiled a list of rings encountered hydrographically in the South Atlantic. He found that isothermal depressions, for most of those rings, were around 300 to 400 m. There were two anomalous rings, a winter ring and a ring situated very close to the continental shelf, which had isothermal depressions of 510 m and 145 m respectively. Rings with a more westerly motion, situated further south and closer to the subantarctic water also exhibited large isotherm depressions. However, one ring situated very far south, did not show excessive isotherm depression. He concluded (*Duncombe Rae, 1994*) that anomalously small or large isotherm depressions could have been attributable to the time of sampling of the ring relative to the time of ring shedding (large isotherm depressions were identified close to the retroflexion), the surrounding water mass conditions (rings with a more westerly motion, being further south and closer to subantarctic water showed large isotherm depressions) or artifacts of the sampling strategy (some rings may not have been adequately covered in the sections across them).

Duncombe Rae (1994) found that Agulhas rings, in general, retain their Agulhas water mass characteristics sufficiently to provide an unambiguous identification of their origin. Modifications to the original Agulhas characteristics were evident with increasing distance from the retroflexion region because the longer time since shedding allows

greater opportunity for mixing of the core waters. However, some rings close to the retroflection experience substantial mixing of the core water with the South Atlantic thermocline (e.g. Cape Town eddy: *Olson and Evans, 1986; Chapman et al., 1987; Fine et al., 1988*).

Inter-basin exchange mechanisms

Based on all current information (*Lutjeharms, 1996*), the leakage of thermocline water from the South Indian into the South Atlantic would seem to be largely a function of the number and dimensions of the Agulhas rings formed at the Agulhas retroflection. An average of six rings appear to be shed each year, pinching off at irregular intervals (*Feron et al., 1992; Goni et al., 1997*). Sometimes there are long periods without any ring formation, e.g. between April and November 1993, no rings were shed, but three rings were formed rapidly in November and December of that same year (*Goni et al., 1997*). Although modeling results (e.g. *Lutjeharms and van Ballegooyen, 1984*) suggest that a decreased volume flux of the Agulhas Current may induce the retroflection loop to penetrate further into the South Atlantic and that shifts in the latitude of minimum wind stress curl (*de Ruijter and Boudra, 1985*) would allow a greater or lesser degree of Agulhas water to leak into the South Atlantic, the actual mechanisms that result in the shedding of an Agulhas ring are not clear.

Duncombe Rae (1994) compared the heat, salt and volume fluxes associated with the rings examined in his doctoral study to the volume flux associated with the thermohaline circulation of the conveyor belt. Analysis of the temperature and salinity differences between sections across rings and profiles representative of the Agulhas Current and the South Atlantic Ocean suggest that Agulhas rings do transfer a significant flux of these properties from the Indian to the Atlantic Ocean. He concluded that instantaneous fluxes of the rings were approximately of the same order of magnitude as the cross-equatorial flow. However, since only 5 to 9 rings enter the South Atlantic in the course of a year, the average flux contributed by Agulhas rings may be less than the net flux required to balance the deep water outflow.

Local effects of Agulhas Rings

An obvious local effect induced by Agulhas rings during their passage across the Atlantic is a trail of mixed and stirred water left in their wake (*Duncombe Rae, 1991*). The resulting frictional energy transfer will heighten the background energy field of the ocean basin while ageing and spinning down the ring.

A ring that moves more northwards than westwards from the retroflection, a possible result of steering by the topography of the West Coast shelf, will likely come into contact with the Benguela upwelling system. This interaction is of significant economic importance to both South Africa and Namibia because the Benguela upwelling system supports the fishing industries of both these countries. *Duncombe Rae et al. (1992a)* demonstrated this scenario when they investigated the interaction of an Agulhas ring with the Benguela upwelling system during June and July 1989. A filament from the Benguela upwelling front was in the process of being entrained by a passing ring of Agulhas water at that time. According to *Duncombe Rae (1994)* the Agulhas ring had to be in close proximity to the Benguela for a month or more for this interaction to be effective. He postulated that the Agulhas ring/Benguela front interaction could have important implications for plankton and fisheries in the Benguela system and that the interaction recorded April – June 1989 was regarded as a possible contributor to the very poor yearclass of anchovy of 1989.

It was mentioned earlier in this review that high rates of surface cooling in new rings destroy their surface expressions and *Olson and Evans (1986)* show that heat is lost quickly to the atmosphere, leaving the salt. These additional sources of heat to the lower atmosphere may influence passing weather systems affecting the climate of South Africa (*Walker, 1990; Rouault and Lutjeharms, 1994*).

Agulhas Filaments

The retroflection of the Agulhas Current is incomplete and some of the current flows into the South Atlantic (*Shannon, 1966; Bang, 1973; Gordon, 1985; Shannon et al., 1990*). Along the eastern part of the Agulhas Bank, the horizontal shear between the Agulhas Current and the relatively quiescent water over the shelf causes the development and growth of shear edge features that include eddies (*Lutjeharms et al., 1989*). These eddies are in turn responsible for the extraction of plumes of warm Agulhas water from the edge of the current. Along the eastern part of Agulhas Bank these warm plumes disperse over the shelf (*Lutjeharms et al., 1989*). In contrast the plumes formed west of about 22°E tend to move northwestward as long Agulhas filaments along the western shelf edge into the South Atlantic (*Lutjeharms and Stockton, 1987*), where they rapidly disperse and lose their distinctive surface temperatures. The contrasting behaviour observed for those filaments which are formed on the western side of the Agulhas Bank is a result of the general northwesterly drift of the Benguela Current in this region (*Lutjeharms and Stockton, 1987*), the prevalence of strong south-easterly winds here, and the recurring presence of recently shed Agulhas rings at this particular location (*Lutjeharms and Valentine, 1988*). Some filaments are not drawn into Agulhas rings and will thus contribute their fluxes independently (*Lutjeharms and Cooper, 1996*).

Based on satellite imagery for the period 1987-1991, *Lutjeharms and Cooper (1996)* concluded that filaments in general follow the western edge of the Agulhas Bank in their equatorward advection. The source points of filaments on the border of the Agulhas Current are usually just downstream of the southernmost point of the Agulhas Bank. They were also able to show that six or seven filaments are formed per year, each lasting three to four weeks. The average width of the filaments was observed to be 50 ± 16 km and the average length 530 ± 166 km. Filaments traversed by research ships were shown to extend no further than 60 m down the water column and the average drift rate of filaments varied between 8.5 and 125 km day⁻¹.

Section B

Applications of Satellite Remote Sensing

The onset of satellite remote sensing of the oceans made it possible to contemplate the synoptic observations of geostrophic surface currents, wind stress and sea surface temperature over an ocean network approaching that now routinely available to meteorologists over land. These data, when combined with subsurface density and current measurements, should provide global information on the general circulation of the ocean and its primary driving forces. In this chapter a general overview of the processes involved in obtaining remotely sensed satellite data is provided. This is followed by a discussion of the two instruments from which data was obtained for this investigation. Lastly the use of satellite products in South African oceanographic research of the Agulhas retroflection and associated features is reviewed.

Overview of remote sensing processes

Satellite remote sensing relies on electromagnetic radiation to convey information about the sea to a sensor on a satellite. Much of the electromagnetic radiation is absorbed or scattered by the atmosphere, but there are three distinct wavebands (spectral windows) at which rays can penetrate the atmosphere with less interference. These are the visible band (400 – 700 nm), parts of the infra-red (the regions around 3.7 μm and 10 – 13 μm are used), and microwaves, which include radar, longer than about 10 mm.

Sensors may be either passive or active. Passive sensors measure naturally occurring radiation, using either the Sun's rays scattered from below the sea surface, or energy emitted by the sea itself in the infrared or microwave parts of the electromagnetic spectrum. Active sensors produce their own source of electromagnetic energy, which is emitted down from the satellite towards the sea and the return backscatter is measured after reflection. For a sensor to be useful for a particular application requires that the measured radiation be influenced in some way by the ocean parameter being monitored.

The influence can be direct, as with infrared radiation emitted by the sea surface according to its temperature. It can be more complex, as in the way the spectral composition, or colour, of sunlight scattered from below the surface is influenced by both the chlorophyll and particulate content of the water. It may be more subtle, as in the way the sea state changes the shape of the reflected pulse of a nadir-viewing radar. A number of useful oceanographic instruments are available on spaceborne platforms (Figure 3.2).

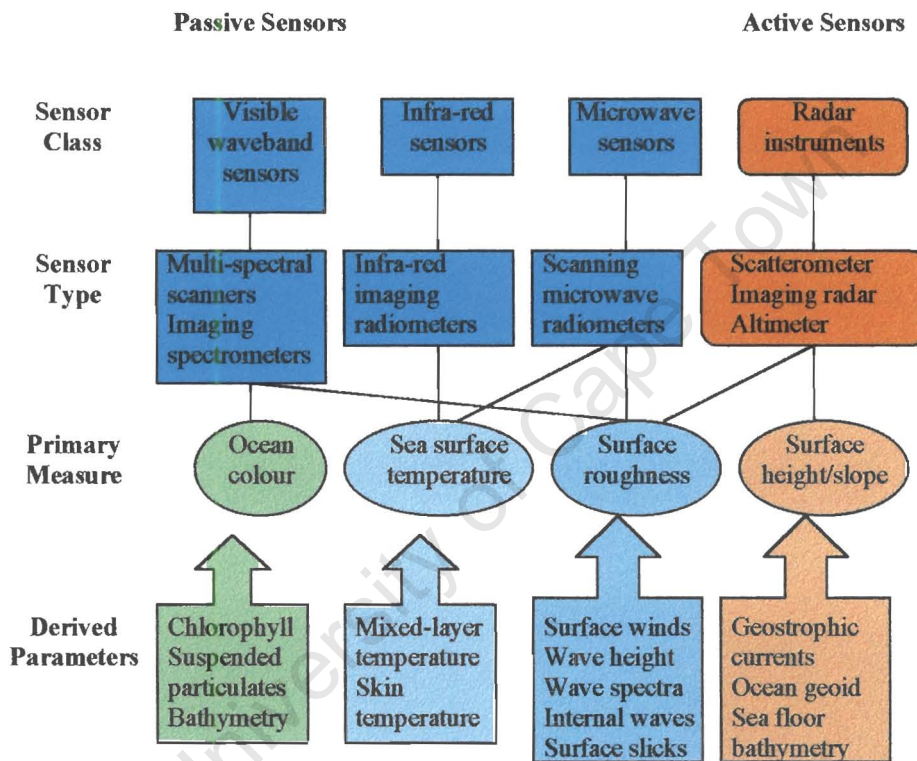


Figure 3.2: Schematic showing the different classes of sensors used in satellite oceanography, the different types of instrument, the primary measurement which each class can make, and examples of the ocean parameters which can be derived from these measurements. (From Robinson and Guymmer, 1996)

Remote sensing has limitations and many important aspects of the ocean cannot be detected remotely with the present technology and knowledge. Most satellite remote sensing data comes from near the upper sea surface. Data showing how the ocean properties change with depth must be measured *in situ*. The greatest advantage in remote

sensing lies in its ability to provide nearly simultaneous measurements of ocean parameters over a wide sea area. The size of the area that can be viewed simultaneously, the spatial resolution of the resulting image data, and the frequency with which it can be revisited depend on the type of sensor and the platform carrying the instrument.

Two types of orbit are employed by space platforms for remote sensing of the ocean. Earth observation satellites in near-polar orbit fly at an altitude of about 700 – 1000 km above the Earth. The orbit is normally arranged to precess slowly so that the orbit plane remains fixed relative to the Sun, thus ensuring a uniformity of solar illumination (sun synchronous) for ocean colour scanners. A consequence of this orbit is the elimination of problems that would be experienced as a result of the diurnal heating cycle. However, this type of orbit limits coverage of a specific area on the Earth's surface to once a day, and necessitates a very oblique view at the swath extremities if daily coverage is required. The other type of orbit configuration used for remote sensing of the sea is that of a satellite in geostationary orbit. A geostationary satellite is parked in high orbit above the equator and orbits the earth once per day, so that it remains stationary relative to an observer on the Earth's surface. From this vantage point, a sensor can scan the whole of the visible disc of the Earth, and can sample at any frequency. Although this platform allows for a high sampling rate, resolution is sacrificed because of the oblique view. Sensors cannot view high latitudes above 55° because of the curvature of the earth.

The raw data transmitted from the satellite has to be pre-processed before it can be of use to the marine scientist. *Figure 3.3* outlines the various procedures involved in acquiring satellite data and processing them to yield oceanographic information. A sensor calibration is applied to the digital signal in terms of the property of radiation being measured at the satellite. Radiation passing through the atmosphere interacts with particulate matter suspended in the atmosphere and with the molecules of the constituent gases. An atmospheric correction, which is an estimate of the radiation that the sensor would have detected leaving the surface of the sea if there were no intervening atmosphere, is applied to the recorded digital data. A variety of approaches are used for this:

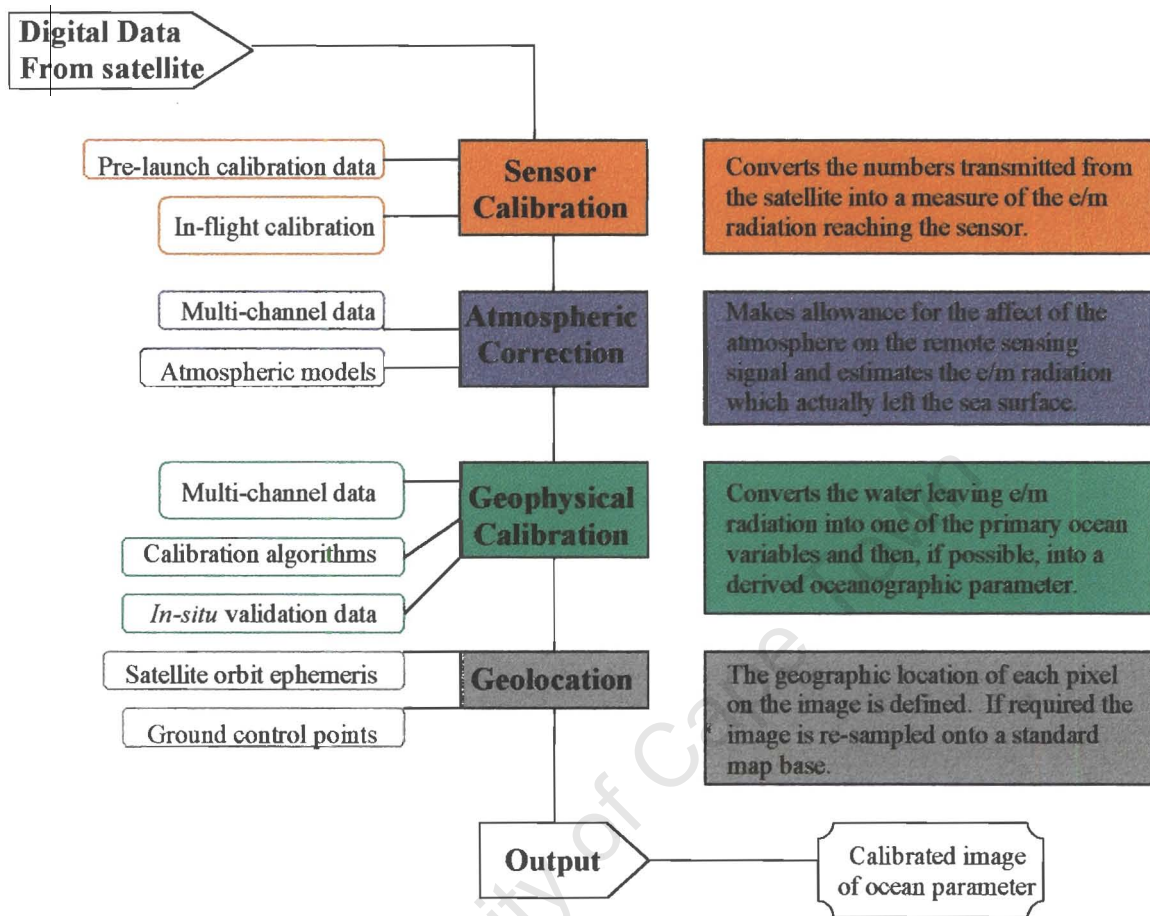


Figure 3.3: Outline of the procedures required for processing data received from satellites. (From Robinson and Guymer, 1996)

- ✘ The use of a model atmosphere with parameters determined from historic data;
- ✘ The use of a model atmosphere with parameters determined from simultaneous meteorological data;
- ✘ The elimination of, or compensation for, atmospheric effects on a pixel-by-pixel basis;
- ✘ Calibration with *in situ* measurements of geophysical parameters.

The value obtained after atmospheric correction may be a useful parameter for some applications, e.g., the sea surface temperature (SST), however, it is often appropriate to apply a geophysical correction to convert the measured radiance into an oceanographically useful parameter, e.g., converting radar back-scatter into wind speed

and direction. Calibration algorithms are generally derived empirically using *in situ* data and calibration or validation experiments. Geolocation is the final procedure required to be performed on the digital data in order to produce a calibrated image of an ocean parameter. This procedure involves the identification of the geographical position of every data value so that the image data can be presented in the form of a regular map projection.

During the course of this project, data from two remote sensing products were used to analyze an oceanographic event: SST from AVHRR (NOAA) and sea surface height from the altimeter (TOPEX/POSEIDON and ERS-2).

The Advanced Very High Resolution Radiometer (AVHRR)

(<http://isis.dlr.de/guide/NOAA-AVHRR.html>)

AVHRR SST data have been used in the past two decades to study the Agulhas Retroflection region, Agulhas Rings and Agulhas Filaments. This has been done by constructing sea surface temperature false-colour images which illustrate the spatial distribution of sea surface temperature, thereby highlighting various structures with contrasting temperature signatures. An example of this would be the temperature distribution in an upwelling cell, i.e. approximately 8°C to 16°C, as opposed to that of an Agulhas Ring, i.e. approximately 18°C to 22°C. This data has dense spatial distribution (of the order of 1 km²) and depending upon the cloud cover, can provide good continuity to study the evolution of upwelling events or Agulhas ring shedding.

The USA-based National Oceanic and Atmospheric Administration (NOAA) has been providing global estimates of sea surface temperature since 1970, with first the Improved Tiros Operational Satellite (ITOS) series and later the Tiros-N (Television Infrared Observation Satellite) generation of operational polar satellites (McClain *et al.*, 1985). NOAA-6 and NOAA-7 were the last in the TIROS-N series, which was then renamed Advanced TIROS-N (ATN) on the launch of NOAA-8. The ATN satellites have a repeat cycle of 12 hours, an orbital altitude of 830-870 km and an inclination of approximately

98.7° to 98.9°. Polar orbiters are able to monitor the entire earth, tracking atmospheric variables and providing atmospheric data and cloud images. The orbits are timed to allow complete global coverage twice per day, per satellite (normally a daytime and a nighttime view of the earth) in swaths of 2 600 km in width. They provide visible and infrared radiometer data that are used for imaging purposes, radiation measurements and temperature profiles. Currently NOAA is operating two polar orbiters: NOAA-14, launched in December 1994, and a new series of polar orbiters, with improved sensors, which began with the launch of NOAA-15 in May 1998.

The AVHRR is carried on NOAA's Polar Orbiting Environmental Satellites, beginning with TIROS-N in 1978. It is a radiation-detection imager used for remotely determining cloud cover and the surface temperature. This scanning radiometer (aboard NOAA-7 to NOAA-14) uses five detectors that collect different bands of radiation wavelengths. The high-quality digital measurements provided by the AVHRR have a spatial resolution of approximately 1.1 km² at nadir in the visible (0.58 - 0.68 μm) and reflected-infrared (0.725 - 1.1 μm) bands and two or three emitted infrared "window" channels (3.55 - 3.93 μm, 10.3 - 11.3 μm, 11.5 - 12.5 μm). These "window" channels allow for the detection of heat radiation from, and hence, the temperature of land, water, sea surfaces, and the clouds above them. The AVHRR data are acquired in two formats: High Resolution Picture Transmission (HRPT), Local Area Coverage (LAC) and Global Area Coverage (GAC) recorded on board. HRPT LAC data are full resolution data transmitted directly to a ground station. GAC data is recorded on board and provided twice daily at a nominal resolution of 4 km by sampling every fourth pixel and every fourth line.

The Altimeter

Satellite altimetry offers the ability to measure global sea surface heights. The distance between the satellite and the sea surface is measured using radar and the exact position of the satellite relative to the earth is calculated at the same time. These measurements are used in conjunction with a number of atmospheric corrections in order to calculate the sea surface height deviation from a mean value. Sea surface slopes can be calculated and

hence the barotropic geostrophic flow can be evaluated. The large scale ocean circulation (including currents and eddies) can now be detected and monitored from space on a variety of time scales.

To date eight altimeters have flown on satellites. The first experiment was flown on SKYLAB and provided useful engineering data on which the subsequent altimeters were developed. GEOS-3 carried the first scientific altimeter, but the resulting data lacked sufficient accuracy and coverage to aid in significant scientific research. SEASAT carried a better altimeter and offered global coverage, but the mission unfortunately only lasted three months. The next altimeter, flown on GEOSAT, functioned for several years (1985 - 1990) and provided the scientific community with a wealth of data on which numerous studies were done.

Currently, two identical altimeters are carried on the multi-disciplinary remote-sensing satellites ERS-1 and ERS-2. The ERS-1 satellite was launched on 17 July 1991 (<http://www.ae.utexas.edu/courses/ase389/sensors/alt/alt.html>) and carries on-board a number of instruments consisting of a core set of active microwave sensors supported by additional, complementary instruments: the Active Microwave Instrument (AMI), which combines a Synthetic Aperture Radar (SAR) operating in image or wave mode and a wind scatterometer; the Radar Altimeter (RA); the Along-Track Scanning Radiometer and Microwave Sounder (ATSR), the Precise Range and Range-Rate Equipment (PRARE) and Laser Retroreflectors (LRR). ERS-2 was launched on 20 April 1995 and carries the same sensors as ERS-1, as well as an absorption spectrometer which measures the presence of ozone, trace gases and aerosols in the stratosphere and troposphere (information gathered for global ozone monitoring experiment GOME). ERS-1 orbits the earth in 101.7 minutes, has an orbital altitude of 785 km, an inclination of 98.5° and repeat periods which can be varied between 3, 35 and 176 days. ERS-2 has very similar parameters: an orbit period of 100.48 minutes, an altitude of 781.36 km, an inclination of 98.54° and a repeat period of 35 days. The ERS Tandem mission was approved in April 1995 by the European Space Agency (ESA) Council for a period of nine months

following the ERS-2 Commissioning Phase. This provided the ESA with an opportunity to assess the following:

- the same instrument on both satellites observing the same area on the ground with a one-day interval, e.g. for SAR interferometry and/or change detection. ERS SAR interferometry had already been validated using ERS-1 data only, with a 3 or 35-day repeat cycle. The one-day offset offered by the tandem mission increases the probability of having high coherence between the acquired data;
- the same instrument on both satellites observing different areas on the ground on the same day, to provide increased spatial sampling;
- different instruments observing the same areas on the ground within a very short interval (less than 1 hr), e.g. the Wind scatterometer and the Radar Altimeter for comparison of wind measurements.

Although ERS-1 is still in good health, it was put into hibernation a year after its successor ERS-2 was launched and carried over its operational duties.

The dedicated altimeter satellite TOPEX/POSEIDON was launched on 10 August 1992 and it has been providing data of greater accuracy than previous satellites (*Gründlingh, 1995*). The mission is conducted jointly by the United States National Aeronautics and Space Administration (NASA) and the French space agency, Centre National d'Etudes Spatiales (CNES). TOPEX/POSEIDON is a satellite mission that uses radar altimetry to make precise measurements of sea level with the primary goal of studying the global ocean circulation (http://podaac-www.jpl.nasa.gov:2031/DATASET_DOCS/topex_mgdr.html). It has a repeat cycle of 10 days and carries two altimeters: a French solid-state altimeter and a US dual frequency altimeter.

Six science instruments are carried aboard the platform; four operational and two experimental: the NASA radar altimeter (NRA), the Solid state radar altimeter (SSALT), the TOPEX microwave radiometer (TMR), the Laser retroreflector array (LRA), The Doppler tracking system receiver (DORIS) and the Global positioning system demonstration receiver (GPSDR). The SSALT and the GPSDR are experimental instruments. The TOPEX and POSEIDON altimeters use radar to measure the distance

from the satellite antenna to the ocean surface by transmitting pulses to the sea surface and measuring the time it takes the pulses to return to the spacecraft. Wave height and near surface wind speeds can be estimated from the shape of the echo pulse. Geophysical corrections are applied to minimize altitude measurement errors introduced by ionospheric electrons, propagation through the troposphere, and the electromagnetic bias arising from the reflection of the radar pulses from asymmetric ocean waves. Data from one of several orbit-determining systems (laser tracking, GPS and DORIS) are used to accurately determine the position of the satellite. Position measurements are made by a network of ground-based lasers dedicated to tracking the satellite and by on-board instruments using radio techniques to determine distance or velocity.

The TOPEX/POSEIDON Merged Geophysical Data Records (MGDR) contain global coverage altimeter data. Geophysical Data Records consist primarily of satellite measurements of sea level (altimeter ranges), including all corrections applied to the data (instrument effects), plus the precise ephemeris of the satellite. All measurements are appended with the latitude, longitude and the time of the observation. The records also include the altimeter measurements of wave height, wind speed, ionospheric electron content, the microwave radiometer observations of brightness temperatures, plus the derived value of tropospheric water vapour and the best available values for the height of the tide and the geoid. Finally the records include flags that reflect the numerous conditions of the sensors and of the values of the data during processing. Data records are at a one per second rate, sampled along satellite track at nadir and averaged over a 5-10 km footprint depending on wave height. In the tropical Pacific, comparisons with tide gauges show that TOPEX/POSEIDON has an accuracy of 2 cm when averaged over spatial scales of a few hundred kilometers (*Cheney et al., 1994*).

The use of satellite remote sensing in the investigation of the Agulhas Retroflection Region

During the late 1970's, infrared imagery was used, for the first time, by South African scientists to investigate meso-scale variability in the Agulhas Current System. In 1976 and 1977 the Very High Resolution Radiometer (VHRR), aboard NOAA's polar orbiting satellites NOAA 4 and 5, was used to collect thermal infra-red and visible data with a spatial resolution of 1 km, over the Southwest Indian Ocean and part of the Southeastern Atlantic. These images were used to prove that surface temperature differences in the Agulhas Current System are sufficiently contrasting to enable features to be identified when cloud cover is absent (*Harris et al., 1978*).

Harris et al. (1978) made the assumption that the infrared radiation signature is representative of a substantial subsurface water body and found that the 1976-77 imagery revealed sources of the Agulhas Current, time-dependent wave-like structures, sharp current retroflections, and the contribution of the Agulhas Current to the South Atlantic.

Lutjeharms (1981a) presented an overview of the large and meso-scale features of the southern Agulhas Current circulation, as derived from the satellite images covering the Agulhas Current region which had been collected and studied up to that time. He constructed a conceptual image of the main circulation features, associated with Agulhas Current circulation, as observed on satellite imagery. The possible importance of relatively small-scale disturbances to the general circulation of this region was also mentioned in this work.

Lutjeharms and van Bailegooyen (1988a) described the nature of the kinematics of the Agulhas Current retroflection based on satellite infrared imagery and selected hydrographic measurements. In the course of their investigation, they utilized data from the radiometers aboard the geostationary satellites METEOSAT I and II, the VHRR aboard the polar orbiting NOAA 4 and 5 and the AVHRR of the NOAA 6, 7, TIROS N and Nimbus 7 satellites. The conclusions of their investigation were summarized in a

conceptual image (*Figure 1.1*). They found that the Agulhas retroflexion lies between 20° and 16° E and that the mean diameter of the retroflexion loop is 342 km. The retroflexion showed a mean westward progradation (~12 cm/s) and each progradation concluded with the shedding of a warm-core Agulhas ring (~9 times a year). Of great value to this current investigation is their mention of the occasional presence of filaments of warm Agulhas Current water that may delineate Agulhas Rings, particularly off Cape Town.

In subsequent years, the use of satellite imagery in combination with hydrographic measurement for the study of oceanographic features around South Africa became more frequent. Satellite observations of vortex dipoles, an integral part of the oceanic upwelling front of the South East Atlantic Ocean, was described for the first time by *Stockton and Lutjeharms (1988)*. The source for the data utilized in these observations was the polar orbiting satellites of NOAA, NIMBUS 7 and TIROS N. *Lutjeharms et al. (1989)* combined hydrographic data with imagery obtained from METEOSAT I and II and NOAA 5 and 9 to investigate boundary phenomena of the Agulhas Current. The shear edge features described in this investigation included meanders, plumes and eddies.

An Agulhas ring was detected using XBT probes on a cruise between Cape Town and Vema Seamount in the South-East Atlantic Ocean in April 1989. The ring and its interaction with the Benguela upwelling frontal system was subsequently investigated using CTD and nutrient data, collected on a second cruise in May 1989, GEOSAT altimeter data for February to April 1989 and cloud-free NOAA-11 satellite imagery from June 1989 (*Duncombe Rae et al., 1992b*). By combining these various resources, the authors were able to speculate about the significance of the ring's interaction with the Benguela system with respect to fisheries applications. The authors were able to determine that the origin of the cool water surrounding the Agulhas ring was upwelled frontal water from the Benguela upwelling region by analyzing the NOAA imagery (*figure 1.4*) and *in situ* salinity data. GEOSAT altimetry provided the means for tracking the origin, and subsequent progress along the South African West Coast, of the Agulhas Ring.

Altimetric data from the first year of the TOPEX/POSEIDON mission and NOAA infrared imagery were used to investigate characteristics of eddies and rings in the oceans around southern Africa (*Gründlingh, 1995*). The altimetry provided insight into rings not visible on the infrared imagery, even in close proximity to the Agulhas retroflection. He found that the eddies in the southeast Atlantic were mainly anticyclonic and estimated that about five Agulhas rings were generated per year. The drift rate of the Agulhas rings varied from 3 to 7 cm/s in a westerly and northwesterly direction. The Indian-Atlantic ocean heat flux was crudely estimated at $3-8 \times 10^{13}$ W.

An extensive investigation of approximately 2700 METEOSAT images from 1985-1992 by *Lutjeharms and Matthysen (1995)* revealed the recurrence of a cyclonic eddy associated with the upwelling front off the Cape Peninsula. From this large collection of images the investigators were able to determine the location, dimensions and longevity of this phenomenon. According to their study the mean diameter of this eddy is 44 ± 17 km, with a mean position of $34.08 \pm 0.29^\circ$ S, $17.57 \pm 0.34^\circ$ E and an average duration of 7 days.

Lutjeharms and Cooper (1996) used satellite infrared images, of the south-eastern Atlantic Ocean and Agulhas Retroflection region, and hydrographic data to show that Agulhas filaments are present about 56% of the time of the study. The authors also found that these filaments are on average 50 km wide, 50 m deep, and carry excess heat of 3.5×10^{19} J, as well as excess salt amounting to about 1 to 5×10^{11} kg into the South Atlantic in each individual filament. Two sources of satellite imagery, covering a period from 1987 to 1991, were employed for this investigation. Contrast enhanced, daily METEOSAT II images were used to establish the presence or absence of Agulhas filaments. Images from the orbiting NOAA 5 to 9 satellites were available, but at irregular intervals due to extensive cloud cover on intervening days. The length and width of 19 filaments were measured from clearly distinguishable filaments on high resolution NOAA satellite imagery (1984 - 1992). In order to estimate the contribution these filaments make to interbasin water exchange, the authors estimated the rate at which the filaments advected

into the South Atlantic. This was done by measuring the daily displacement of the leading edge of each filament over the full period for which cloud-free satellite imagery was available.

A survey of the rings formed from September 1992 until December 1995 in the retroflection region was carried out using TOPEX/POSEIDON altimeter data (*Goni et al., 1997*). A two-layer model was used to estimate the upper layer thickness from the altimeter-derived sea-surface height anomaly data. Their results showed that the number of rings translating simultaneously in this region is larger during the first half of each year. They also found close associations between high variations in transport and ring shedding and a WNW'erly translation with translational speeds ranging from 5 to 16 km day⁻¹. The rings exhibited high values of potential energy (up to 70×10^{15} J) and each contributing an approximate average of 1 Sv of Agulhas Current waters to the Benguela Current.

With the advent of routine satellite observations of the sea surface has come an increased spatial resolution, synoptic geographic coverage and observational frequency made available by these instruments. The importance of combining various satellite remote sensing tools with *in situ* hydrographic data in the analysis of an oceanographic event or feature is clearly highlighted in this review of the use of satellite remote sensing tools in South African oceanography.

Chapter 4

Instrumentation and Methods of Data Analysis

The hydrographic data from the “Christmas Cruise” 1996, covers an important oceanographic phenomenon. It is clear from *Figure 1.2* that the surveyed dipole vortex plays a role in the transport of water from the Agulhas Bank to the Atlantic Ocean. A combination of infrared satellite data and hydrographic data are used to establish the structure of the dipole and filament during the cruise period. Furthermore a series of satellite imagery (infrared and altimetry), pre-dating the cruise, is used to backtrack the development and origin of the dipole. The kind of temporal density required to study the origin and translation of the dipole would not have been possible with *in situ* data alone. In order to present the best possible description of the evolution and eventual structure of the vortex dipole, data were selected and research methods adopted that were thought would best meet the objectives of this investigation.

This chapter describes the instruments that were used to collect the data analysed for this investigation and the methods employed for processing of the data. The significance of the data and the methods adopted for this study is also presented.

CTD and XBT Data

Dr Chris Duncombe-Rae of the Directorate of Marine and Coastal Management (MCM) provided the hydrographic data. CTD data was sampled with a Neil Brown Instrument Systems Mark III CTD unit and Sippican T7 XBT's were launched between CTD stations. The temperature probe of the CTD unit was calibrated at MCM before and after the cruise. Salinity samples were obtained at selected stations for calibration purposes and MATLAB conversion software (written at MCM) was used to apply the salinity corrections and a median filter to the CTD data. Outliers were removed and the resultant dataset could thus provide a reliable reflection of the physical conditions encountered within the water column during the cruise.

Various scripts were written in MATLAB to aid in the further analysis of the *in situ* data at UCT and the SURFER package was used to represent the results graphically. The data was also imported into Ocean Data View for further processing and visualization.

Calculations

i) *Great Circle distance*

Distances between station pairs were calculated according to the formula:

$$dx = R \cdot \arctan \sqrt{\frac{1}{\alpha^2} - 1}$$

where;

dx is the great circle distance in kilometres

$$\alpha = \cos(lat1) \cdot \cos(lat2) \cdot \cos(lon1 - lon2) + \sin(lat1) \cdot \sin(lat2)$$

R is the radius of the earth = 6371 km.

The latitudes and longitudes are given in radians

ii) *Geostrophic velocities*

Relative geostrophic velocities between stations were calculated from the known vertical density structure obtained from the CTD casts. Procedures for the calculation of the geopotential anomalies and the geostrophic velocity were written in the software package MATLAB and the resultant output was contoured and graphically represented in SURFER. The MATLAB procedures were based on the geostrophic balance equations in *Pond and Picard (1986)* p. 73 and adapted for the Southern Hemisphere:

$$(V_1 - V_2) = \frac{10}{L2\Omega \sin\phi} [\Delta D_B - \Delta D_A] \text{ where } \Delta D = \int_{p_2}^{p_1} \delta dp ;$$

In the above equation:

V is the relative velocity, with V_1 and V_2 representing different vertical levels,

L is the distance between stations,

f = $2\Omega \sin\phi$; the coriolis parameter, where $\Omega = 7.29 \times 10^{-5} \text{ rad s}^{-1}$; the angular velocity of the earth's rotation, and ϕ is the latitude of the station,

δ is the geopotential anomaly, and

p_1 and p_2 are the pressure levels between which δ is determined.

To allow for the greatest possible data coverage, geostrophic velocities were calculated relative to the 900 db pressure level because most of the CTD casts were done to this depth or more.

Altimeter Data

The images representing the altimeter data were downloaded from the web pages of the Colorado Centre for Astrodynamic Research (CCAR – <http://www-ccar.colorado.edu>). The CCAR's Altimeter Data Archive Home Page provides the user with altimeter data visualization and processing software. At this website maps of sea surface height anomaly can be viewed for any region in the global ocean (60°S to 60°N latitude). Alternately, sea surface height can be viewed using a mean circulation derived at the Naval Research Laboratory (NRL) at Stennis Space Center in Slidell, Mississippi. The maps are produced from TOPEX, ERS-1, and ERS-2 altimeter data using geophysical data records (GDR's). An analysis product is produced every three days, based on the latest 10 days of TOPEX and/or 35 days of ERS-2 sampling if available. The historical product is designed to retain the mesoscale sea surface height anomalies associated with fronts and eddies. The data available at this site covers the period from 1 May 1994 to 22 May 1998.

Real-Time Geophysical Data Records (RGDR's) are based on ESA's Fast-Delivery (URA) product, which is received at NOAA within 6 hours of satellite acquisition. Since the URA data contain only crude satellite state vector information, the most important step in RGDR production is the addition of orbital information from ephemerides computed by the Delft Institute for Earth-Oriented Space Research. It is necessary to utilize a predicted extension to the computed orbits in order to produce RGDR's on a daily basis (within 12 hours of satellite acquisition). After applying the predicted orbit, NOAA enhances the RGDR with improved geophysical corrections and makes the data available to select real-time users. An Interim GDR can be produced by relaxing the timeliness of data production to three days, making it possible to use the highest precision part of the Delft JGM-3 orbits, rather than the

predicted phase. The RGDR data have relatively large orbit errors, so are most suitable for mesoscale studies with explicit orbit error removal.

The University of Colorado procedure blends ERS-2 and TOPEX altimetry, treating both data sets in a consistent fashion (*Lillibridge et al., 1997*):

- ✧ All TOPEX and ERS-2 data are referenced to the Ohio State University Mean Sea Surface 1995 (*Yi, 1995*). The data are treated as nonrepeat tracks and are referenced directly to the mean sea surface. This saves a significant amount of computation in the near-real-time processing.
- ✧ NOAA provides the following geophysical corrections: ocean + load tides from the University of Texas CSR 3.0 tide model; solid earth tide; ionosphere correction from the IRI90 model; wet and dry troposphere corrections based on NMC model grids; and a wet troposphere correction from the SSM/I sensor onboard the DMSP satellites.
- ✧ Along-track "loess" filtering is used to remove orbit and environmental correction errors. Loess filtering is a running least squares fit of a tilt plus bias, within a sliding window. The window width is approximately 15 degrees of latitude, to retain mesoscale signals.
- ✧ A fast, multigrid preconditioned Cressman analysis is used for interpolation to a quarter-degree grid (*Hendricks et al., 1996*).
- ✧ Finally, a model mean is added to the sea surface height anomaly to produce an estimate of the total dynamic height.

AVHRR DATA

SST Global Area Coverage (GAC) processing of Pathfinder AVHRR data

All Pathfinder GAC 4.0 data distributed by the NASA Jet Propulsion Laboratory Distributed Active Archive Centre [JPL DAAC] are processed at the University of Miami before release for distribution (http://www.rsmas.miami.edu/groups/rrsl/pathfinder/Processing/proc_index.html). The data processed for the Pathfinder Oceans program is obtained by the Advanced Very High Resolution Radiometer

aboard polar-orbiting satellites of the NOAA series. All processing of GAC 4.0 data occurs in a four step procedure:

- *Ingestion, calibration and navigation of GAC data.*

During this step orbit information of files containing approximately one orbit of GAC coverage is collected by a procedure called SCAN. This information is then used during the ingestion step in a procedure called INGEST to split the orbit file into several ascending and descending pieces, as well as to reformat the data for input to the atmospheric correction and SST calculation procedure (ATCOR).

- *Pathfinder SST calculation.*

The ATCOR procedure reads the navigation and radiance data of all five AVHRR channels contained in a piece. And then applies the algorithm to calculate the Pathfinder SST value. Several quality tests are performed on a pixel by pixel basis and each pixel is assigned an overall quality level ranging from 0 (poor) to 7 (best).

- *Spatial binning.*

In this processing step, all pixels in a piece are binned into an equal-area global grid. The spatial gridding scheme adopted for AVHRR Pathfinder Oceans processing is based on the equal-area grid adopted by the International Satellite Cloud Climatology Project (ISSCP). The equal area grid adopted consists of rectangular bins or tiles (approximately 9.28 km per side at the Equator), arranged in zonal rows. During assignment to a given spatial bin only pixels of the highest available quality level are summed, i.e. the binning procedure considers only the best data for a given bin.

- *Temporal binning and the accumulation of daily global fields.*

The spatially binned ascending or descending pieces of a given data-day are then binned in time to produce interim global ascending or descending fields at daily or other resolutions. In low latitudes there is no spatial overlap between ascending and descending passes in a given data-day, therefore bins in a daily product only have pixels from a single piece. At higher latitudes there may be

spatial overlap between passes and the selection of data to be binned in time is then performed in the same way as in the spatial binning.

Processing of AVHRR data at UCT

The SST data analysed at UCT was obtained by the AVHRR sensor aboard NOAA 14. Both the visible and infrared images are received from the Satellite Applications Center (SAC) at Hartebeesthoek, Pretoria, where the images have been calibrated from AVHRR channels 1, 4 and 5, and geo-corrected to a Clarke 1880 Mercator Projection. The SAC is operated as a facility for the reception, processing, archiving and distribution of satellite data.

At UCT the image files have been imported to an image processing package called Imagine on a UNIX system. The files were then exported as flat raster binary files to a PC environment for processing by the PC-SEAPAK image processing package. PC-SEAPAK was developed at the NASA (National Aeronautics and Space Administration) Goddard Space Flight Centre (*Firestone et al., 1990; McClain et al., 1992; Darzi et al., 1991*). The image data files were then ingested and transformed to SEAPAK format, such that $SST(^{\circ}C) = \text{pixel value} * 0.127 - 0.254$. Corresponding visible band images were used to identify clouds on the infrared images and the pixels which were identified as cloud on the infrared images were all set to one value (masked out). A file representing coastline and land values was also imported from Imagine and a similar procedure to the cloud removal was followed in masking out the land. The next step involved creating a suitable colour palette to represent SST and which would help to identify mesoscale oceanographic structures from the SST. As mentioned in chapter 3, section B, the SST values are accurate within $<0.5^{\circ}C$.

An approximation to the “Zebra Palette” (*Hooker and Brown, 1994; Hooker et al., 1995a and Hooker et al., 1995b*) has been applied to the thermal images to facilitate structure and flow identification. The palette used in this investigation is only an approximation to the zebra palette because SEAPAK only uses 8-bit colour, and so does not permit complicated palette manipulation (32 colours maximum). An appropriate method for creating a similar effect using the SEAPAK image processing

software was devised. The temperature range applicable to the identification of the dipole was established (18°C to 24°C) and the corresponding pixel values identified. Pixel values representing data on the images range from 0 to 255. The pixel values representing the dipole temperature range are then stretched so that each 1°C in that range is represented by 15 pixel values, which can be placed in 5 colour boxes of 3 integer values each. A maximum of 32 colour boxes are allowed during palette manipulation in SEAPAK. Thus selecting 4 temperature slots, e.g. 18°C to 21°C, will occupy 20 colour boxes and the remaining 12 boxes have to be utilized to represent the remaining data on the image. Four such palettes were created so that the zebra portion could represent the range 18°C to 24°C, thus allowing the dipole structure represented by the temperature tracer to be examined more closely.

In order to confirm that the two adjacent vortices constituted a dipole system, it was necessary to establish the rotation rate of the secondary vortex (cyclone) around the primary vortex (anticyclone), i.e. as opposed to a random interaction between a cyclone of South Atlantic origin and an Agulhas ring. The SST gradient images could be used in determining the cyclone rotation around the anticyclone by applying the “separatrice method” as documented by *Hooker et al. (1995a)*. This technique assumes the ring is a dipole system, and thus, 1) a separatrix or dividing line must exist between the two counterrotating velocity fields, and 2) the separatrix must rotate at the same rate as the dipole system. Fluid converges at one end of the separatrix and diverges downstream at the opposite end. A frontal line results from the increased thermal contrast of the converging fluid, flattening the material lines of the fluid and producing a D-shaped primary vortex in the thermal imagery. The changing orientation of this flattened area with respect to an arbitrary reference is taken as the separatrix rotation rate. For the case analyzed in this investigation, the reference is taken to be true north, so that a separatrix rotating anticyclonically in the southern hemisphere has a negative rotation rate.

Chapter 5

Structure of surveyed dipole

In this Chapter, hydrographic and satellite evidence is provided to confirm the hypothesis that a dipole vortex was indeed surveyed by the scientific team onboard the F.R.S. *Africana* in December 1996. Unfortunately, the hydrographic data and the satellite data overlap for only the first two days of the cruise. The most significant overlap is on 20 December 1996 and an overlay of the cruise track on the corresponding infra red image does show that both a cyclonic eddy and an anticyclonic eddy were surveyed hydrographically.

It is appropriate to investigate the AVHRR data first because the regular, quasi-real time monitoring of SST images of the Western Agulhas Bank and Agulhas retroflection region, prompted the initiation of the hydrographic survey conducted on the FRS *Africana*. In the first section of this chapter various features and flow inferences observed on the images of 19 and 20 December 1996 are identified. The aim of this section is to search for evidence of the presence of a dipole vortex in the region surveyed during the “Christmas cruise”. This is followed by the examination of the hydrographic material to support any conclusions drawn from the AVHRR data. The *in situ* data is also used to determine the possible origin of the vortex dipole.

Analysis of AVHRR Data

Figure 5.1 and 5.3 are false colour AVHRR images representing the sea surface temperature observed on 19 and 20 December. An approximated “Zebra Palette” has been applied to both images to assist in flow and structure identification. The colour bar indicates the values of the various SST’s represented on the image, as well as the colours used to mask cloud cover and land. The intersection of latitude and longitude lines on the image are indicated by “+” symbols where they are not labelled. A patch of gray near the upper right hand corner of the images represents the outline of the Saldanha Bay and Cape Columbine region (see *figure 1.3* for orientation). Solid black lines west of the land mass represent the 200 m (difficult to see due to the colour of the SST palette in this

region), 500 m and 1000 m isobaths. In both the images the pseudo zebra palette has been applied in the 18-21°C bracket.

Figure 5.2 and *5.4* represent the sea surface temperature gradient images of *Figures 5.1* and *5.3* respectively. The latitude and longitude intersections are represented in the same way as in the SST images. However, both the land and cloud cover are represented by gray and not indicated on the colour bar. The colour bar represents 0.25°C increments per kilometer.

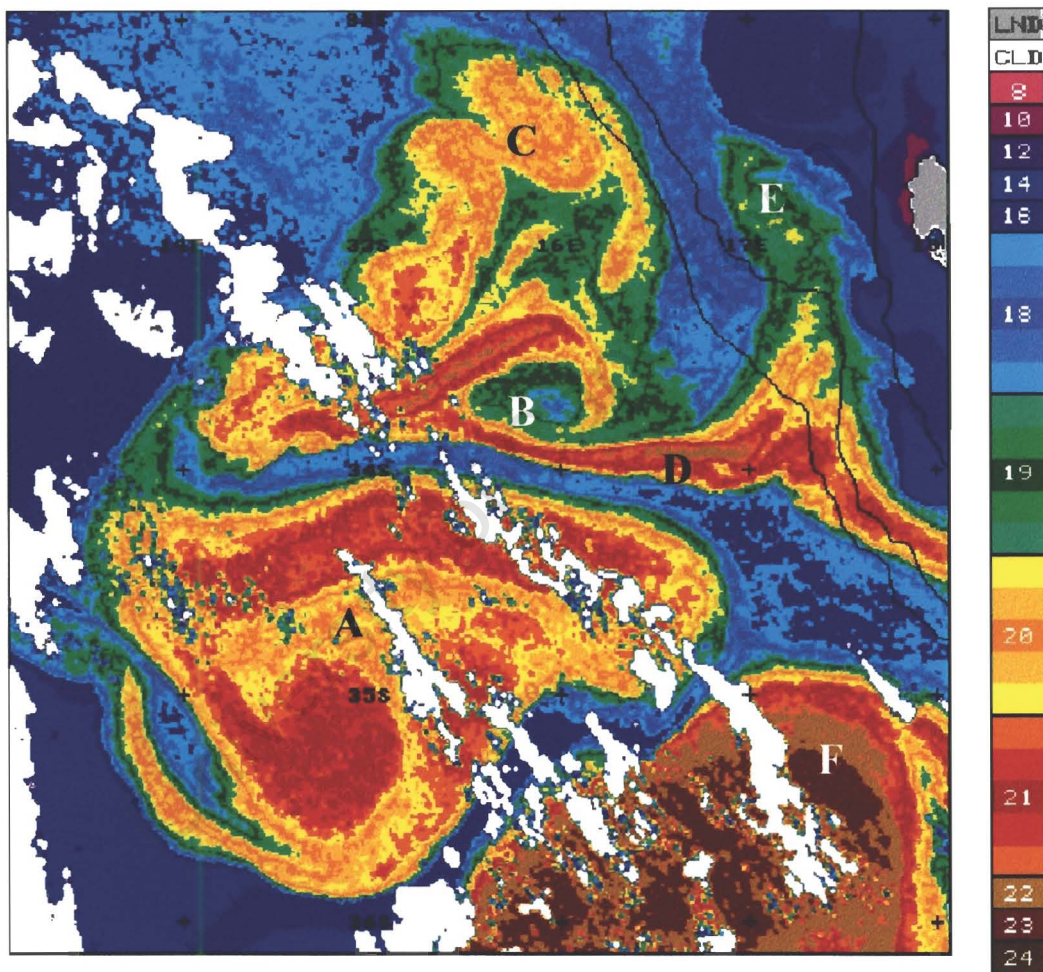


Figure 5.1: AVHRR Sea Surface Temperature Image on 19 December 1996

On 19 December, structures are well resolved on the SST imagery (*Figure 5.1*) and can be observed as warm water (>20°C) embedded in a cooler background ($\leq 18^\circ\text{C}$). The dominant feature on the image is a D-shaped pool of warm water (**feature A**), with the flattened side orientated in an east-west direction. Temperatures within this mass of warm water vary from 19°C at the outer edges to 21°C inside the warm pool. The

warmest regions within this structure are found near the flattened edge and in the rounded body of the “D”. A filament of warm water is seen trailing from the southern most edge of this structure in a north-westerly direction. A similar, although cooler, filament is observed trailing from the north-western edge of the feature. The orientations of these filaments hint at a possible anticyclonic circulation exhibited by **feature A**. Cooler South Atlantic water surrounded the entire D-shaped structure seemingly separating it from any contact with other warmer water. Although the D-shape is anomalous, the temperature characteristics and the location (north of the Agulhas Retroflexion region) of **feature A** suggest that it is a recently spawned Agulhas ring.

North of the Agulhas ring a filament of warm water, which seems to originate from the Agulhas Bank (see *Figure 1.2*), is coiled around a small cooler feature (**feature B**). The temperatures of this filament vary from 22°C in its centre to 19°C at the edges. This temperature signature is consistent with the findings of *Lutjeharms and Cooper (1996)* and suggests that the filament could be of Agulhas Current origin. In *Figure 1.2* the filament could be traced to its origin on the Western Agulhas Bank. The cyclonic coil of the filament around the cooler feature (18°C in its centre) alludes to the presence of a cold core cyclonic eddy on the flattened outer-edge of the D-shaped anticyclonic eddy. Thus two adjacent eddies exhibiting opposing spin can be identified on the image. Water is drawn from east to west between these eddies and there is evidence of both cooler Atlantic water and warmer Agulhas water passing between them. A plume of warm water (**feature C**), with a temperature range of 19-21°C, extends from the west to the north of the cold eddy and spreads out towards the shelf edge.

As the filament passed over the shelf edge it separated into two parts, with one component being drawn westward (**feature D**) by the two eddies and another component moving northward (**feature E**) along the contours of the shelf. Upwelling filaments extending westward across the shelf can also be identified on the eastern side of the northward component of the filament. Strong evidence of upwelling is seen west of Cape Columbine (<12°C water spreading westward). South-east of the anticyclonic eddy a mass of warm water, exhibiting temperatures as high as 24°C, can be identified (**feature F**). Such high sea surface temperatures are characteristic of the Agulhas Current and this mass of warm water could thus either be a meander in the current or a recently spawned ring leaving the Agulhas Current.

The outline of the Agulhas ring, identified on the infra red imagery, is also clearly delineated by sea surface temperature fronts on *Figure 5.2*. Strong fronts are observed on the southern edge ($\geq 2.5^{\circ}\text{C/km}$) and the northern edge ($\geq 0.75^{\circ}\text{C/km}$) of the ring; further emphasizing the strong temperature differences between the Agulhas ring and the surrounding Atlantic Ocean water. North of the front marking the edge of the anticyclonic eddy, two further fronts are observed. The southernmost of the two fronts marks the southern edge of the filament and is traceable to the eastern most edge of the image. It is also the stronger of the two fronts with sea surface temperature gradients greater than 2.25°C/km found between the two eddies, where the front is strongest. The

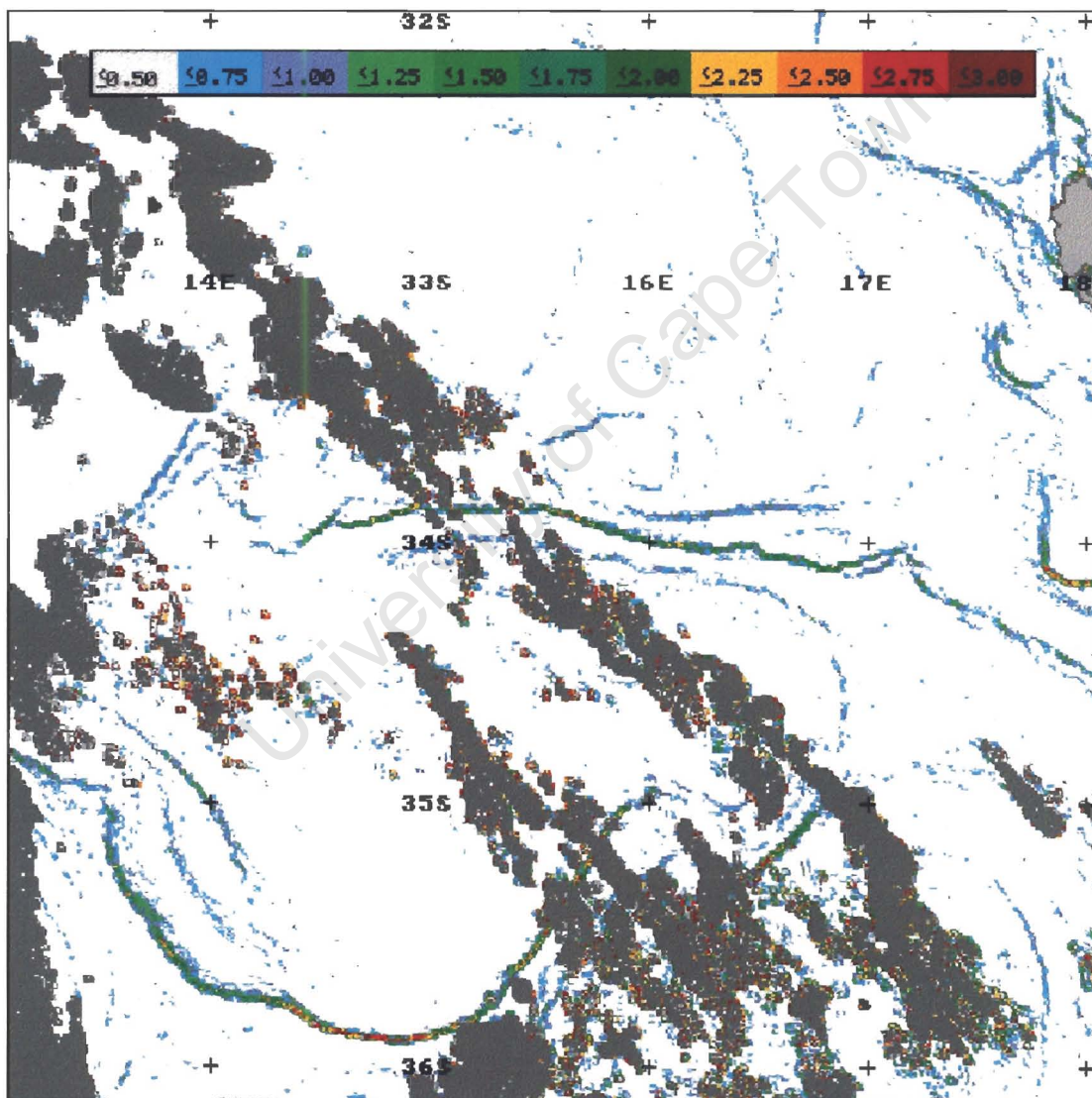


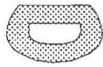
Figure 5.2: *AVHRR Sea Surface Temperature Gradient Image on 19 December 1996. Colour Bar divisions are in $^{\circ}\text{C/km}$.*

the sea surface temperature images. The cyclonic eddy exhibits a 3 km northward and 11 km westward translation in 24 hours, i.e. an approximate resultant translation of 13 cm/s. These results imply that the cyclonic eddy was moving faster in a northwestward direction than the anticyclonic eddy. The calculated translation of the cyclone is perhaps more accurate than that of the anticyclone because the displacement of the cooler central water of the cold core eddy is easily discernable on *Figure 5.3*.

By 20 December 1996 the other features identified on *Figure 5.1* also exhibit some evolution. Along the shelf the component of the filament following the shelf contours (**feature E**) has moved even further north. The difference in the surface signature of this feature on *Figure 5.1* as opposed to its surface signature in *Figure 5.3* is quite striking. In *Figure 5.3* there is evidence of sea surface cooling of the waters identifying **feature E** due to heat loss to the atmosphere. This northward component could be the result of part of the filament being “poached” by the shelf edge jet described by *Shannon and Nelson (1996)*. The tongue of upwelled water issuing forth from Cape Columbine also extends further northward (*Figure 5.3*) and the fronts representing the edges of tongues of upwelled water have become more extensive along the eastern edge of the northern component of the filament (*Figure 5.4*). A continued northward spread of the plume of warm water (**feature C**), north of the cyclonic eddy, is also evident. This flow is indicative of the background Benguela Current flow as described by *Peterson and Stramma (1991)*.

In the analysis of the AVHRR data presented in this section, SST has been used as a surface tracer to identify various phenomena occurring in the southeast Atlantic Ocean. The next objective would be to determine whether any of these observations reflect the characteristics of a dipole vortex, i.e. whether the two eddies form part of one translating system. Various observations made from the AVHRR data support this hypothesis.

- Two eddies of opposing temperature characteristics are observed adjacent to each other, i.e. a warm and cold eddy pair.
- Water is entrained between the two eddies and there is a convergence of fluid on the eastern side of the eddy pair, with divergence on the western side.
- Both of the eddies exhibit an overall northwestward translation.

- The larger of the two eddies has a flattened edge and its overall shape resembles the letter ‘D’ lying face down, i.e. , similar to material line observations made by *Hooker et al. (1995b)*.

All these characteristics were also observed by *Hooker and Brown (1994)* and *Hooker et al. (1995b)* when they described the translation history of ‘Warm Core Ring 82-B’ (WCR 82-b). They were also able to describe the rotation rate of the dipole system in which WCR 82-B was the primary vortex. This was achieved by using the separatrix method (described in Chapter 4). As described earlier, fluid converges at the one end of the separatrix and diverges downstream at the opposite end. The frontal line established by the converging fluid is clearly identifiable between the eddies as the southern edge of the filament (*Figures 5.2 and 5.4*) and the section of this front that is most perpendicular to the line connecting the (approximate) centres of the two vortices is estimated. Along the straightest portion of the front, two digitized end-points (as far apart as possible) are connected with a chord, which then represents the separatrix. The change in the angle of the separatrix (clockwise from true north) is then directly related to the rotation of the secondary vortex around the primary vortex.

This method was applied to the satellite imagery of 19 and 20 December 1996. The orientation of the separatrix was 107.6° from N (clockwise) on the 19th and 99.0° from N on the 20th. Assuming that the eddy pair is a dipole system, then the secondary vortex is rotating around the primary vortex at $8.6^\circ/\text{day}$ in an anticlockwise direction. However, this measurement was taken from a ‘snapshot’ (i.e. short timescale) of the total development of this dipole system and should not be regarded as definite affirmation of the rate of rotation of this dipole system, but solely as the confirmation of an anticyclonic rotation of the cyclonic eddy around the anticyclonic eddy. There is thus ample evidence to suggest that the eddy pair surveyed hydrographically by the FRS *Africana* does indeed constitute a dipole system. The investigations of *Hooker et al (1994, 1995a, b)* delved extensively into the origin and translation of WCR 82-B in order to provide strong evidence of the dipole nature of that particular system from satellite imagery. A similar commitment is required here and a more complete history of the origin and the development of this dipole will be provided in Chapter 6.

Hydrographic Data

In this section the hydrographic observations made during Voyage 138 of FRS *Africana* are presented and discussed in detail. Although the overlay of the cruise track on the infra red images examined in the previous section does indicate that both eddies were surveyed hydrographically, it is important to consider that the two features show a marked north-westward drift on the images, and the cyclone rotates anticyclonically around the anticyclone. *Table 5.1* provides information about the CTD stations pertinent to this investigation. It is evident from the table that CTD stations 13 to 17 provide information directly comparable to what is observed on the AVHRR data of 20 December 1996. The observer has to allow for rotation of the cyclonic eddy when considering the rest of the CTD stations.

CTD Stations	Latitude	Longitude	Date
13	34.371 °S	17.284 °E	20/12/96
14	34.373 °S	16.883 °E	20/12/96
15	34.373 °S	16.278 °E	20/12/96
16	34.567 °S	15.718 °E	20/12/96
17	34.908 °S	14.820 °E	20/12/96
18	34.411 °S	14.972 °E	21/12/96
19	34.099 °S	15.085 °E	21/12/96
20	33.936 °S	15.116 °E	21/12/96
21	33.609 °S	15.247 °E	21/12/96
22	33.339 °S	15.342 °E	21/12/96
23	33.333 °S	14.731 °E	21/12/96
24	33.660 °S	14.623 °E	22/12/96
25	33.979 °S	14.521 °E	22/12/96
26	34.298 °S	14.416 °E	22/12/96
27	34.634 °S	14.414 °E	22/12/96
28	34.971 °S	14.417 °E	22/12/96
29	34.641 °S	14.876 °E	22/12/96
30	34.304 °S	15.352 °E	22/12/96
31	34.047 °S	15.625 °E	23/12/96
32	33.749 °S	15.804 °E	23/12/96
33	33.752 °S	16.214 °E	23/12/96
34	33.751 °S	16.614 °E	23/12/96
35	33.754 °S	17.023 °E	23/12/96

Table 5.1: *The position and time at which the CTD dips, relative to this investigation, were made.*

The XBT positions are provided in *Table 5.2*.

XBT Stations	Latitude	Longitude	Date
1	34.372 °S	17.426 °E	20/12/96
2	34.370 °S	17.069 °E	20/12/96
3	34.353 °S	16.656 °E	20/12/96
4	34.368 °S	16.476 °E	20/12/96
5	34.436 °S	16.085 °E	20/12/96
6	34.500 °S	15.891 °E	20/12/96
7	34.617 °S	15.538 °E	20/12/96
8	34.696 °S	15.350 °E	20/12/96
9	34.780 °S	15.136 °E	20/12/96
10	34.836 °S	15.001 °E	20/12/96
11	34.728 °S	14.876 °E	20/12/96
12	34.549 °S	14.932 °E	21/12/96
13	34.245 °S	15.015 °E	21/12/96
14	33.934 °S	15.116 °E	21/12/96
15	33.765 °S	15.187 °E	21/12/96
16	33.423 °S	15.314 °E	21/12/96
17	33.324 °S	15.129 °E	21/12/96
18	33.339 °S	14.931 °E	21/12/96
19	33.498 °S	14.698 °E	21/12/96
20	33.823 °S	14.572 °E	22/12/96
21	34.132 °S	14.444 °E	22/12/96
22	34.468 °S	14.415 °E	22/12/96
23	34.802 °S	14.406 °E	22/12/96
24	34.857 °S	14.575 °E	22/12/96
25	34.741 °S	14.722 °E	22/12/96
26	34.521 °S	15.041 °E	22/12/96
27	34.412 °S	15.194 °E	22/12/96
28	34.188 °S	15.483 °E	23/12/96
29	33.906 °S	15.712 °E	23/12/96
30	33.753 °S	16.011 °E	23/12/96
31	33.751 °S	16.412 °E	23/12/96
32	33.748 °S	16.828 °E	23/12/96
33	33.761 °S	17.206 °E	23/12/96
34	33.778 °S	17.422 °E	23/12/96

Table 5.2: *The position and time at which the XBT probes, relative to this investigation, were launched.*

CTD/XBT Map

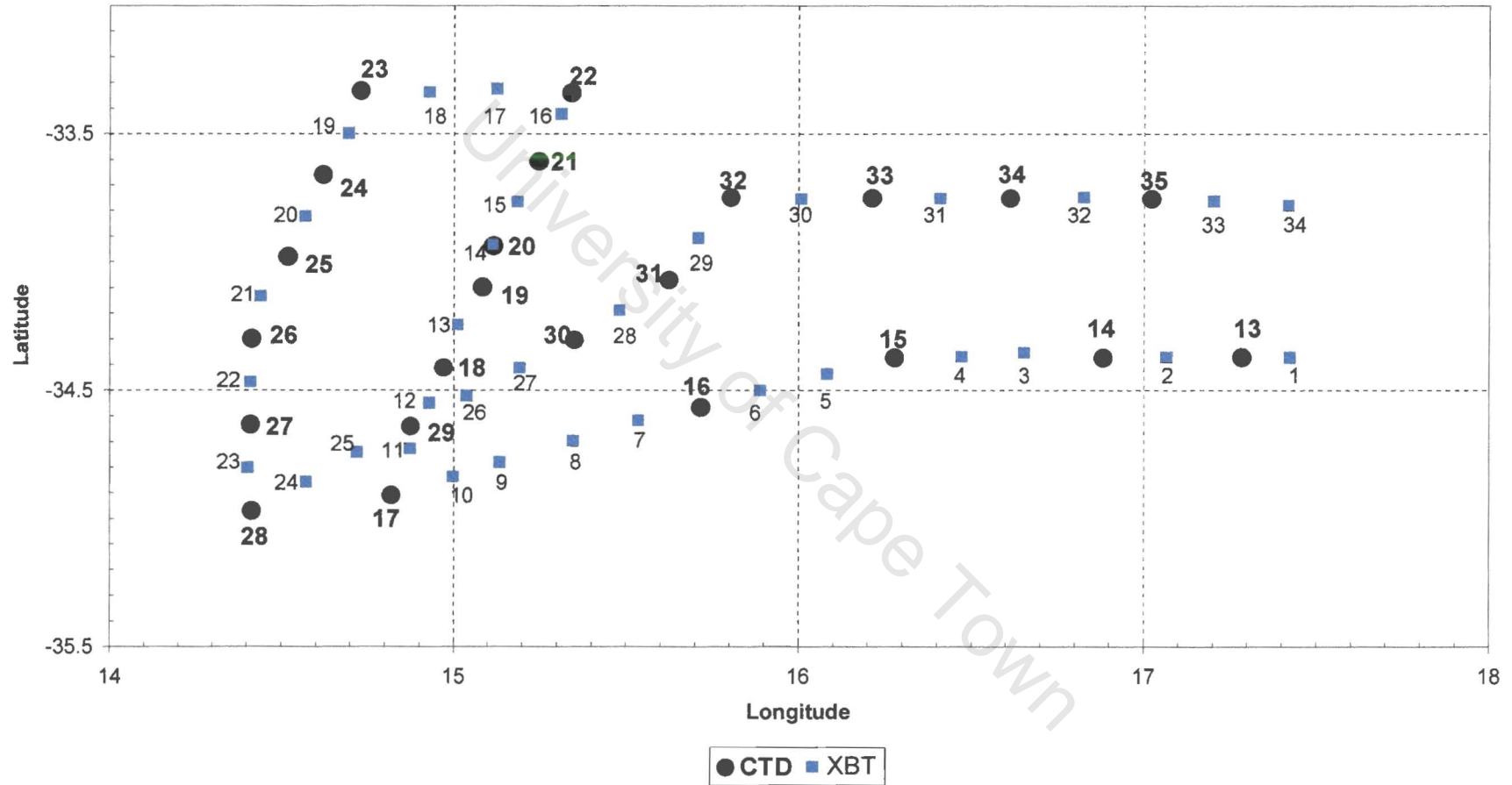


Figure 5.5: Map of relevant CTD and XBT stations

All the positions of the CTD and XBT stations relevant to this investigation are represented in *Figure 5.5*. The stations have been plotted on an Xcel graph to facilitate their identification in horizontal sections that will be discussed later in this chapter. Horizontal sections, representing temperature at the 500 m depth level and the depth of the 27 kg/m^3 surface, will be examined for traits that would suggest the presence of a dipole vortex. These sections are then compared to the AVHRR satellite images presented in the first section of this chapter (*Analysis of AVHRR Data*), so that the overlap of the positions of the vortices identified from one source can be compared with the other. A good overlap will infer efficient hydrographic sampling, thus implying that the information represented in the vertical sections will be a reliable reflection of the dipole structure. The vertical sections were chosen so as to best represent the physical structure of the respective eddies constituting the dipole. Vertical sections of temperature, salinity, potential density and geostrophic velocity are analyzed. Lastly various ring-scaling parameters are calculated so that these parameters can be used for comparison with previously identified Agulhas rings in the South-west Atlantic region.

Horizontal Sections

Even though there was some translation of both eddies during this survey, the period of the survey was short enough, and the transect grid was spaced well enough, so that horizontal sections of the *in situ* data should make the features identified on the satellite imagery identifiable in the water column. The most direct comparison between the AVHRR data and the *in situ* data would be to compare the sea surface temperature images to a horizontal temperature section that also reflects the same features in the water column.

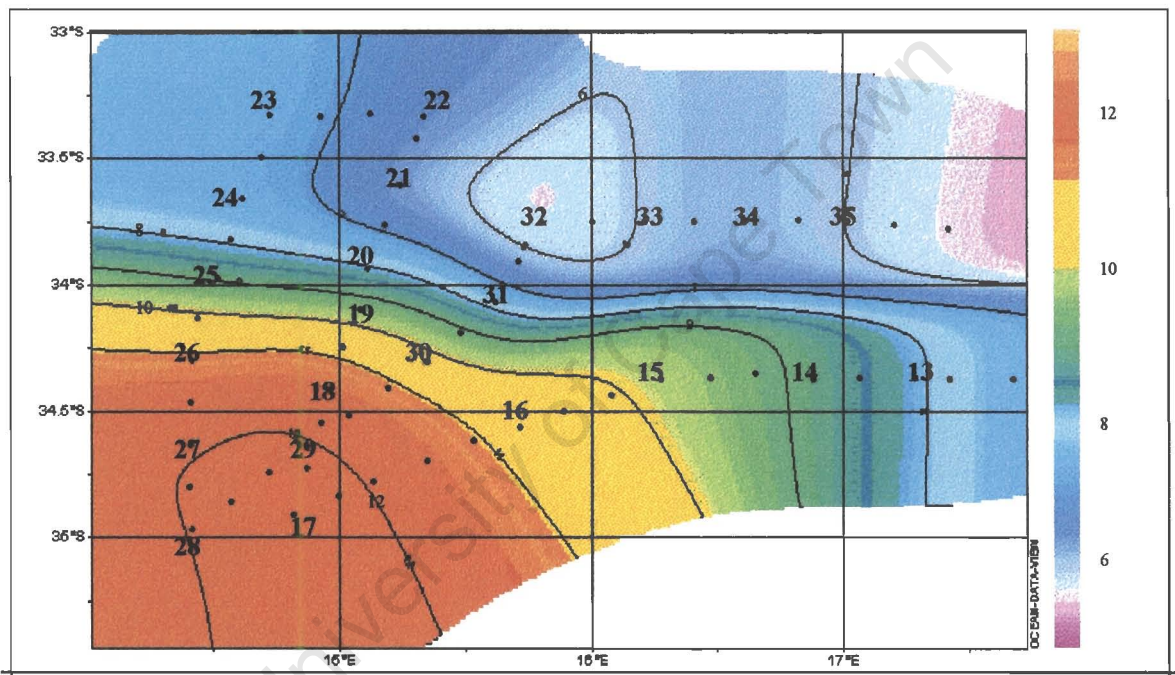


Figure 5.6: Isotherms in 1°C intervals at 500 m depth for the region surveyed by the FRS Africana. The positions of the XBT's and CTD's along the cruise track are indicated with a "•", and the CTD's are numbered.

The temperature distribution at 500 m depth (Figure 5.6) mirrors the sea surface temperature images of 19 and 20 December 1996. Both the anticyclonic and the cyclonic eddy are represented in the temperature field. At this depth level the edge of the Agulhas ring is marked by the 9°C isotherm and it also indicates that the northern edge of the ring is flattened in an east-west direction. The highest temperature (12.31°C) at this depth was recorded at XBT 11. This and other measurements (XBT 9, 10, 25 and 24; CTD 17) in the vicinity of this station, suggest that the ring was centred near 15° E / 35° S at the

time of the survey. The cold core eddy is represented by a pool of cold water that is delineated by the 6° C isotherm. A minimum temperature of 5.33° C was measured at CTD 32 and this suggests that the cold core eddy was centred near 15.8° E / 33.74° S.

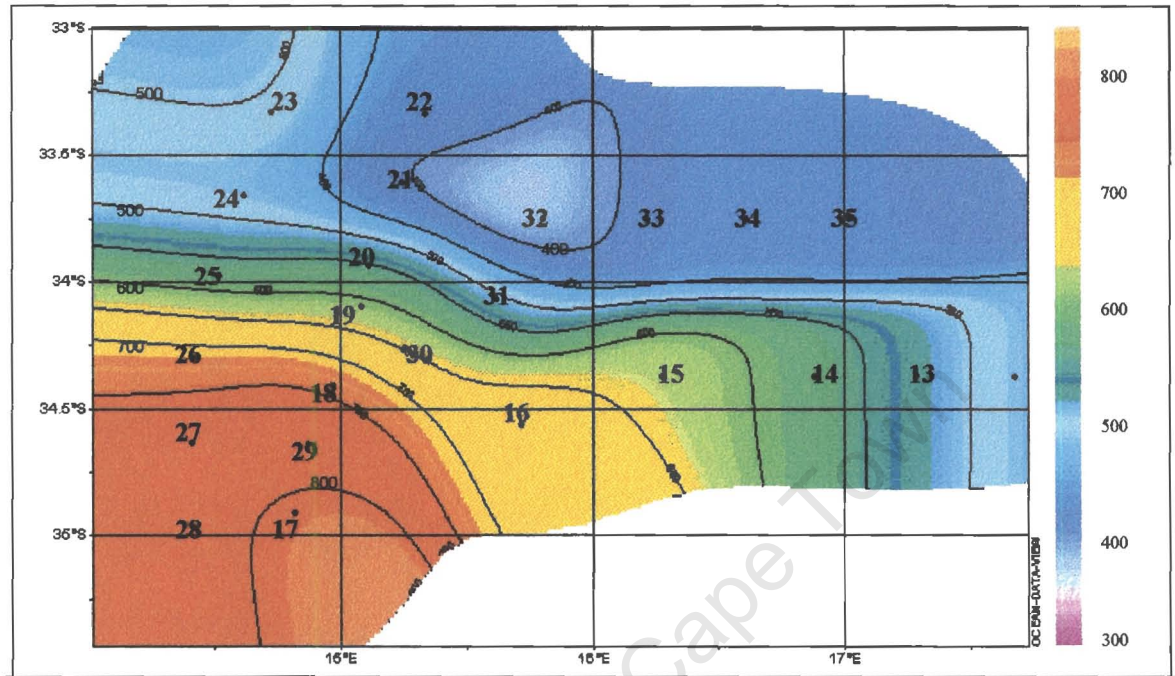


Figure 5.7: *Depth of the 27 kg/m³ σ_{θ} surface (potential density) in 50 m contour intervals.*

The change in elevation of potential density surfaces provide clues to the circulation patterns in the survey region and the 27 kg/m³ isopycnal was selected to illustrate the presence of the two eddies. In *Figure 5.7* a peak (<400 m below the surface) of the isopycnal surface marks the presence of the cold core eddy and a depression (>750 m below the surface) is evident in the vicinity of the centre of the Agulhas ring. The slopes represented by these contours indicate that the strongest geostrophic (westerly) flows are expected between the two eddies and the flow directions concur with the expected flows around the respective eddies.

Both these horizontal sections confirm the observations made from the AVHRR images and also suggest the presence of a dipole vortex system.

Vertical Sections

The survey grid criss-crossing the two eddies was divided into vertical sections constructed from the *in situ* data so that 'slices' of information about the physical character of the two eddies could be studied. Four sections were chosen for the examination of the temperature, salinity and potential density characteristics. These physical characteristics were further used to calculate geostrophic velocities between CTD stations within each section. The sections were chosen in such a way as to facilitate the interpretation of the *in situ* data with respect to the dipole structure.

Transect 1

Transect 1 represents CTD stations 13 to 17 and XBT stations 1 to 10 for the temperature profile. The salinity, potential density and geostrophic velocity profiles were only constructed from the CTD data. *Figure 5.8(a)* shows the structure of the Agulhas ring from approximately the centre to the eastern most edge of the ring, as well as the presence of the warm filament.

The upper 100 m layer was well-mixed with a peak temperature of 21° C between CTD 16 and 17. Cooler 18° C water is centred on CTD 14 and the strong slope of the isotherms between CTD 15 and 14 marks the edge of the Agulhas ring in the upper 100 m layer. Eastward of CTD 13 there is again an increase in the temperatures in the upper 100 m and this marks the presence of the filament originating from the Agulhas Bank (as seen on *Figure 1.2*). The cooler water centred at CTD 14 could indicate the presence of south Atlantic water between the warm filament and the ring. At depth (>200 m) there is a general depression of the isotherms and this is a characteristic of warm core rings (*Olson, 1991*). Considering that a surface temperature front occurs between CTD 14 and 15, it is possible to conclude that the edge of the ring can be located somewhere between these two stations. If XBT 4 is considered to be representative of the edge of the eddy and CTD 17 represents the centre, then the observed radius of the eddy is approximately 163 km. The 10° C isotherm is depressed by 200 m at the centre of the ring and the temperature difference between the edge and the centre of the ring at a level surface of 500 m is 2.5° C.

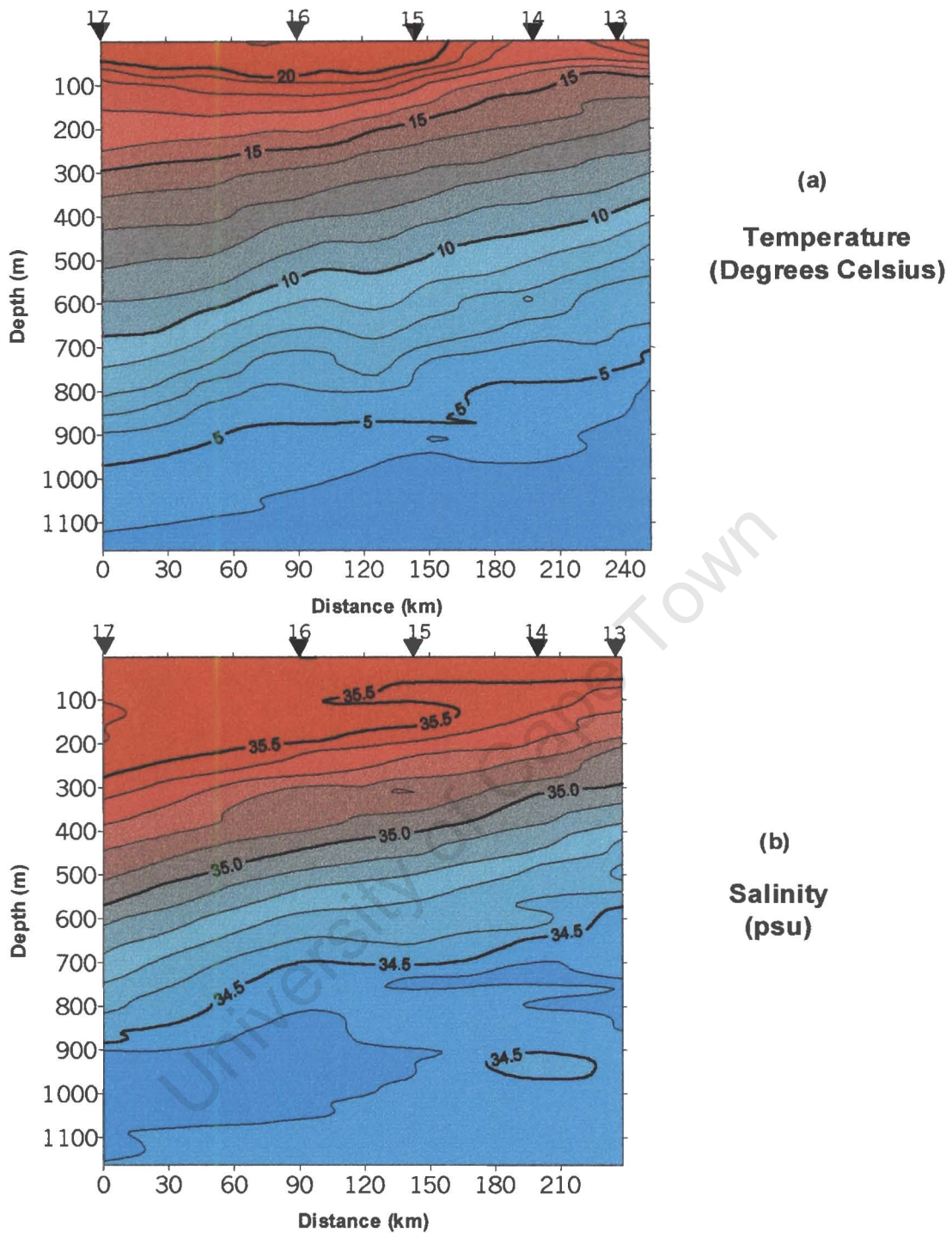


Figure 5.8: Vertical temperature (a) and salinity (b) sections derived from XBT and CTD measurements taken from FRS Africana in December 1996.

The salinity section (Figure 5.8(b)) indicates a mostly isohaline layer of 35.5 psu up to a depth of approximately 250 m at CTD 16. At CTD 17 however, a salinity maximum of 35.6 psu is observed between 100 m and 200 m. This salinity maximum layer could be more extensive than what it appears to be on the diagram because the lack of information between CTD 17 and 16 influences the accuracy of the contouring between the stations.

A general depression of the isohalines towards CTD 17 is also observed in the salinity section and the difference between the core salinity and the surrounding water is approximately 0.3 psu at the 500 m depth level.

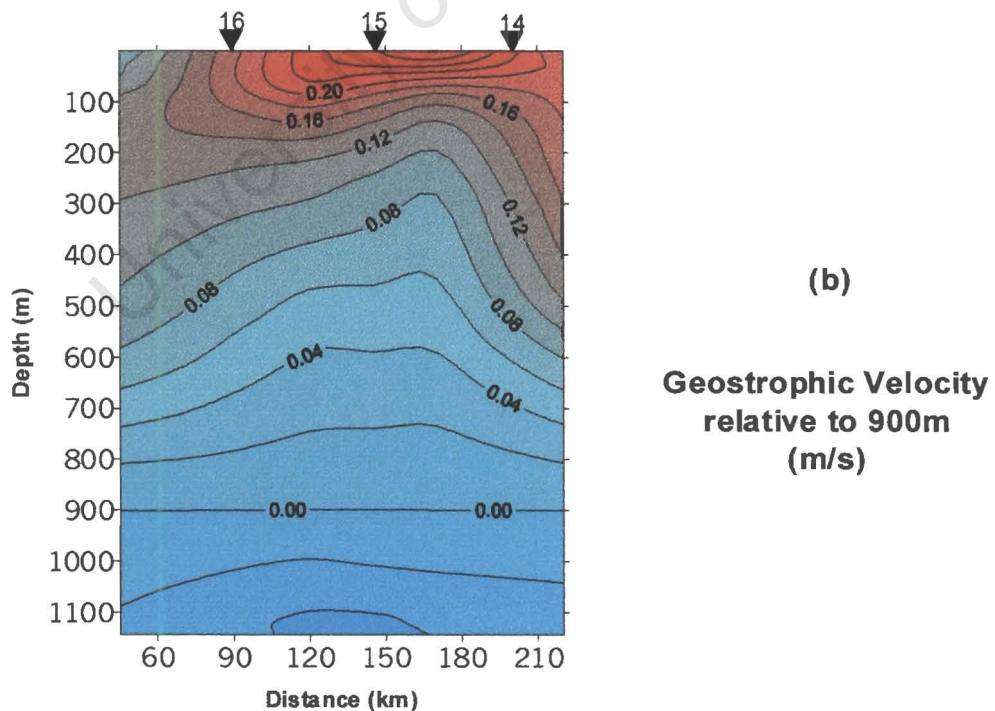
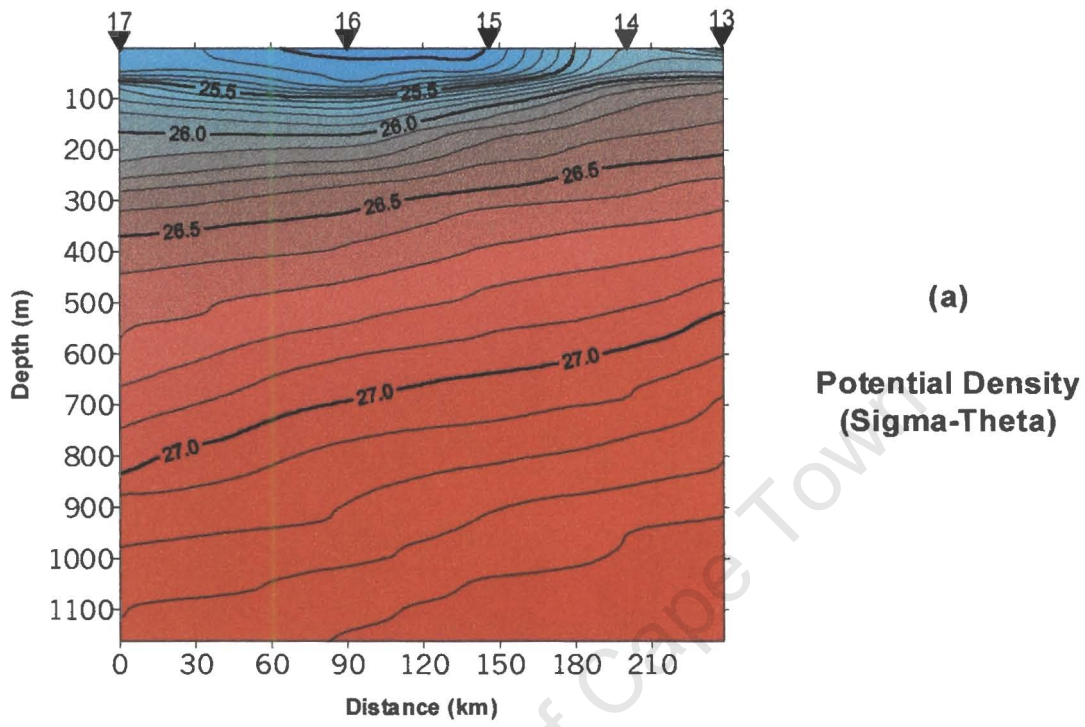


Figure 5.9: Vertical potential density (a) and geostrophic velocity (b) sections derived from XBT and CTD measurements taken from FRS Africana in December 1996.

The slopes and compression of the isopycnals between CTD 15 and 14 (*Figure 5.9(a)*) indicate that the strongest geostrophic flow component could be expected between these stations. Furthermore the deeper sloping isopycnals indicate a general northward flow throughout the water column. The observations made from the potential density section are confirmed in the geostrophic flow section (*Figure 5.9(b)*). A general northward component of flow is evident with the strongest component of flow (26 cm/s) found between CTD 14 and 15 with respect to a level of no motion at 900 m. This stronger flow component with respect to the rest of the section persists throughout the water column, once again marking this region as the outer edge of the ring.

Transect 2

Transect 2 extends from CTD 17 to 22 and includes XBT 11 to 16. This section dissected the Agulhas ring approximately from its centre, crossing the filament between the two eddies and proceeding into the plume exuding behind the cyclonic eddy.

The temperature section *Figure 5.10(a)* reveals various features in the upper 100 m. Firstly, the Agulhas ring can be identified between CTD 17 and CTD 20 (see *Figure 5.6*). The clear upward slope of the isotherms between CTD 19 and 20 marks the edge of the Agulhas ring. An upper mixed layer temperature of 20° C is observed within the Agulhas ring and assuming CTD 20 marks the edge of the surface expression of this ring, then for this section it has a radius of approximately 111.5 km. Although the surface expression is not clear in this section, the warm filament (20° C) was crossed between CTD 20 and CTD 21. Warmer surface water was identified beyond CTD 21 signifying the presence of the warm plume.

There is a strong depression of the 10° C isotherm (272 m) between CTD 20 and CTD 17, with a difference between edge and centre temperatures of approximately 4° C at 500 m. There is thus a stronger expression of anticyclonic ring characteristics in this temperature section than in *Figure 5.8(a)*. A doming of the isotherms is also evident in the deep water (>200 m), centring on CTD 21. Here the 10° C isotherm is elevated approximately 65 m between CTD 21 and the edge of this feature at CTD 22. This doming of the isotherms hints strongly at the presence of a cyclonic feature near CTD 21.

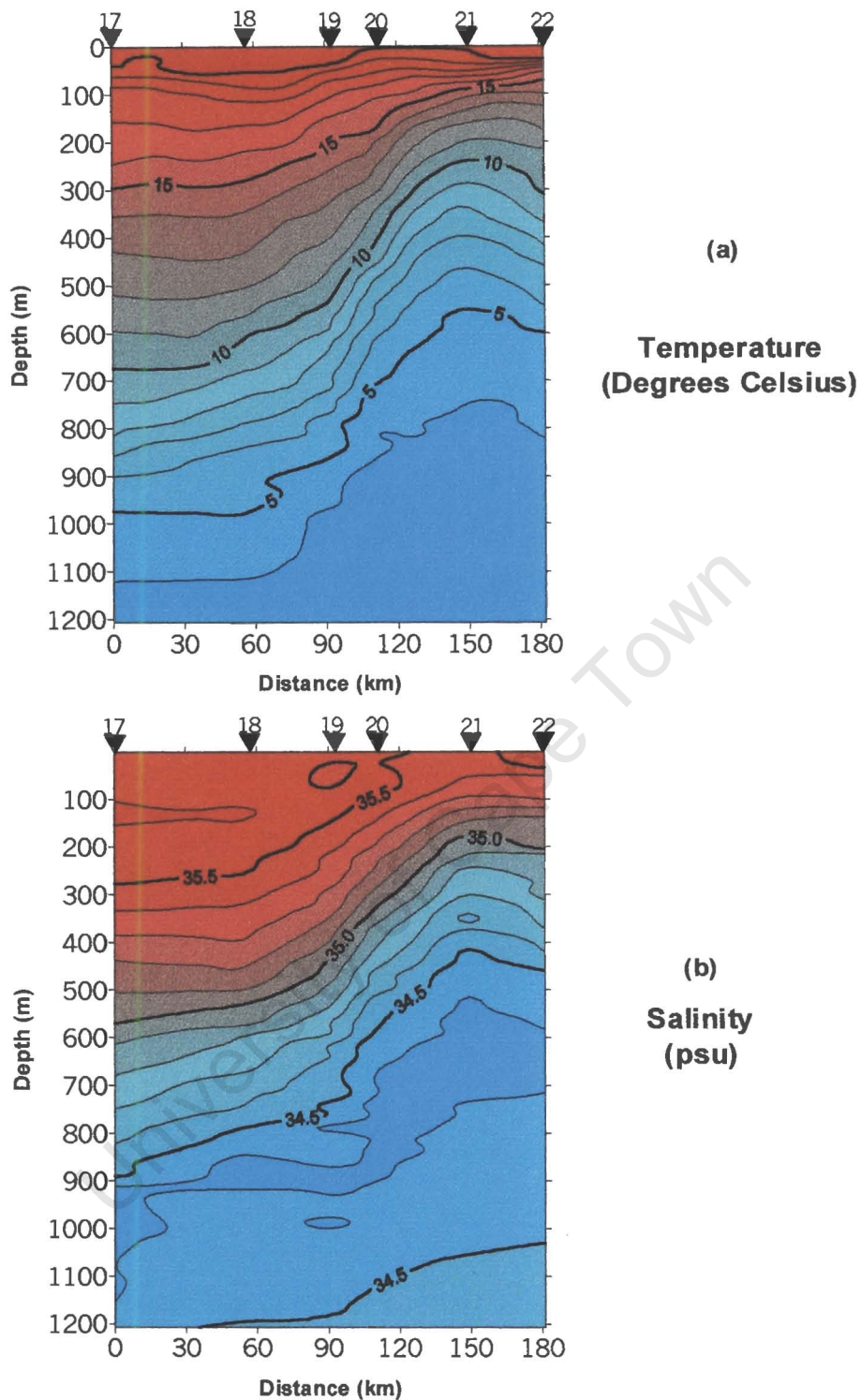


Figure 5.10: Vertical temperature (a) and salinity (b) sections derived from XBT and CTD measurements taken from FRS Africana in December 1996.

In Figure 5.10(b) a salinity maximum of 35.6 psu is observed between CTD 17 and CTD 18 at a depth of 100 m to 150 m. Most of the upper 200 m of the water column between CTD 17 and CTD 20 is a well-mixed isohaline layer with a salinity of 35.5 psu. The 35.5 psu isohaline reaches a maximum depth at CTD 17 and it forms part of a general

depression in the isohalines observed at CTD 17 and CTD 18. Strong slopes observed in the isotherms (*Figure 5.10(a)*) are mirrored in the isohalines (*Figure 5.10(b)*) and the salinity observations confirm the presence of an anticyclonic ring. The difference between the core water and the edge of the ring is 0.5 psu at the 500 m depth level. Doming in the isohalines, although less severe, is also observed in the salinity section, with the maximum doming occurring at CTD 21.

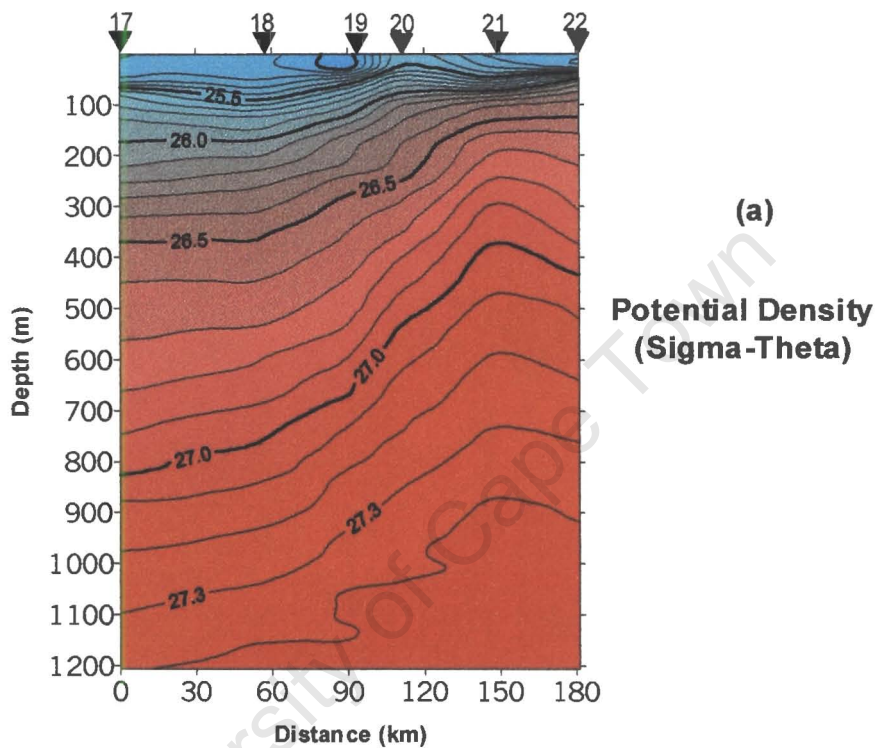
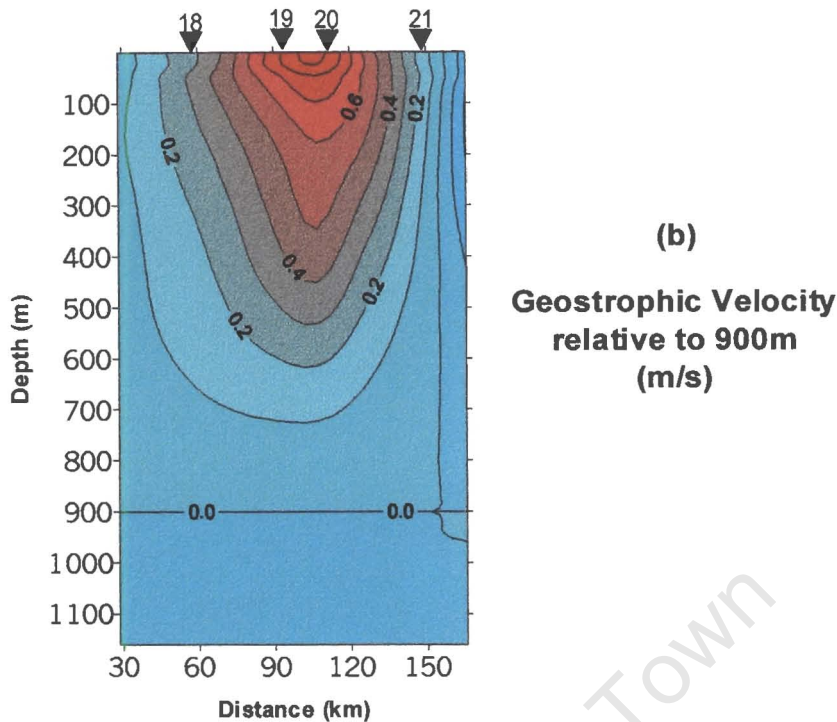


Figure 5.11: Vertical potential density (a) and geostrophic velocity (b) sections derived from XBT and CTD measurements taken from FRS Africana in December 1996.

The slope and compression of isopycnals between CTD 19 and CTD 20 (*Figure 5.11(a)*) suggests that the strongest geostrophic flow can be expected in this region and this is confirmed in *Figure 5.10(b)* with a maximum geostrophic velocity of 0.9 m/s calculated in this region. General westward flow is implied by the deep sloping isopycnals and confirmed in the geostrophic section. The doming observed in the salinity and temperature sections (*Figure 5.10(a) and (b)*) persists in the density section (*Figure 5.11(a)*) as well, and a flow reversal is observed between CTD 21 and CTD 22 (*Figure 5.11(b)*), indicating the eastward part of what would be the cyclonic flow of the cold core eddy. A maximum cyclonic flow (>20 cm/s) is observed between 100 m and 200 m depth.



Transect 3

Transect 3 represents the hydrographic data collected from CTD 22 to CTD 28 and XBT 17 to XBT 23. This transect slices through part of the Agulhas ring in a north-south direction and extends into the plume issuing from the filament drawn between the two eddies. A 90° change in direction, representing an east-west section, occurs from CTD 23 to CTD 22 and is represented by a dashed line on *Figure 5.12 and 5.13*. The orientation of the sections have been chosen so that any flow characteristics derived from the data could be illustrated in a manner consistent with the flow characteristics derived from Transect 2.

A 20° C isohaline layer reaching to a maximum depth of approximately 70 m is observed in the temperature section (*Figure 5.12(a)*) from CTD 28 to CTD 25. Beyond this mixed layer a surface temperature minimum occurs at XBT 20, marking the presence of a cooler filament of water between the plume of warm water and the Agulhas ring. Thus, the surface expression of the Agulhas ring marks the edge of the ring at CTD 25. A shallower mixed layer is observed spanning from CTD 24 to CTD 22 representing the plume resulting from the warm filament. Essentially the same features, concerning the Agulhas ring observed in section 2, are reflected in this section. There is a general depression of the isotherms, but the 10° C isotherm is not depressed as strongly at CTD 28

as at CTD 17, reaching a maximum depression of 208 m. Thus this section is probably not a true radial section. The doming of isotherms observed in section 2 is also visible in this temperature section. It is less severe, however, and the elevation of the 10° C isotherm is only 30 m with respect to the edge of the anticyclonic ring at CTD 25.

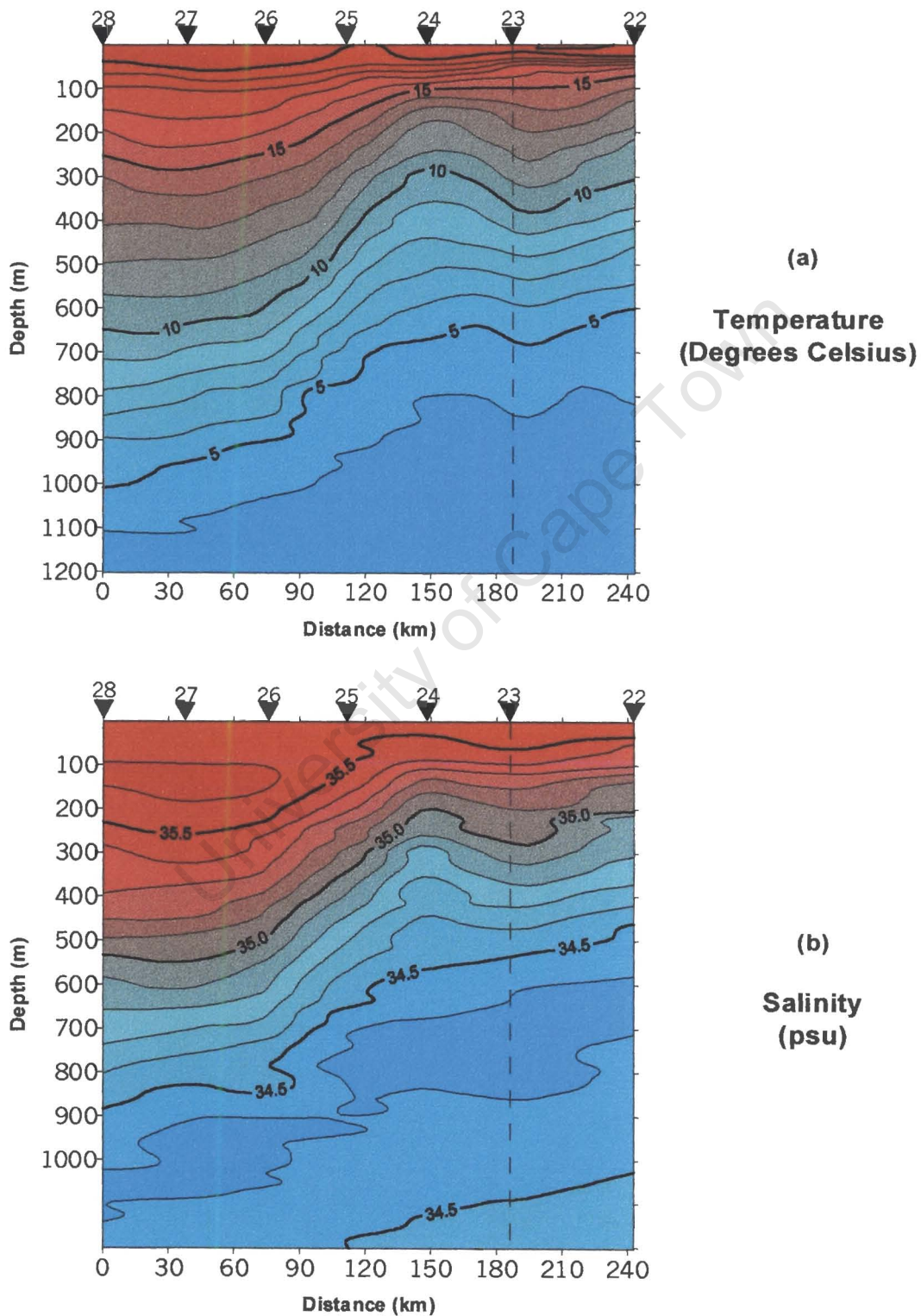


Figure 5.12: Vertical temperature (a) and salinity (b) sections derived from XBT and CTD measurements taken from FRS Africana in December 1996.

A surface mixed layer of 35.5 psu is evident throughout the salinity section (*Figure 5.12 (a)*) and this isohaline is depressed to below 225 m in the vicinity of CTD 28 to CTD 26. There is also a salinity maximum layer (35.6 psu) below the surface at a depth of 100 m to 200 m for these same stations. Again the isohaline section mirrors the character of the isotherms for this section, having a depression and doming of isohalines in accordance with that of the temperature section, providing anticyclonic ring characteristics and a hint of cyclonic ring characteristics.

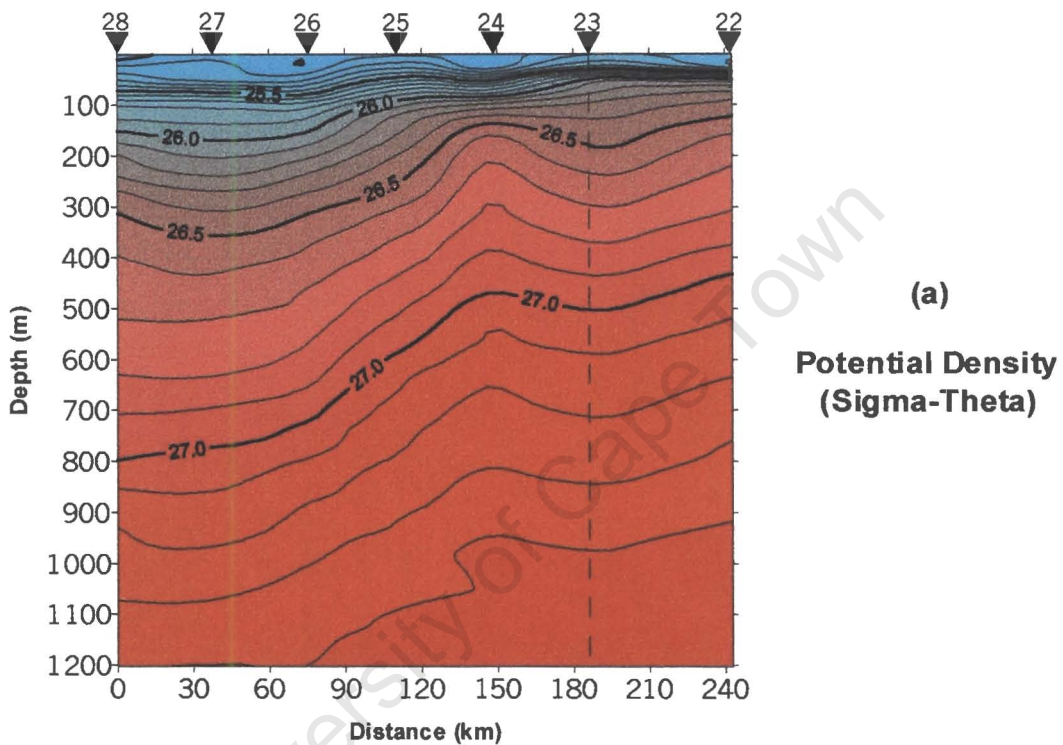
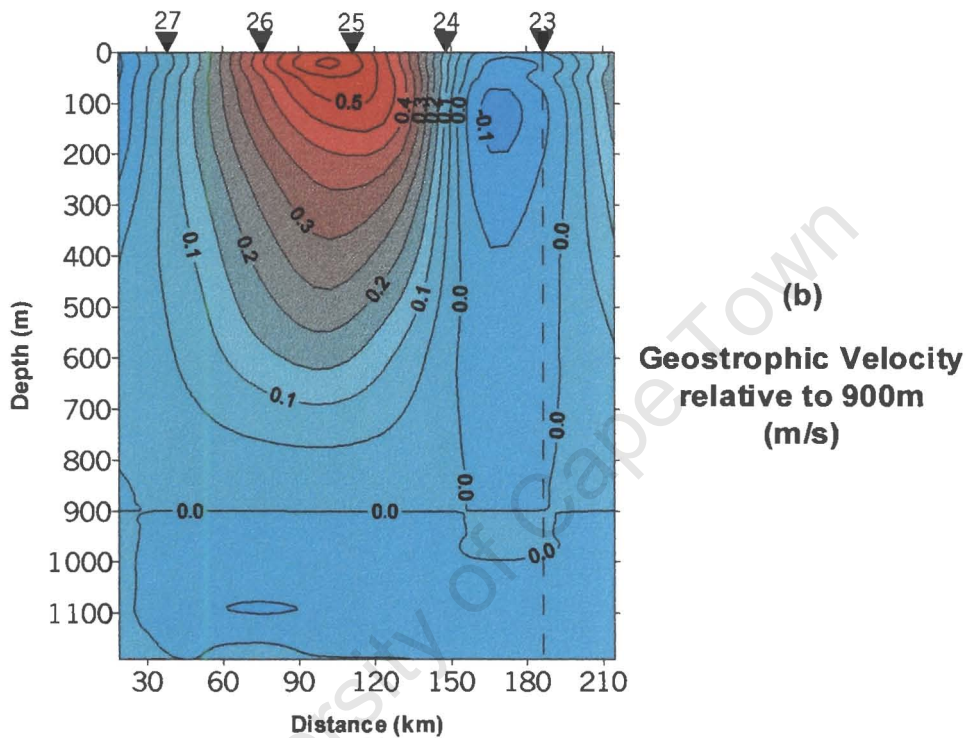


Figure 5.13: Vertical potential density (a) and geostrophic velocity (b) sections derived from XBT and CTD measurements taken from FRS Africana in December 1996.

In the potential density section (*Figure 5.13(a)*) the strongest slopes in combination with compressed isopycnals in the upper 100 m is observed between CTD 26 and CTD 25. The strongest resultant geostrophic flow (*Figure 5.13(b)*) is thus found between these stations and this marks the edge of the ring (as determined from the temperature and salinity sections in *Figure 5.12(a)* and (b)) close to CTD 25. As in section 2, the strongest and most persistent flow throughout the water column is in a westerly direction. Speeds of up to 0.7 m/s were measured between these CTD stations. The density section shows weaker slopes occurring between CTD 24 and CTD 23 as well as a change in slope in the deeper water. There is a reversal of flow and a speed of at least 0.1 m/s was

measured between the 100 m to 200 m depth layers. This could be part of the background Benguela flow mentioned earlier. At CDT 23 the orientation of the section changes to east-west and consequently any positive geostrophic flow will represent northward flow. There is some indication of flow of up to 0.15 m/s in a northward direction. If the geostrophic results between CTD 25 and CTD 24 and CTD 24 and CTD 23 are combined, it would appear that the plume shows a resultant north-eastward drift at these stations.



Transect 4

Transect 4 starts near the centre of the Agulhas ring and proceeds in a north-easterly direction to the vicinity of the centre of the cyclonic eddy, then heads due east. The transect incorporates CTD 28 to CTD 35 and XBT 24 to XBT 34. The direction change occurs at CTD 32 and this station is marked with a dashed line on all the sections.

The temperature section (*Figure 5.14(a)*) reveals a mixed layer of 20°C up to a maximum depth of at least 100 m between CTD 28 and XBT 28. This layer forms the upper part of the circulation of the Agulhas ring. The mixed layer then becomes shallower and the temperature drops to 19° C as the transect crosses the filament and the cyclonic feature. There is a further drop in temperature to 18° C in the upper layer when Atlantic water is encountered followed by an increase in temperature reaching a maximum between CTD

34 and CTD 35. This increase in temperature identifies the northward component of the filament being drawn along the shelf.

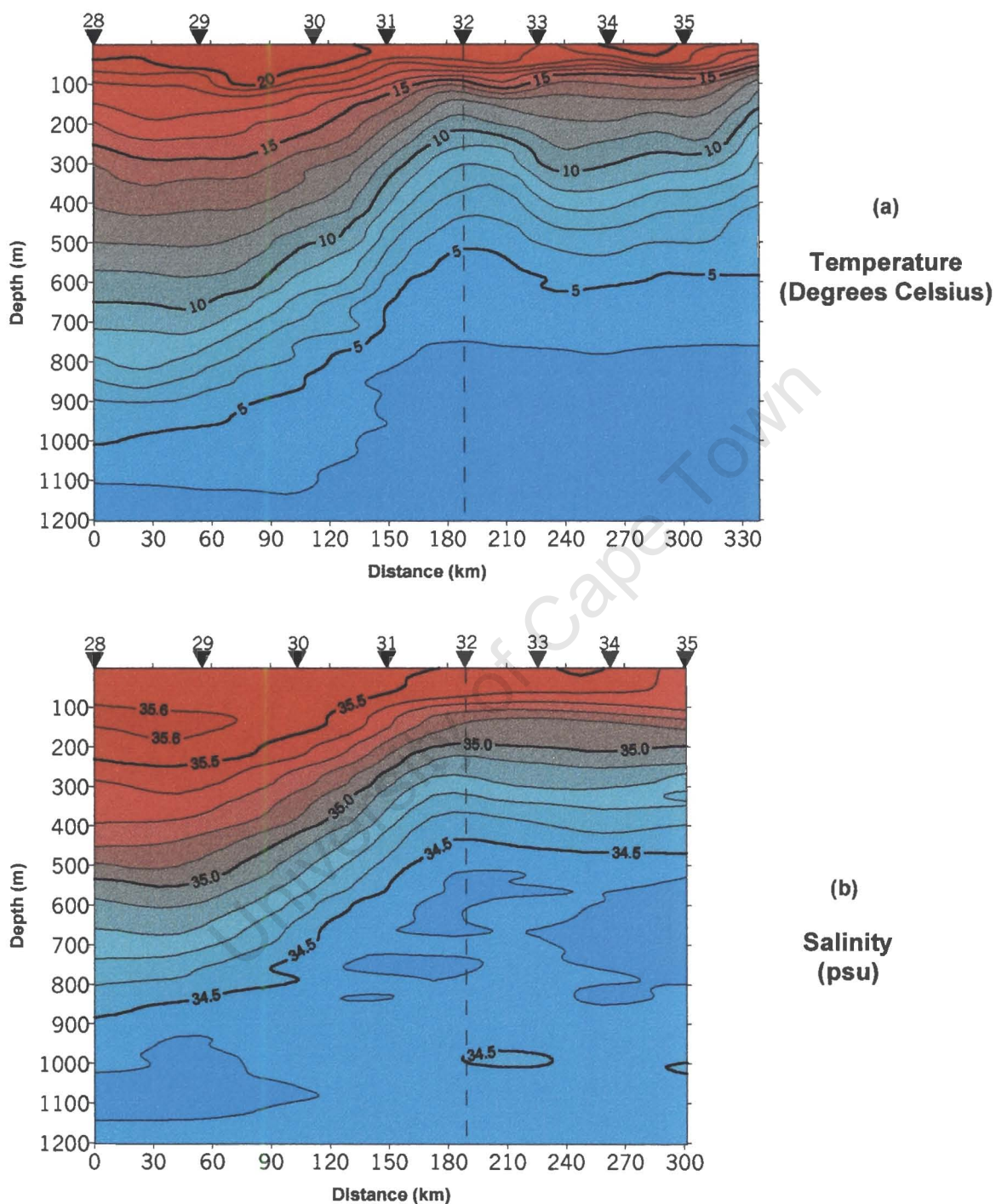


Figure 5.14: Vertical temperature (a) and salinity (b) sections derived from XBT and CTD measurements taken from FRS Africana in December 1996.

The presence of the anticyclonic eddy is again marked by the depression of the isotherms throughout the water column with the depression of the 10° C isotherm reaching a maximum of 667 m below the surface at XBT 25. This amounts to a depression of 317 m with respect to the edge of the eddy at CTD 31. Using the positions of XBT 25 and CTD 31, the radius of the eddy can be estimated as approximately 111 km. At the 500 m depth level a temperature difference of 5° C is measured between the centre of the ring and the edge. The doming of the isotherms observed in *Figure 5.10 (a)* and *Figure 5.12 (a)* is even more prominent in the temperature section of transect 4. Assuming that CTD 32 is close to the centre of the cyclonic ring and that CTD 33 is close to the edge, the 10°C isotherm is elevated at least 96 m due to the eddy presence and a radius of approximately 38 km can be estimated for the eddy.

A salinity maximum of 35.6 psu is again observed in the 100-200 m layer in the salinity section (*Figure 5.14(b)*) and an isohaline surface mixed layer of 35.5 psu is evident at least to CTD 31. The characteristic depression of the isohalines due to the anticyclonic eddy presence is also obvious and the difference between the ring core water and its surroundings is 0.5 psu at the 500 m depth level.

The potential density section (*Figure 5.15(a)*) shows most of the same features described in the temperature and salinity sections. There is a depression of the isopycnals identifying the anticyclonic ring and a slight elevation signifying a smaller and weaker cyclonic feature. The geostrophic velocity section (*Figure 5.15(b)*) reveals the flow characteristics associated with the two eddies. It is important to bear in mind that there is a change in the orientation of the section at CTD 32 and that the diagram represents northwesterly flow positively to the left of CTD 32, and northerly flow positively to the right of CTD 32. A maximum north-westerly flow of 0.7 m/s is calculated between CTD 30 and CTD 31 in the upper 100 m. Southerly flow of at least 0.15 m/s is calculated between CTD 32 and CTD 33 at 100 m depth. Considering the orientation of the transect and the positions of the CTD stations with respect to the two eddies, the geostrophic section reveals a maximum anticyclonic ring velocity of 0.7 m/s and a maximum cyclonic ring velocity of >0.15 m/s.

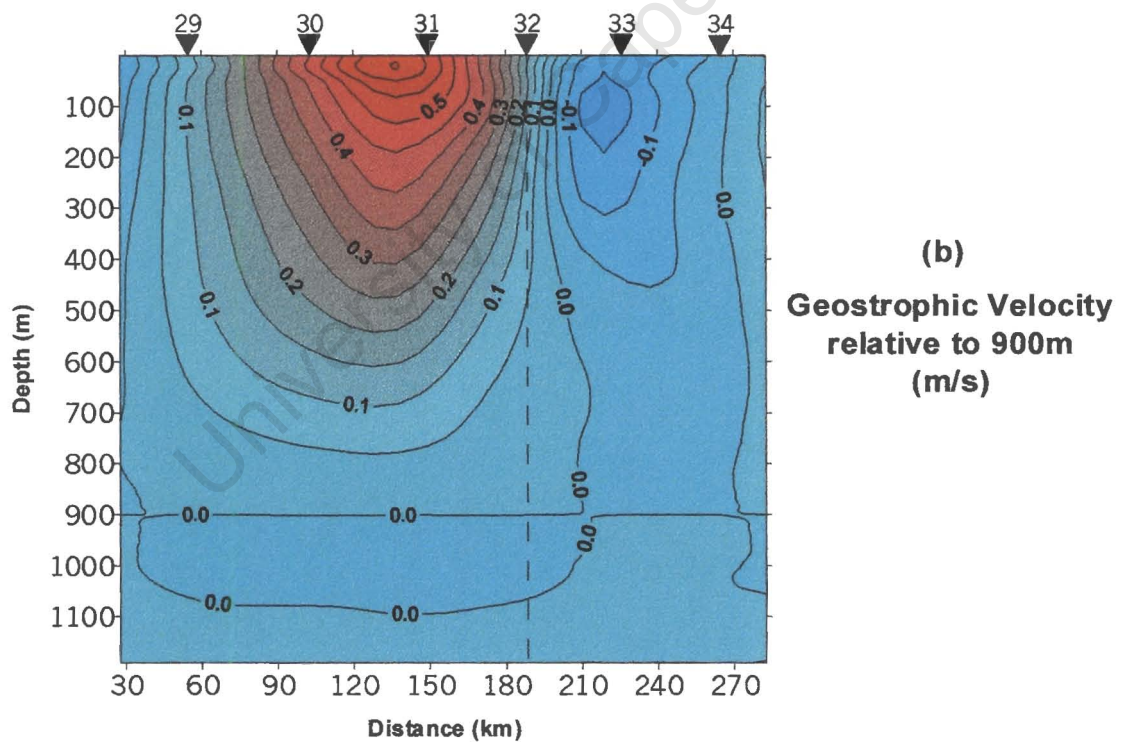
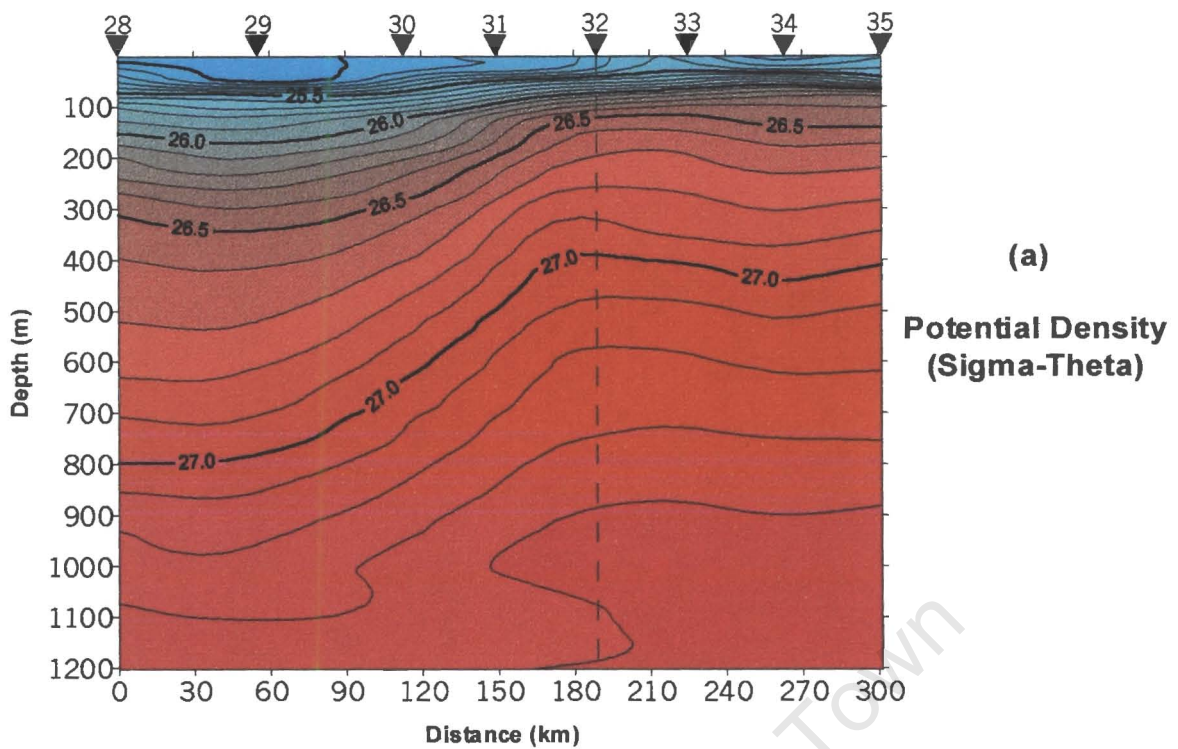


Figure 5.15: Vertical potential density (a) and geostrophic velocity (b) sections derived from XBT and CTD measurements taken from FRS Africana in December 1996.

Scaling Parameters for anticyclonic ring

In order to provide a baseline for the inter-comparison of the ring sampled during December 1996 with previously sampled Agulhas rings, it is useful to introduce a number of different scales. These scaling parameters are the Rossby number, the Burger number and the Richardson number (*Olson, 1991*). A simple two-layer description of the density variation with depth allows for the calculation of the scaling parameters (see *Appendix I*). Various quantities were determined to make this calculation possible. The maximum radial velocity (V) for the anticyclonic ring was calculated as 1.0 m/s between CTD 19 and CTD 20. Using the ring characteristics established from section 2, the length scale at the radius of maximum velocity (L) could be estimated at 102 km, the depth of the 10° C isotherm (h) is 672 m and the depression of the 10° C isotherm (δh) is 272 m. The reduced gravity for the two-layer model (g') calculated from the regression of the dynamic height vs the isotherm depth was 0.0106 with a r^2 of 0.9657. These values allowed for the calculation of the following ring scaling parameters:

Rossby number (R_o)	-0.042
Rossby radius (R_d)	32.1 km
Displacement Burger number (B')	-0.040
Burger number (B)	0.099
Richardson number (R_i)	7.12

Discussion

Information retrieved from the hydrographic data supports the findings gleaned from the AVHRR imagery of 19 and 20 December 1996. The transect grid allowed for hydrographic coverage of the anticyclonic eddy and the cyclonic eddy, as well as the filament being drawn between them. The plume exuding between the eddy pair and the northward moving shelf edge arm of the filament was also surveyed.

At the 500 m depth level, the horizontal temperature section (*Figure 5.6*) of the data agreed well with the picture of an eddy pair portrayed by the AVHRR data of 20 December 1996 (*Figure 5.3*). This section illustrates the strength of the dipole feature by virtue of the significant distortion of the temperature field at this depth level. The

significance of the dipole is further illustrated by its effect on the elevation of the $27 \text{ kg/m}^3 \sigma_\theta$ (Figure 5.7), with a peak representing the cyclonic eddy and a strong depression representing the anticyclonic eddy. It is also evident from the AVHRR data represented in Figure 5.1 and Figure 5.3 that the approximate centres of the respective rings observed on these images are corroborated by the *in situ* data. Thus, the dipole signature identified from the surface tracer, i.e. sea surface temperature (AVHRR), provides a very accurate representation of the surface expression of the features present throughout the surveyed water column. The cruise-track overlay on Figure 1.2 indicates that both eddies, as well as the filament, were sampled during the cruise and the presence of these features were all recognised during the analysis of the *in situ* data. The warmer surface water of the anticyclonic eddy is clearly identifiable as a $>20^\circ \text{ C}$ well mixed surface layer in all the sections, but the 18° C surface temperature water observed in the centre of the cyclonic ring is conspicuously absent. This could be because the cyclone was only partially sampled. There is, however, evidence of the warm filament, exhibiting $>20^\circ \text{ C}$ water east of CTD 13 (Figure 5.8 (a)), between CTD 21 and 22 (Figure 5.10(a)) and between CTD 34 and 35 (Figure 5.14(a)), having been sampled. Cooler water (19° C to 20° C) of Atlantic origin (Figure 5.3) was identified between the anticyclonic eddy and the warm filament at CTD 25 (Figure 5.12(a)) and between CTD 20 and CTD 21 (Figure 5.10(a)).

The vertical sections also illustrate, in agreement with the horizontal sections, the deformation of water column property iso-surfaces due to the presence of the translating dipole. Geostrophic velocities calculated for the various transects indicate the presence of strong anticyclonic flow as well as weaker cyclonic flow. These sections also provide more clues about the origin of the respective eddies in this dipole. A salinity maximum layer of 35.6 psu is observed in all the sections in the 100 m to 200 m depth level inside the anticyclonic ring. At the Agulhas retroflection, water with a temperature above 16° C is isohaline at 35.6 psu (Camp *et al.*, 1986; Valentine *et al.*, 1988). The surveyed anticyclonic eddy exhibited two isohaline layers: one of 35.5 psu in the near surface layer with temperature greater than 18° C and another of 35.6 psu with temperatures ranging from 16° C to 17° C . Subtropical Surface Water (>35.5 psu) is recognised by the subsurface salinity maximum it exhibits throughout the South Indian Ocean and this water is transported by the Agulhas Current into the retroflection region (Valentine *et al.*, 1993). It is notable in Figure 5.16 that the anticyclonic eddy core does share properties

with the Agulhas retroflection and this supports the assumption that it is an Agulhas ring. Ring scaling parameters calculated for the anticyclonic eddy supports the assumption that the surveyed ring is of Agulhas retroflection region origin. The ring parameters resulting from this investigation fall in the expected range of ring scaling parameters calculated for various Agulhas rings by *Duncombe Rae (1994)*. The Rossby number for the anticyclonic eddy show that, despite the anomalous “D-shape” of the ring, non-linear advective terms can be ignored and the assumptions allowing the use of the two-layer model are valid. *Olson et al. (1985)* showed that the radius to maximum velocity (L) approaches the radius of deformation (R_d) scale as the ring decays. This ratio is small (0.31) indicating that the ring was spawned recently (at the Retroflection region).

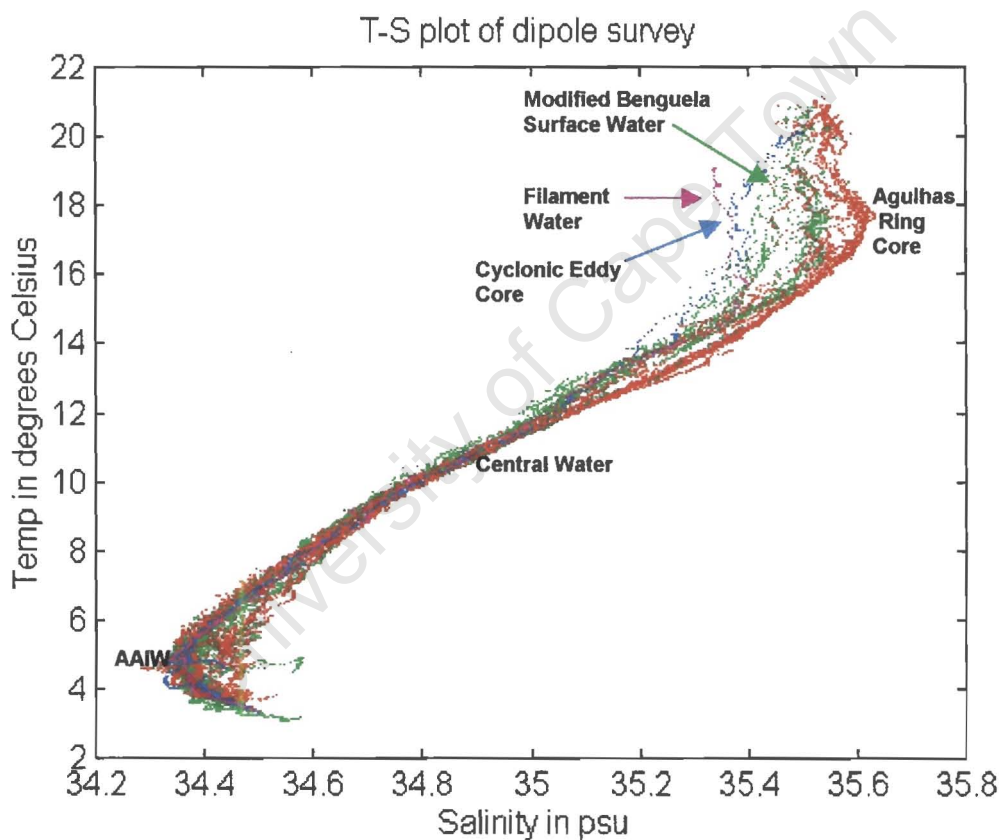


Figure 5.16: Temperature-salinity (T-S) diagram for CTD stations representative of the dipole and filament structure.

Figure 5.16 illustrates the different properties associated with the water masses, which characterise the different oceanic features identified on the sea surface temperature images in Figure 5.1 and Figure 5.3. The stations representing the various features were identified from the satellite imagery and assigned distinctive colours on the T-S curve. Red represents the anticyclone (CTD 15 to 18 and CTD 26 to 30), blue the cyclone (CTD

21 and 32), magenta the filament (CTD 35) and green the South Atlantic water (CTD 12 to 14, 19, 20, 22 to 25, 31, 33 and 34). There are a number of water masses present off the west and south coasts of Southern Africa, including tropical and subtropical surface waters, thermocline waters (comprising South Atlantic Central Water, South Indian Central Water, tropical Atlantic Central Water), Antarctic Intermediate Water, North Atlantic Deep Water and Antarctic Bottom Water (*Shannon and Nelson, 1996*). Four water masses can be identified on *Figure 5.16*:

- * Antarctic Intermediate Water (AAIW) with a temperature range of 4-5° C and a salinity range of 34.32–34.43 psu.
- * Lower Central Water (LCW) with a temperature range of 6-12° C and a salinity range of 34.44-35.04 psu.
- * Upper Central Water (UCW) comprising two discrete T-S curves with a temperature range of 12-16° C and salinity values ranging from 35.04-35.39 psu and 35.04-35.53 psu respectively.
- * Surface Water (SW) which have temperature values >16° C and salinity values ranging from 35.37-35.6 psu.

In the core of the anticyclone AAIW is found at approximately 1025 m, which is close to the depth of 1100 m at which AAIW is found in the Agulhas retroflection region (*Shannon and Nelson, 1996*). The AAIW identified in the cyclone and other water, sampled in close proximity to the two eddies, is found at a depth of approximately 800m. According to *Shannon and Nelson (1996)*, AAIW is present at this depth in the South-east Atlantic Ocean. Indian Ocean AAIW (Agulhas Current origin) has a salinity value >34.45 psu (*Shannon and Hunter, 1988*) and South-east Atlantic Ocean AAIW (Benguela Current) has salinity values ranging from 34.2-34.5 psu. Overall the AAIW indicated in *Figure 5.16* falls within these salinity ranges and could thus represent the sampling of AAIW of Benguela Current origin, as well as AAIW of Agulhas retroflection origin.

The LCW identified in *Figure 5.16* agrees well with the expected values for the South-east Atlantic described by *Shannon and Nelson (1996)*. However, the authors also explain that it is extremely difficult to distinguish between central waters with a temperature range of 10-12° C, found in the South-east Atlantic Ocean and those originating from the Indian Ocean. Indian Ocean Central Water is advected into the South-east Atlantic Ocean in modified form by Agulhas rings and filaments. Two

separate curves can be identified in the UCW. It is clear that the curve indicating more saline water represents the anticyclone, whereas the curve indicating fresher water represents a combination of CTD stations incorporating the filament, the cyclone, South-east Atlantic Ocean water and some of the anticyclone CTD stations. The UCW identified in the anticyclone has the characteristics of South Indian Central Water that has a temperature range of 8-15° C and salinity values ranging from 34.6-35.5 psu (*Gordon et al., 1987*). South Atlantic Central water has a temperature range of 6-16° C and salinity values ranging from 34.5-35.5 psu (*Valentine et al., 1993*). These values agree well with the UCW identified in the waters sampled outside the anticyclone core.

The SW (upper mixed layer) represented in *Figure 5.16* clearly illustrates the different mixed layer characteristics of the anticyclone, the cyclone and the filament. Warmer and more saline T-S characteristics signify the presence of the anticyclonic eddy. In contrast, the surface waters of the cyclonic eddy are significantly cooler and fresher. Salinity values ≥ 35.4 psu are found with temperatures above 17° C, suggesting that the surface water of the cyclone is of Benguela Current water origin (see *Figure 14* of *Shannon and Nelson, 1996*). Considering the rotation of the cyclonic eddy about the Agulhas ring, it is possible to surmise that this eddy was not completely sampled hydrographically. It is clear from the sea surface temperature image of 20 December 1996 that CTD 21 could only sample the edge of the cyclonic eddy. Although CTD 32 appears to sample the centre of the cyclonic eddy, this centre would have shifted at least 0.3° of longitude by the time the data was collected. These deductions would also explain why the 18° C water marking the central surface water of the eddy was not observed in the temperature sections. Between the T-S curves representing the Agulhas ring core and the cyclonic eddy core the spread of salinity characteristics represent modified Benguela surface water, which could be a result of mixing between surface waters of Agulhas Bank origin (via the filament) and Benguela surface water.

Even lower near surface salinity values, ranging from 35.35 psu to 35.4 psu, are seen at CTD 35, marking the eastern edge of the shelf edge component of the filament. *Figure 5.14(a)* clearly represents the position of CTD 35 with respect to the northward arm of the filament from an *in situ* point of view. In the gradient image of 20 December 1996 (*Figure 5.4*) the eastern edge of the northward component of the warm filament is

delineated by a temperature front in association with an upwelling filament. The time delay between the image and the actual sampling could indicate that Benguela upwelling frontal water was at least partially sampled at CTD 35, or that there was some mixing of Benguela upwelling frontal water with the borders of the filament. Upwelling filaments extending from the Cape Peninsula and Cape Columbine form strong sea surface fronts adjacent to the warm filament. These fronts represent regions of shear where entrainment of old upwelled surface water into the borders of the warm filament could occur. Furthermore the isobaths on *Figure 5.3* indicate that the measurements were recorded in close proximity to the West Coast shelf edge. According to *Shannon and Nelson (1996)* water mass properties of approximately 6° C, 34.5 psu to 16° C, 35.5 psu are indicative of the water mass that upwells along the coast and constitutes, often in highly modified form, the shelf waters of the Benguela Current. Old upwelled water is sun-warmed and could thus be fresher than non-upwelled water of the same temperature. The salinity values measured in the near surface layer at CTD 35 approximate values expected of Benguela shelf water.

The hydrographic survey conducted by the FRS *Africana* in December 1996 thus revealed the following:

- An Agulhas ring forming a dipole vortex with an adjacent cyclonic eddy was surveyed in the South-east Atlantic Ocean.
- Water in the cyclonic eddy has T-S characteristics of South-east Atlantic thermocline and surface water.
- A warm filament is being drawn westwards between the two eddies and result in a pool of warm water to the north-west of the dipole vortex.
- There is a northward component of the filament water present on the West Coast shelf edge forced by the shelf-edge jet (*Shannon and Nelson, 1996*).
- Cooler Atlantic water is drawn (from the south) between the filament and the Agulhas ring causing a temperature front in the near surface mixed layer.

Agulhas rings have not commonly been described as vortex dipoles in literature to date. Naturally this leads one to wonder about the origins of the particular dipole described in this chapter. In Chapter 6 further analyses of satellite data, representing the south-east Atlantic Ocean in the three-week period preceding the cruise, will be undertaken so that an understanding of the genesis and evolution of this eddy pair can be gained.

Chapter 6

Origin of the Dipole Vortex

Even though the presence of a dipole vortex in the Southeast Atlantic, during mid-December 1996, has been established, its origin needs to be established. In Chapter 5 strong evidence was found supporting the assumption that the primary vortex in the dipole originates from the Agulhas Current. Evidence in Chapter 5 also indicates that the secondary vortex contains Benguela Current water and was thus formed away from the retroflection region. These assumptions fail to address the processes involved in initiating the dipole circulation and leads one to ask:

What circumstances conspired to result in the presence of a dipole vortex, comprised of an Agulhas ring and a cyclone containing Benguela Current water, in the South-east Atlantic Ocean?

This chapter will answer this question from the results of an investigation of satellite imagery pre-dating the cruise. AVHRR data and altimeter data are used to trace the translation of the dipole from its origin. The AVHRR images are treated as the primary source of information for the analysis of the history of the dipole. Altimetry data is then used to corroborate deductions made from the infrared images.

Analysis of AVHRR Data

Cloud cover in the South-east Atlantic region interferes with the tracking of the sea surface temperature as a tracer of ring shedding processes at the Agulhas retroflection region. Consequently only days representing the maximum amount of interpretable sea surface data were chosen for “back-tracking” the dipole to its origin. All the SST data, except *Figure 6.1*, was represented in the same way as in Chapter 5. A different palette is used in *Figure 6.1* and the represented data has a lower resolution (9 km GAC data). The rest of the data are represented as false-colour images with an approximated “Zebra palette”. Six days representing quality data are analysed and the anticyclonic ring is easily traced back to the Agulhas retroflection region where it originated at the beginning

of December 1996. The progress of the dipole feature and its influence on the surrounding environment could be followed on AVHRR data representing 4, 5, 7, 9, 10, 13, 19 and 20 December 1996. However, data representing 19 and 20 December 1996 has already been analysed in Chapter 5 and only relevant AVHRR data preceding these dates are analysed in this chapter.

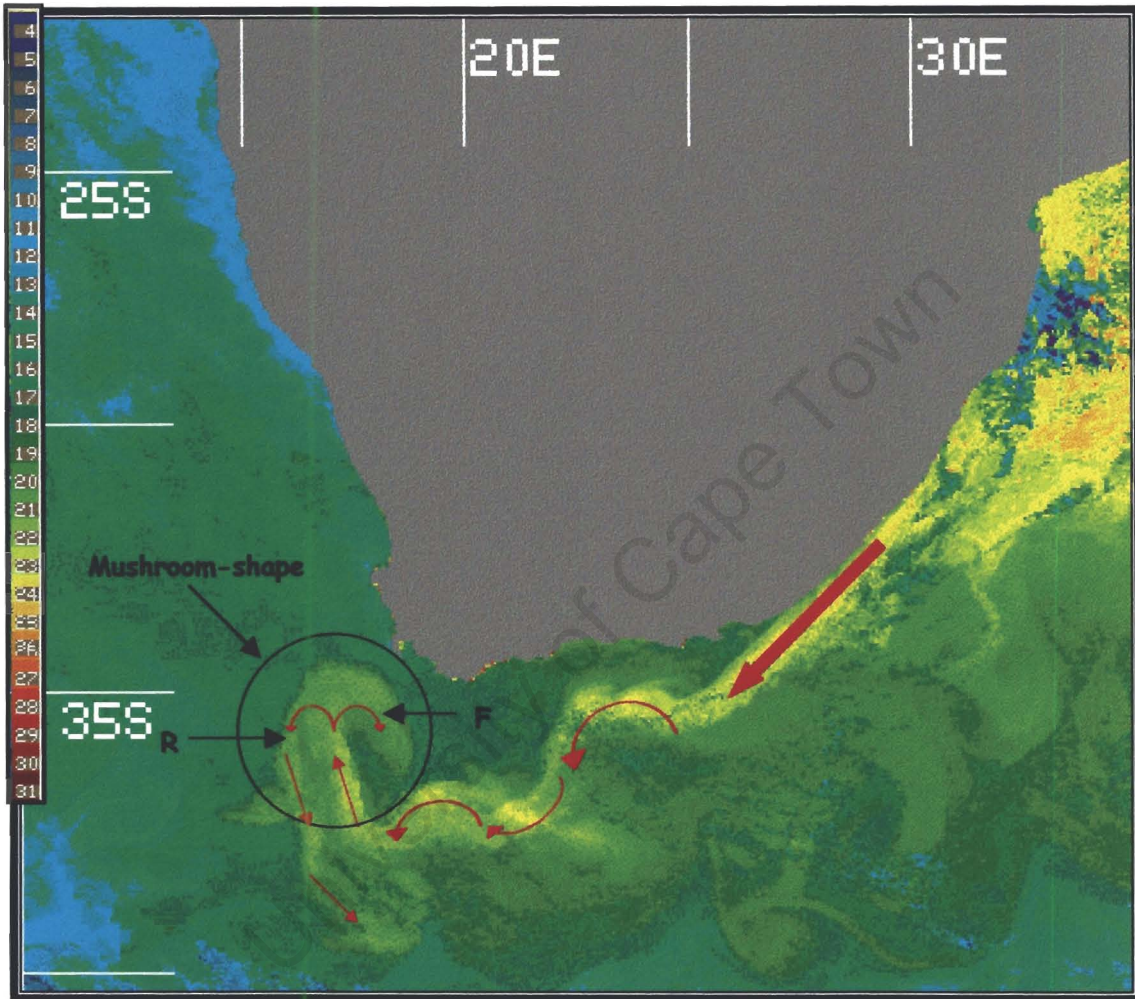


Figure 6.1: *AVHRR Sea Surface Temperature Image for 5 December 1996. Flow representing the Agulhas Current is marked in red arrows. (GAC data from RSMAS at Miami University)*

At the time of production, the southern limit of available AVHRR data processed at UCT could only be extended to 37°S. Important information concerning the initiation stages of the Agulhas ring is thus not represented in this data and another source of data was required for representing an overall picture of the region during the early stages of this

dipole's development. Dr Chris Duncombe-Rae of the Cape Town-based Sea Fisheries Research Institute (now Directorate of Marine and Coastal Management) provided an SST image (*Figure 6.1*), obtained from the University of Miami Rosenstiel School of Marine and Atmospheric Science (RSMAS), in which the whole Agulhas Current is visible as it meanders and retroflects south of Africa. The image is part of the AVHRR Pathfinder Oceans dataset.

Various features on *Figure 6.1* have been highlighted in order to help sketch the scenario relevant to this investigation as seen on 5 December 1996. The upper reaches of the Agulhas Current can be identified as the strip of 23° to 24° C water following the East coast of South Africa very closely (thick red arrow in *Figure 6.1*). As it left the East coast and followed the eastern Agulhas Bank, the current meandered several times before it retroflected at about 16° E (thin curved red arrows). The retroflexion region formed part of a large meander in the current and some interesting flow patterns can be discerned on the image. As the Agulhas reached 17° E it turned sharply and flowed northward for about 2.5° of latitude before turning back upon itself. A division in the flow of the Agulhas Current can be identified at 35.5° S as part of the current continued anticyclonically along the expected route, forming the Agulhas retroflexion (marked **R**). To the east of the meander a filament of warm water (21°-22° C, marked **F**) moved away from the main current in a large cyclonic turn. Together these features constituted a mushroom-type formation with the main current forming the 'mushroom-stem' and the cyclonic and anticyclonic branches of the current forming the 'mushroom-cap'. The Agulhas Return Current can be observed flowing eastward at approximately 39° S. In this region the temperature signal identifying the ribbon of Agulhas Current water is less distinctive, but the southern boundary of the Return Current is delineated by a temperature front meandering between 38° and 40° S.

Now that an overall picture of the behaviour of the Agulhas Current in early December 1996 has been described, it is important to zoom in and do a detailed description of the progression of the relevant features that ultimately result in the dipole vortex identified on 19 December 1996. The images that follow start with a closer look at the mushroom formation identified in *Figure 6.1* and are then used to track the progression of flow patterns to the distinction of a clear dipole vortex on 13 December 1996.

4 December 1996

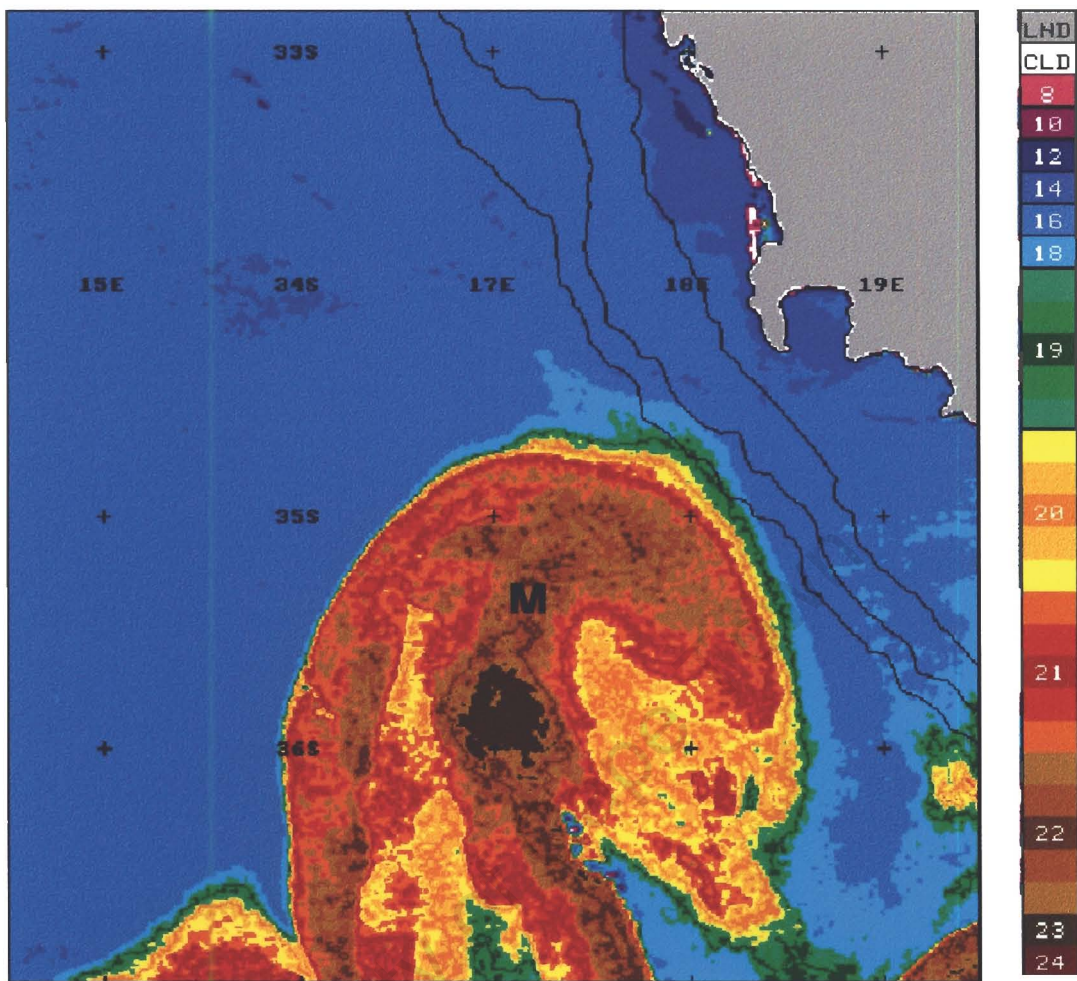


Figure 6.2: AVHRR Sea Surface Temperature Image on 4 December 1996.

Although *Figure 6.1* represents AVHRR data sampled on 5 December 1996, it was possible to produce good high-resolution AVHRR data from 4 December 1996 onwards. This allowed for better continuity in tracking features from one day to the next. A mushroom-shaped flow pattern is identifiable on *Figure 6.2* and it has already been ascertained from *Figure 6.1* that this feature forms the northern part of an Agulhas retroflection loop. The northern part of the feature shows a spread of warm water in both an easterly and westerly direction, and the 21° C and 22° C water indicate that the flow turns back towards the south, forming a ‘mushroom’-like structure (marked **M**). The western arm of this mushroom structure extends beyond the boundaries of this image and has been identified as part of the retroflection loop in *Figure 6.1*. Anticyclonic flow can thus be identified on the western side of the mushroom structure, with the indication of cyclonic flow on the eastern side of the mushroom structure. The elliptical shape and the

annulus-type water distribution of the sea surface temperature, representing the anticyclonic structure, are characteristic of an Agulhas ring in its early formative stages.

5 December 1996

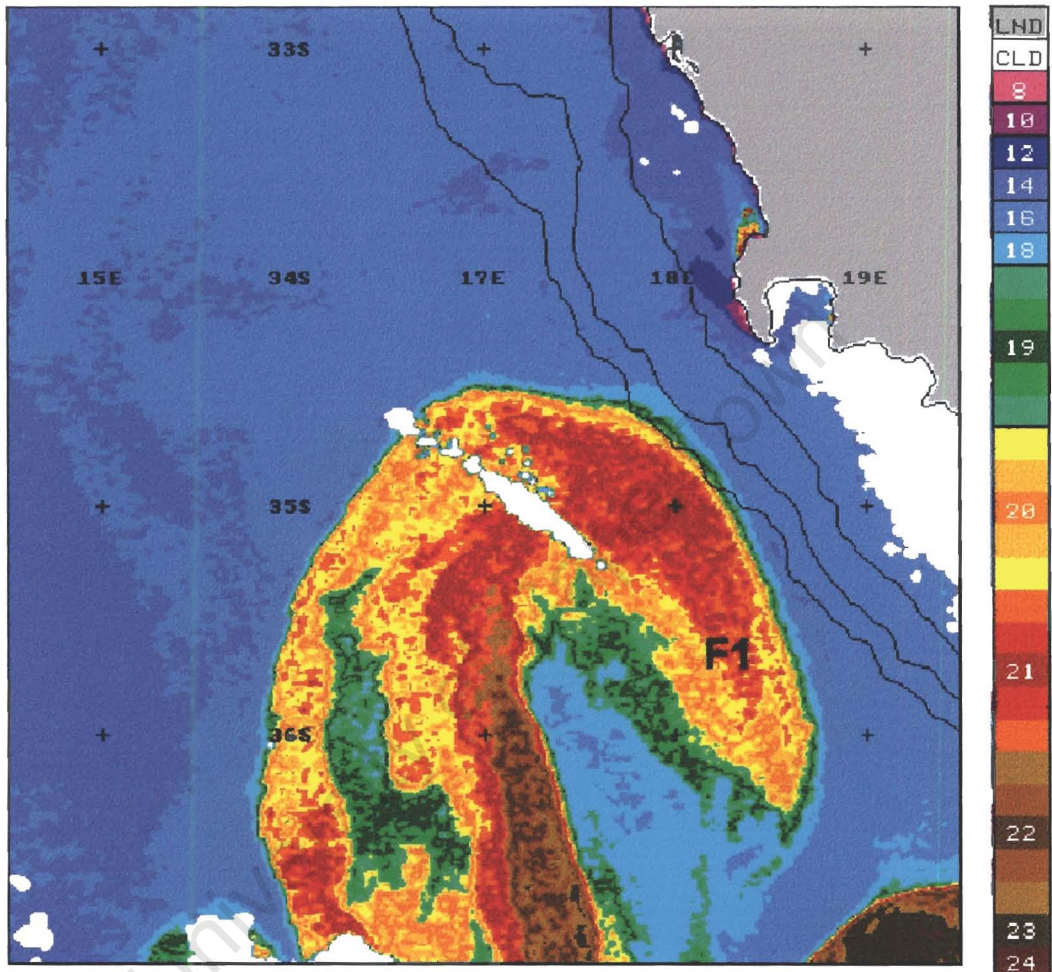


Figure 6.3: AVHRR Sea Surface Temperature Image on 5 December 1996.

In *Figure 6.3* the northern most extent of the ‘mushroom cap’ has shown some northward displacement since the previous day. The feature on the eastern side of the ‘mushroom stem’ exhibits a cyclonic rotation delineated by a broad warm filament (F1) extending from the ‘mushroom cap’. This filament curls back along the Agulhas Bank edge and then heads southward. Although some surface cooling of the phenomenon is evident, especially around the anticyclonic feature, a very clear cyclonic turn is evident from the 21° C water. The area of cooler water in the centre of the anticyclonic feature is larger than before and a minimum temperature of 18° C is observed in the centre. Despite the

change in the temperature signature of the anticyclonic feature, the thermal structure does not reveal any significant spatial displacement of the feature.

7 December 1996

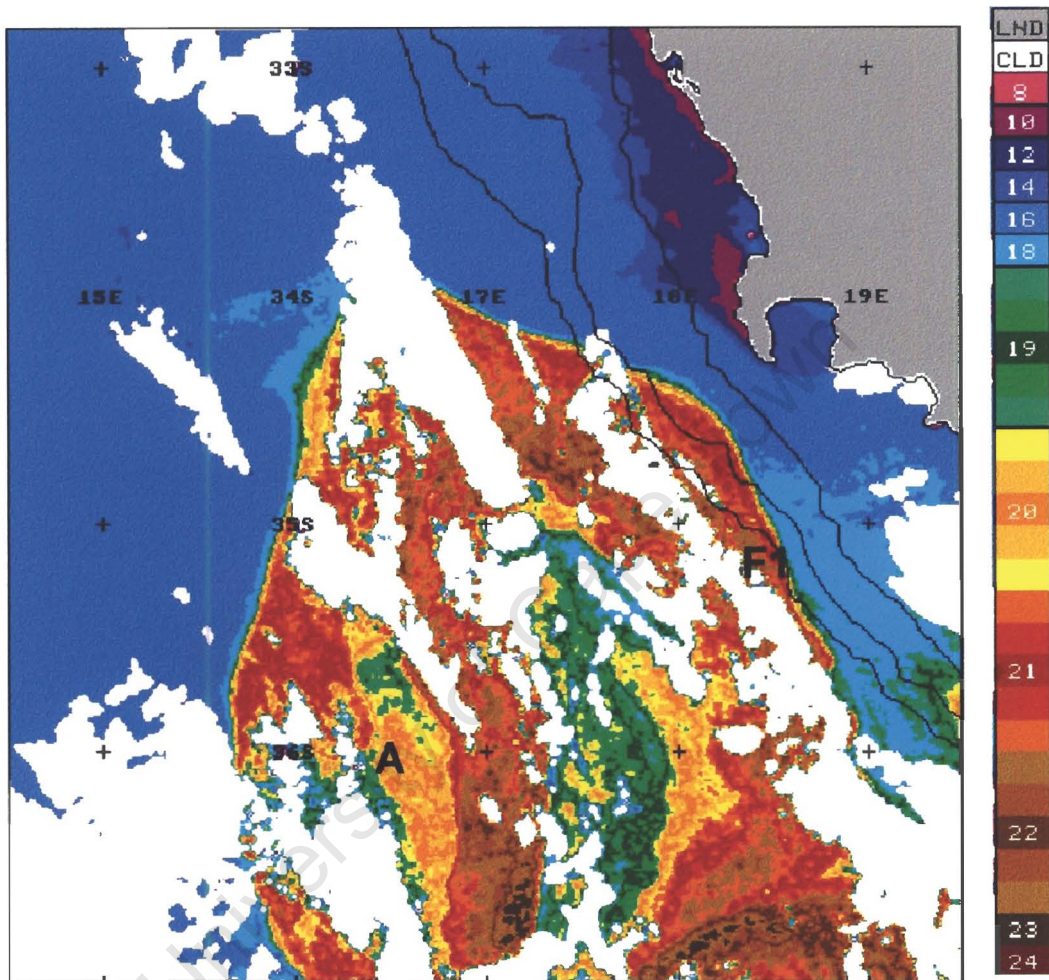


Figure 6.4: *AVHRR Sea Surface Temperature Image on 7 December 1996.*

Cloud cover obscures much of the image on 7 December 1996 (*Figure 6.4*), but the remaining data is adequate for identifying structure and flow characteristics relevant to this investigation. The boundary of the warm Agulhas surface water now extends further north and the ‘mushroom cap’ has collapsed giving the whole warm feature an elongated appearance. An annulus-shaped anticyclonic structure (A) is recognisable on the image, but it is still unclear from this image whether an Agulhas ring has occluded or not. Warmer surface temperatures are evident in the anticyclonic feature and this suggests that the feature has intensified. The eastern arm of the collapsed ‘mushroom-cap’ has become

broader, indicating that a higher volume of Agulhas water is being incorporated within structure A. Warm Agulhas water (22°C to 23°C) is drawn along the ‘stem’ of the ‘mushroom’ and cools as it flows back southwards in the form of filament F1. This is clear when one observes the cooler water in filament F1 joining the warmer waters of the eastward flowing Agulhas Current. The strength of the cyclonic feature is evident from the sheer size and extent of the filament trailing from the collapsed ‘mushroom cap’. A body of cooler water (18°C to 19°C) is still apparent between the ring and the filament.

9 December 1996

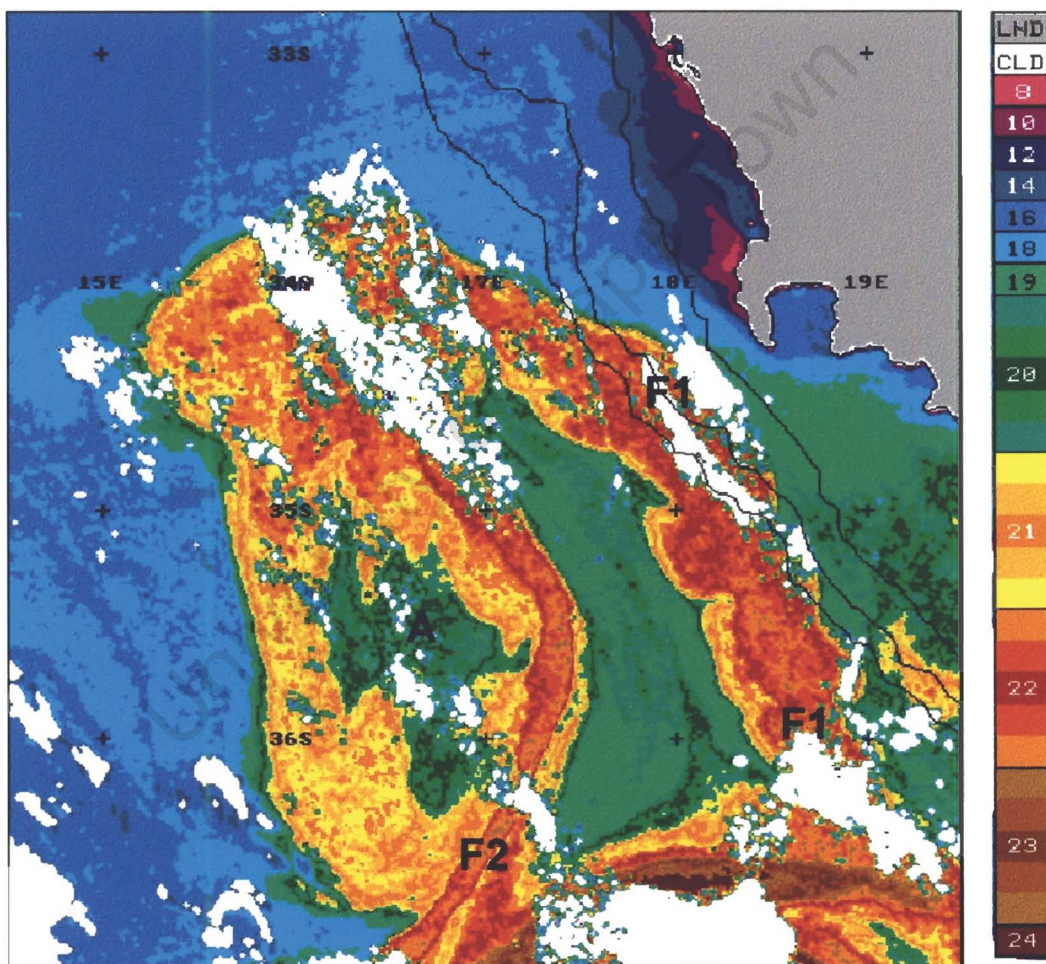


Figure 6.5: AVHRR Sea Surface Temperature Image on 9 December 1996.

On 9 December 1996 (Figure 6.5) the anticyclonic feature A is still connected to the Agulhas Current via a filament labelled F2. Warm water is drawn directly from the retroflection region, via F2, and collects in the northern part of feature A, previously

referred to as the collapsed ‘mushroom-cap’. It is clear from the surface signature that this part of feature A has expanded considerably and shows increasing northward and westward spread. The warm filament (F1) identified on earlier images is unmistakably observed extending eastward from the bulbous part of the Agulhas ring and following the edge of the Agulhas Bank to the retroflexion region. There is no clear indication of cyclonic flow east of the Agulhas ring, other than, perhaps, the persistence and continual warm surface signature of filament F1. A considerable region of cooler water (19° to 20° C) separates the two filaments F1 and F2.

10 December 1996

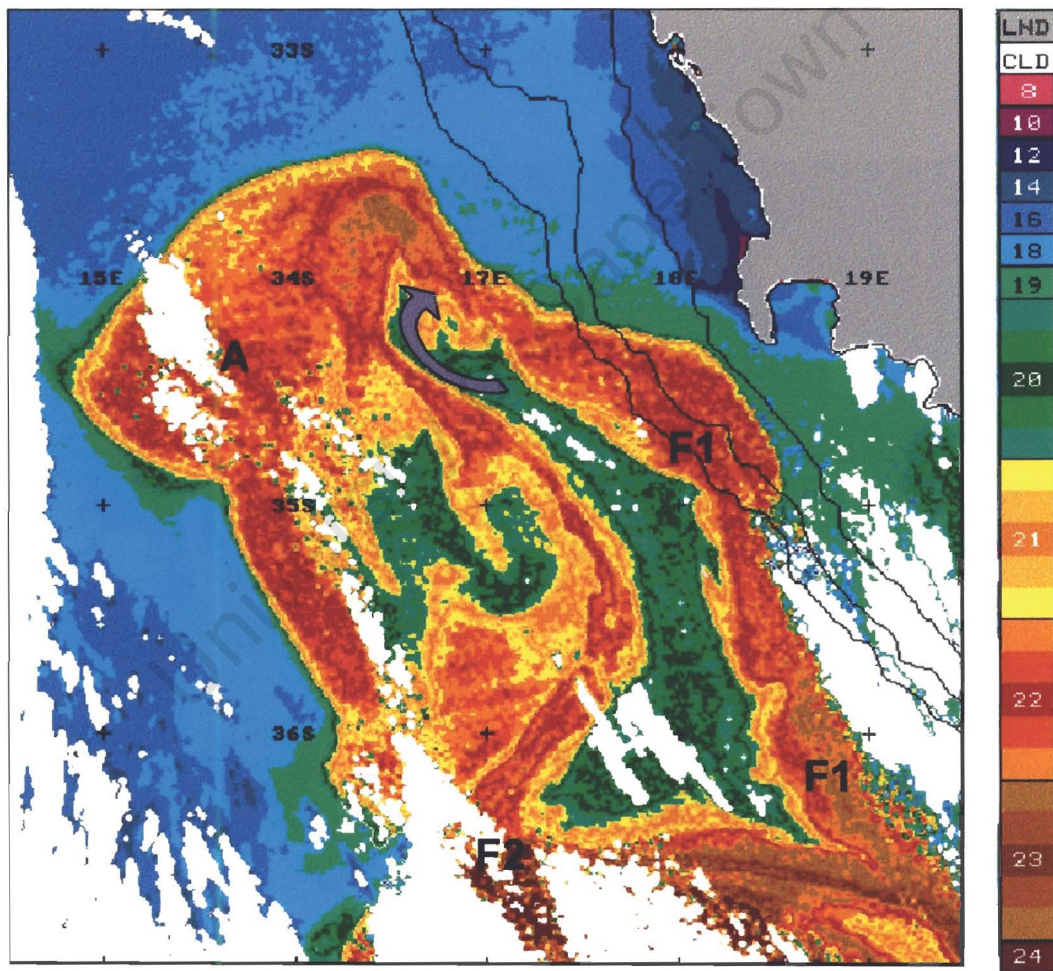


Figure 6.6: AVHRR Sea Surface Temperature Image on 10 December 1996.

In *Figure 6.6* the ‘bulbous’ region is bigger than before and reaches further west and north, assuming a more familiar eddy-like shape. This region also retains the greatest

amount of Agulhas Current water and is marked **A**, as it now represents the most intense component of the Agulhas ring. There is still an annulus-shaped appendage that trails the principal region of the ring. This feature could represent a weaker part of the general anticyclonic circulation associated with the Agulhas ring, with filament **F2** forming the eastern part of this circulation, and a trailing warm filament in the wake of the Agulhas ring forming the western part. The complicated circulation patterns observed in *Figure 6.6*, are probably indicative of some intermediate stage of Agulhas ring separation from the retroflection region. Filament **F2** is moving ever closer to filament **F1** and the cooler water separating them is being drawn into a cool filament that exhibits cyclonic curl at approximately $16.6^{\circ}\text{E}/34.4^{\circ}\text{S}$ (see grey arrow in *Figure 6.6*). At this stage it is not possible to establish unambiguously the preferred direction of flow of filament **F1**.

13 December 1996

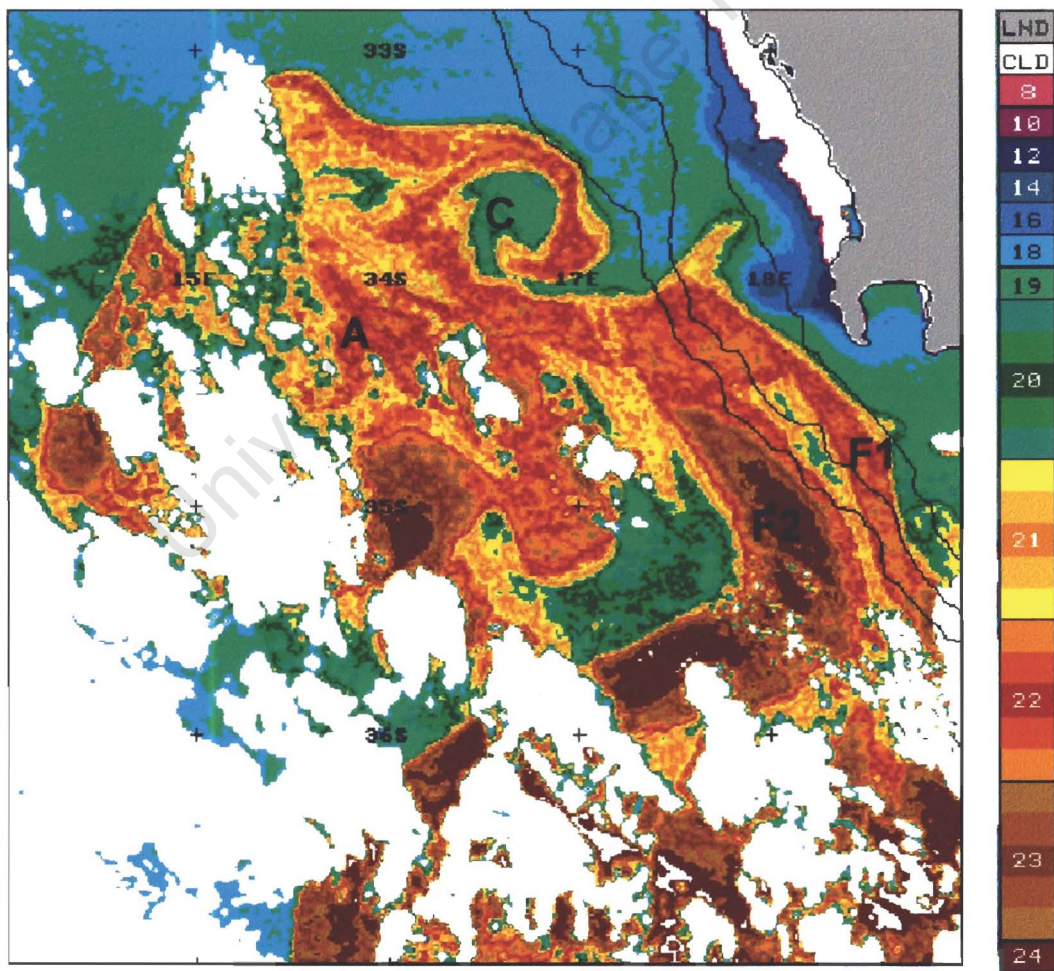


Figure 6.7: AVHRR Sea Surface Temperature Image on 13 December 1996.

The extensive cloud cover in *Figure 6.7* obscures large areas of the features identified in the region thus far. The process of declouding, i.e. assigning one value to pixels representing cloud cover, also proved to be problematic and some ‘cloud ringing’, i.e. uncharacteristic cold areas surrounding patches of cloud over warm water, does occur. However, the Agulhas ring (**A**) can be partially identified and both filaments are clearly identifiable. **F1** is now narrower than **F2** and the filaments coalesce before they are drawn around the Agulhas ring. The orientation of this unified filament becomes closer to an east-west orientation. North of where the filament joins the Agulhas ring a cyclonic feature (**C**) is recognisable as it is delineated by a filament curling cyclonically around a cooler body of water. A dipole is thus formed just east of Cape Town by the Agulhas ring and a newly developed cyclonic eddy.

At this stage the information gleaned from the AVHRR imagery analysis indicates that an Agulhas ring occluded from an extreme northward meander of the retroflexion region and subsequently developed into a dipole. The dipole development was preceded by a complicated continual interaction of the developing Agulhas ring and the retroflexion region. This process does deserve further discussion, but at this point in the investigation it is necessary to corroborate the interpretation of the AVHRR imagery from altimeter data.

Analysis of Altimetry Data

Gründlingh (1995) used TOPEX/POSEIDON data in conjunction with NOAA-11 AVHRR data to investigate the characteristics of eddies and rings in the oceans around southern Africa. It was concluded from that investigation that there is good agreement between the topographic and infrared portrayals of rings, even in the dynamic environment of the retroflexion region. Based on this premise, it is reasonable to expect good agreement between the altimetry and the AVHRR imagery despite the difference in resolution of data representation (1.1 km^2 for AVHRR vs. 0.25° for altimetry). Seven sea surface height anomaly images, which were produced from geophysical data records and represent the best available TOPEX/ERS-blend on that day, were downloaded from the CCAR Altimetry archive website. The following dates are represented in the altimetry imagery: 2, 5, 8, 11, 14, 17 and 20 December 1996.

It is important to consider whether the information seen in *Figure 6.8* is a good representation of the sea surface height anomaly (SHA) because it is a blend of the most recent 10 days of TOPEX/POSEIDON and most recent 35 days of ERS-2 sampling. The accuracy of the data and quality of interpolation will thus depend on the most recent overpasses of the satellites. In order to validate the relevance of the altimetry images to this investigation, an altimetry image representing good recent coverage by both satellites is chosen to compare to an AVHRR image of around the same time. The overpass times and cycles for the two satellites during December 1996 are included in *Appendix II*.

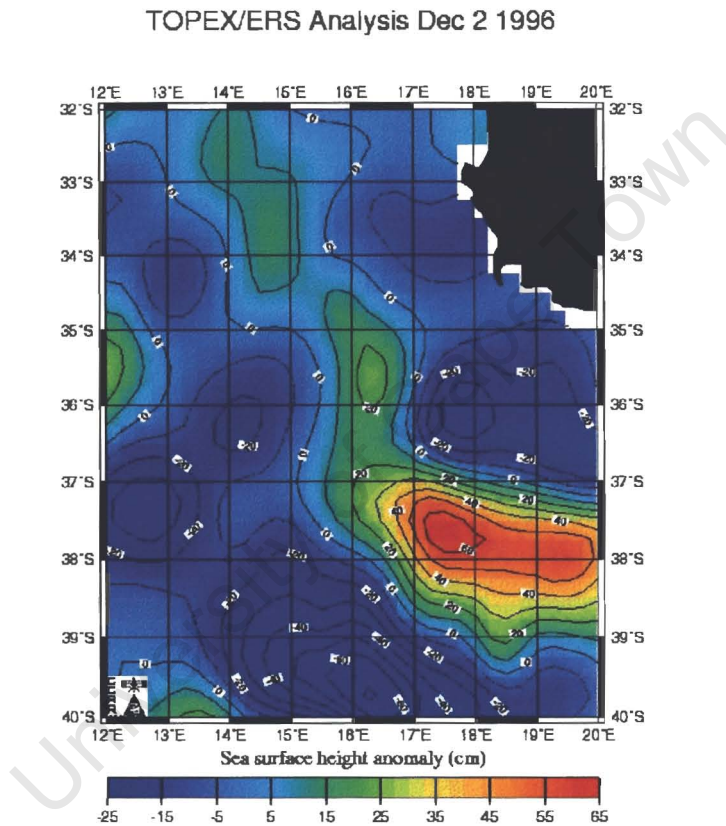


Figure 6.8: *Sea surface height anomaly (SHA) for the southeast Atlantic region on 2 December 1996.*

Mesoscale features can be identified from altimeter-derived data as deviations from the mean sea surface height (SHA) and anticyclonic warm rings can usually be detected as positive alongtrack values of SHA (*Goni et al., 1997*). Conversely cyclonic rings can be detected as negative alongtrack values of SHA. In *Figure 6.8* the large positive region located at approximately $17.5^{\circ} \text{ E} / 37.7^{\circ} \text{ S}$, together with a lobe of positive SHA values budding in a northward direction from it, represents the retroflection region as it was

identified in AVHRR images of early December 1996. This representation compares especially well with *Figure 6.1* and *Figure 6.2*. Furthermore, there is an elevated elliptical region within the northward protrusion suggesting the initiation of an Agulhas ring occluding from the retroflexion region. A cyclonic feature located at $17.9^{\circ}\text{E} / 36.1^{\circ}\text{S}$ is also identifiable east of the northward protruding retroflexion region. The fact that these observations agree well with the oceanographic regime observed on SST imagery in early December 1996 promotes the claim that altimetry can provide an accurate interpretation of features surrounding the Agulhas retroflexion region. However, one should bear in mind that the accuracy of the altimetry interpretation depends upon the most recent overpasses made by both the TOPEX/POSEIDON and ERS-2 satellites.

Now that the agreement between observations made in the SST imagery and the altimetry imagery has been established, it should be possible to follow the development of the dipole in *Figure 6.9*. This figure consists of a sequence of selected altimetry imagery representing the SHA in the south-east Atlantic during the first three weeks of December 1996. The three-day gap between images is due to the method employed by the CCAR for producing near-real-time altimetry images. In the first image (*Figure 6.9(a)*) there is an apparent intensification of the cyclonic feature described earlier, but no spatial variation is evident since the previous image. There is a significant change in the lobe of elevation extending from the retroflexion region. It extends further north and the region of maximum elevation has been displaced to $15.8^{\circ}\text{E}/34.8^{\circ}\text{S}$. Much of the rest of the information on the image is very similar to that represented on 2 December 1996. It is disconcerting to notice that there are some striking inconsistencies between the altimetry image of 5 December 1996 and the AVHRR image of the same date. The position of the developing ring represented by a region of elevation at $15.8^{\circ}\text{E}/34.8^{\circ}\text{S}$ does not compare well with the developing mushroom shape on the AVHRR image. This altimetry image is an example of poor SHA representation and should be regarded with scepticism because there was very poor coverage of the relevant region of interest in the south-east Atlantic Ocean by the recent overpasses of the respective satellites. An examination of the overpass information presented in *Appendix II* reveals that the most recent overpass of the TOPEX/POSEIDON was 133 and that of ERS-2 was 214. Both overpasses do not cover the region of interest and the image produced from this data was more subject to interpolation errors. Since good images are produced from Interim GDR's every three days (see Chapter 4), poor coverage by the satellite overpasses in the three day period

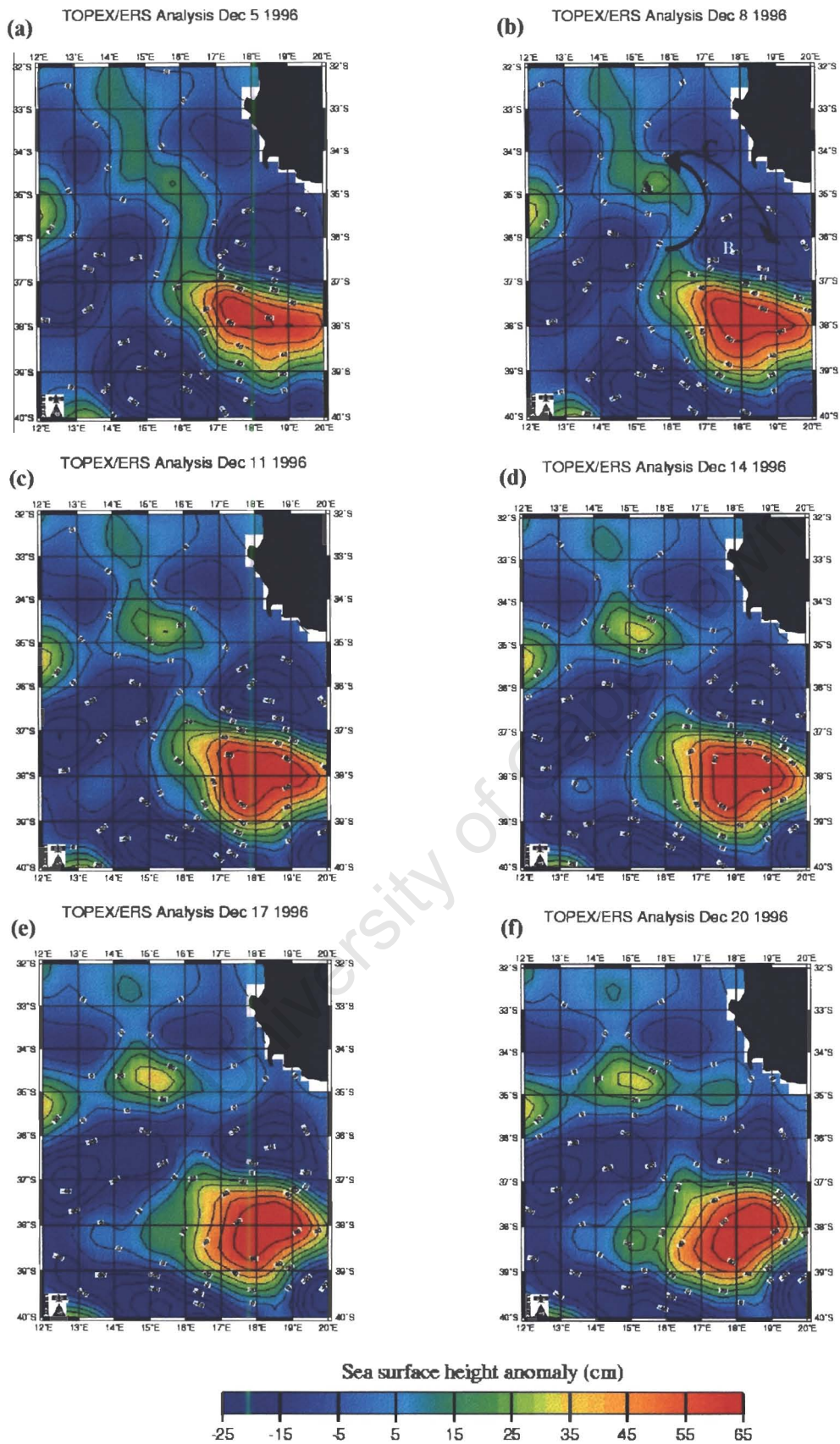


Figure 6.9: Sequence of SHA images from the CCAR altimetry website.
 (<http://www-ccar.colorado.edu>)

preceding the generation of an altimetry image will result in a less reliable representation of SHA. These situations of poor satellite coverage do not occur often and the CCAR altimetry images have successfully been used at UCT (The University of Cape Town) to track other mesoscale features (Agulhas rings).

Fortunately the rest of the images in *Figure 6.9* have been constructed from the data sampled during a period of good coverage of the represented region by the respective satellites. It is thus feasible to track the features of interest, identified in the South-east Atlantic during early December 1996, on the rest of the altimetry imagery. The variation/development of three structures near the retroflexion region is relevant to the interpretations gleaned from the AVHRR imagery. These structures are marked **A**, **B** and **C** on *Figure 6.9(b)*.

Except for the elevated region identified at $15.8^{\circ} \text{ E} / 34.8^{\circ} \text{ S}$ (marked **A**) on 8 December 1996 in *Figure 6.9(b)*, there is very little evidence of movement of any of the other features in the sequence of altimetry imagery. Feature **A** can be identified as the expanded northern region of the anticyclonic feature (**A**) observed in *Figure 6.5*. The altimetry indicates that the Agulhas ring has already occluded and the annulus shape identified in the SST (*Figure 6.5*) is thus a consequence of multiple filament interaction between the ring and the Agulhas Current. This feature shows continual growth and westward movement throughout the sequence and represents the translation of an Agulhas ring.

Two black arrows (*Figure 6.9(b)*) mark the paths of the filaments, **F1** and **F2**, as observed in *Figure 6.5*. Here the presence of feature **B** ($18^{\circ} \text{ E} / 36.1^{\circ} \text{ S}$) aids in shedding some light upon the direction in which filaments are moving, to and from the Agulhas ring. This depression (**B**), representing cyclonic flow, allows one to determine the preferential directions of flow associated with the filaments. Flow direction is indicated by the arrow heads. The cyclone (**B**) persists in this region throughout the altimetry sequence. Its presence can be noted up to 13 December 1996 in the SST imagery (*Figure 6.7*), because the positions of the filaments (**F1** and **F2**) and their flow directions agree well with the expected flow around the cyclone identified in *Figure 6.9(d)*, centred at $18.2^{\circ} \text{ E} / 36.2^{\circ} \text{ S}$.

A much clearer indication of a small cyclone centred at 16.8° E / 33.8° S has been identified as feature **C** on *Figure 6.7*. This feature has a very close association with the Agulhas ring on the SST imagery, but cannot be unambiguously identified in the altimetry sequence of *Figure 6.9*. The change of orientation of feature **C** (*Figure 6.9(b)*) throughout the altimetry sequence, from 4 December 1996 to 20 December 1996, does show a westward progression of depressed SHA accompanying the westward translation of the Agulhas ring. However, the region of depression (**C**) identified on the altimetry is a large feature making it difficult to associate this relatively large feature with the small cyclone identified on the SST. Their association is significant despite this reservation, because the resolution that can be obtained from altimetry data complicates the identification of smaller features. The general location and westward development of this depression is therefore a reasonable confirmation from the altimetry of the cyclone(**C**) identified in the SST (*Figure 6.7*).

It is clear from the above analysis that the altimetry data supports and augments the interpretations gained from the AVHRR imagery. The collaboration of these two sources allows one to establish that a northerly meander of the Agulhas Current in the retroflexion region formed a dipole configuration in association with an adjacent cyclone situated directly east of this meander in early December 1996. This meander occluded to form an Agulhas ring that had multiple filament interactions with the retroflexion region due to the presence of the adjacent cyclone. As the Agulhas ring moved away from the retroflexion region a secondary cyclone developed to the north-east of the ring and the two features exhibit a combined westward translation. Thus the Agulhas ring forms the primary partner in a dipole vortex system.

Discussion

The combination of AVHRR and altimetry imagery presents the intricate life history of an Agulhas ring from its origin at the Agulhas retroflection region to its role as primary vortex in a vortex dipole in the South-east Atlantic.

In the early stages of the ring's development, it forms part of a mushroom configuration budding off from the Agulhas retroflection (*Figure 6.1*). As mentioned before (Chapter 2), mushroom-like patterns are more likely to result from the immature, or generation stages of a dipole and its tracer advection (*Mied et al., 1991*). The presence of a dipole configuration is supported by the altimetry imagery of early December 1996 (*Figure 6.8*). The next step would be to determine which components constitute the dipole/mushroom configuration. As the Agulhas Current flows past Port Elizabeth and encounters the Agulhas Bank, significant meandering behaviour is observed routinely (*Lutjeharms, 1981a; Schumann and Van Heerden, 1988*). *Lutjeharms et al. (1989)* also demonstrated that shear edge features are nearly always present in the inshore border of the Agulhas Current as it flows past the Agulhas Bank and that cyclonic eddies may form in the lee of meanders extracting plumes from the current. On 4 December 1996, there is no complete Agulhas ring visible on either the AVHRR or the altimetry imagery. A meander of the Agulhas Current protruding northward from the retroflection loop was evident and it formed the anticyclonic part of the mushroom configuration. The cyclonic eddy was situated in the lee of the meander and drew a filament off the eastward edge of this meander. Thus the mushroom configuration was a combination of a meander in the Agulhas Current, a cyclonic eddy in the lee of this meander and the filament extracted from the current by the eddy.

Recent modelling experiments of the Agulhas retroflection region shed some light on the genesis of cyclonic eddies off the western Agulhas Bank. *Penven et al. (2000)* used a model with a high spatial resolution for the southern Agulhas Current in order to see if it might simulate the origin and development of cyclonic eddies found in the South-east Atlantic. The model gave a realistic portrayal of the known circulation in this ocean region. Cyclonic eddies were found to be prevalent between the Agulhas Current and the western side of the Agulhas Bank in the model. Hydrographic information, covering such a cyclonic eddy in November 1992, was used by the authors to compare with model

results and they established good consistency between model results and observations. These numerical results could then be used to explore the origins of the cyclonic eddies and it was found that the generation of cyclones past the Agulhas Bank can be explained by a flow detachment process.

Previous altimetry observations of the Agulhas retroflection also suggested the presence of a dipole structure west of the Agulhas Bank. *Gründlingh (1995)* observed a vortex dipole south-west of the Agulhas Bank when he examined TOPEX/POSEIDON altimetric snapshot imagery in conjunction with NOAA AVHRR imagery for early November 1992. On the AVHRR imagery the Agulhas Current was seen to meander in a south-westerly direction to 16°-17°E, where a dipole-like branch protruded northward from the main current, while the latter turned southward and then eastward. These observations compare very well with *Figure 6.1* and the same similarities were also found when comparing the altimetry observations of early December 1996 and early November 1992.

A sudden shift in the position of maximum SHA is noted on the following altimetry image (*Figure 6.9(a)*), but not so in the AVHRR imagery. The altimetry observations lead the same expected features, on the AVHRR imagery. Although *Gründlingh (1995)* found good agreement between the features identified in the AVHRR imagery and their positions on the altimetry imagery, he did explain that the topographic contours may distort the flow as portrayed in the satellite image, because of the various “errors” that are introduced in the topographic representation (contouring and gridding technique, satellite line spacing, loss of steady flow, etc.). Overpass information for the two satellites for December 1996 is presented in *Appendix II*. This information made it possible to determine that there was good coverage of the South-east Atlantic region associated with most of the altimetry images produced for this time period. It is also important to bear in mind that the AVHRR imagery has a finer resolution than that of the altimetry imagery. Therefore, although the general picture presented by the two media is similar, the altimetry imagery might represent a more distorted view of the actual oceanographic regime that is smaller than mesoscale phenomena, whereas AVHRR imagery can resolve sub-mesoscale phenomena very reliably.

By 7 December 1996 it was obvious that the meander was occluding into an Agulhas ring. The filament extracted from the ring by the cyclonic eddy is recirculated to the Agulhas Current, whereas the ring is “fed” by a filament attached to the Agulhas retroflection region. At this stage there is closer agreement between the two sources of satellite imagery and the altimetry suggests that the anticyclonic section of the original mushroom/dipole configuration is moving away from the retroflection region in a northerly direction, independently of the cyclonic feature (*Figure 6.9(b)*). Northward translation of the cyclonic eddy would be blocked by the proximity of the Agulhas Bank to the northeast and the anticyclonic eddy to the northwest. This is consistent with the conclusion of *Byrne et al. (1995)* that steep topography influences eddy trajectories and translation speeds.

A continual expansion of the area of maximum SHA representing the Agulhas ring on the altimetry image of 11 December 1996 (*Figure 6.9(c)*), echoes the growth of the ‘bulb-like’ region on the AVHRR image of the previous day (*Figure 6.6*). The core of the Agulhas ring is thus growing and intensifying as more Agulhas Current water is being drawn into the ring. An interesting observation is that of the cyclonic coil at approximately $16.6^{\circ}\text{E}/34.4^{\circ}\text{S}$ on *Figure 6.6*, signifying the start of a cyclonic eddy forming just west off the shelf edge. There is some support for this observation in the altimetry as the region of depression north-west of the Agulhas ring exhibits westward translation. The proximity of the boundary prevents the northward translation of the original cyclone identified as the secondary vortex of the dipole, but according to *Hooker and Brown (1994)* this situation will force straining of the cyclone as it is pulled through the gap between the anticyclone and the boundary. During the period of northward translation of the Agulhas ring, it becomes increasingly difficult to identify an accompanying secondary cyclonic vortex in the AVHRR imagery (*Figures 6.3 to 6.5*). Instead there is evidence of streaming and multiple filament expression in the region where the cyclonic eddy is expected to be. This observation is very similar to what *Hooker et al. (1995b)* described as the “filamentation phase” of the dipole structure of WCR 82-B in his analysis of the dynamics of this dipole (see *Figure 2.4 (d)*). Thus the cyclone has become partially elongated and filamentous as it is strained between the Agulhas ring and the Western Agulhas Bank.

The Agulhas ring continued to show significant growth on both sources of satellite imagery (*Figure 6.7 and 6.9(d)*). A little east and north of the anticyclonic eddy core, there is a small eddy with a cyclonic rotation signature, some evidence of closed circulation, and an indication of Benguela Current water entrainment in the eddy centre. This is a clear indication of dipole development and is also consistent with similar observations made by *Hooker et al. (1995b)* during their analysis of the “reformation phase” of the dipole nature of WCR 82-B. At this stage filament **F1** has a weaker surface expression than before, whereas filament **F2**, has a much stronger surface expression before the two filaments coalesce. The orientation of the dipole has also changed, so that orientation of the entrained filament between the two vortices is forced into an east-west direction, i.e. preferentially drawing water from the Agulhas Bank region.

Extensive cloud cover over the study area, due to the passage of a cold front from 14 to 18 December 1996, made it impossible to present good AVHRR imagery for feature tracking. On 19 December 1996 (*Figure 5.1*) it is clear that the dipole has translated westward and is directly drawing water from the Agulhas Bank and ‘leaking’ that Agulhas Bank water into the South Atlantic.

It is clear from the above interpretation of events occurring in the Southeast Atlantic oceanographic regime that various factors conspired to create the dipole surveyed by the F.R.S. *Africana* in December 1996.

- A large meander in the Agulhas Current was observed west of the Agulhas Bank.
- The meander and an eddy, in the lee of the meander, extracting a plume from the current, resulted in a mushroom-type configuration, which is a precursor to dipole vortex occurrence.
- The meander occludes and becomes an Agulhas ring, which translates away from the retroflection region in a northward direction.
- Because of the cyclonic eddy’s proximity to the Agulhas Bank, the initial dipole configuration is destroyed as the cyclone goes through a deformation and filamentation phase.
- West of Cape Town a new dipole configuration is initiated with an adjacent cyclone north-east of the Agulhas ring.
- This different orientation promotes the extraction of warm water directly from the Agulhas Bank into the south Atlantic.

- The water extracted from the Agulhas Bank follows two routes:
 - some flowing northward along the West Coast shelf in the shelf-edge jet, and
 - the rest being drawn offshore, between the two eddies into the oceanic region.

A significant influx of warm water onto the Agulhas Bank and the subsequent removal of this water, via a filament, by the dipole vortex, is evident in *Figure 1.2*. It is clear that the dipole vortex is responsible for the entrainment of the filament and hence the removal of Agulhas Bank water, but the initial origin of the warm water has yet to be explained. Earlier in this chapter mention has been made of shear-edge features of the Agulhas Current, which include meanders, eddies and plumes, that has been described by *Lutjeharms et al.* (1989). The authors found that amplitudes of current meanders grow downstream of Port Elizabeth, as do all dimensions of border plumes and eddies associated with them, and concluded that these features are found on the inshore boundary of the Agulhas Current as it flows past the Agulhas Bank. *Swart and Largier* (1987) have suggested that the cyclonic frontal eddies are responsible for forcing warm subtropical surface water onto the continental shelf of the Agulhas Bank. The large expanse of warm water ($>18^{\circ}\text{C}$) seen on the Agulhas Bank in *Figure 1.2* could be the result of plumes of warm water forced onto the Agulhas Bank by cyclonic eddies found in the lee of successive meanders in the Agulhas Current. Evidence is presented on *Figure 6.1* of the presence of one such meander, whereas a similar meander is seen on *Figure 1.2*. These meanders would have been initiated earlier along the eastern Agulhas Bank and progressed downstream where they become visible in the region of study relevant to this investigation. The conditions necessary for the forcing of warm plumes onto the Agulhas Bank thus existed in the days preceding *Figure 1.2*.

During this investigation, it was possible to establish that a dipole vortex did indeed develop at the Agulhas retroflection region in early December 1996. The dipole interacted with the shelf edge, as it underwent a filamentation and reformation phase, before it became orientated favourably for a circulation pattern which promoted the direct leakage of Agulhas Bank and Agulhas Current water into the South Atlantic Ocean.

Chapter 7

Conclusions

The results from this investigation provide an answer to the question, “Are rings in other current systems dipoles?”, posed by *Hooker and Brown (1995a)* after they had established the dipole nature of WCR 82-B. The shedding of a dipole vortex from the Agulhas Current retroflection region was identified from satellite imagery and subsequent interactions of the dipole vortex with the Agulhas Bank and its reformation west of Cape Town could be monitored during December 1996.

During the course of this investigation the following objectives were realised:

- **A descriptive analysis (from satellite and *in situ* evidence) was given of the hydrographic characteristics of a vortex dipole, which was encountered in the Southeast Atlantic and surveyed by the *F.R.S. Africana* during December 1996.**

There is *in situ* and satellite evidence indicating that the cyclonic eddy core was of Benguela Current (South-east Atlantic Ocean water) origin and that the anticyclonic eddy was of Agulhas Current origin. It was established from AVHRR imagery that the secondary vortex exhibited an anticlockwise rotation of 8.6°/day around the Agulhas ring and that the dipole exhibited an overall north-westward translation during the period of the cruise. A warm filament, of Agulhas Bank origin, was drawn between the two eddies and resulted in a pool of warm water to the north-west of the dipole vortex. The northward flowing component of the filament was the result of forcing by the West Coast shelf-edge jet.

- **A descriptive analysis of the origin and translation of the vortex dipole, from its formation at the Agulhas Current up to the time of the hydrographic survey, is achieved from the inspection of NOAA AVHRR imagery and TOPEX/POSEIDON and ERS-2 altimeter imagery.**

The development of the dipole can be followed on the sequence of AVHRR images in *Appendix III*. In early December 1996, a large meander in the Agulhas Current was

visible west of the Agulhas Bank. This meander combined with a cyclonic eddy, in the lee of the meander, to form a mushroom-type configuration recognisable on the sea surface temperature satellite imagery. The mushroom configuration was a precursor to dipole development and indicated the presence of an adjacent pair of circulatory features of opposing spin. An Agulhas ring occluded from the meander and exhibited a northward translation. As a result of this, the dipole configuration was destroyed as the cyclone underwent a filamentation phase due to the presence of the Agulhas Bank. The dipole was re-established west of Cape Town when the cyclone exhibited the reformation phase and the orientation of the dipole was changed so that a filament was directly drawn from the Agulhas Bank. This filament had two branches, one that was entrained between the two eddies forming a northward spreading plume, and another that flowed northward as part of the shelf-edge jet.

In order to achieve the successful interpretation of all the data used in this investigation, three sources of data had to be analysed, i.e. *in situ* hydrographic observations, AVHRR infra-red SST imagery and altimetry imagery. Any one of these sources used on its own would not have been adequate for sketching the genesis and maturation of this dipole vortex. During the course of this investigation, the limitations of the individual sources were exposed. Altimetry imagery sometimes represents a distorted view of the actual sea-surface height properties with respect to sub-mesoscale structures due to errors (contouring and gridding technique, satellite line spacing, loss of steady flow, etc.) that are introduced in the topographic representation. Surface temperature characteristics of features can only be recognised from AVHRR satellite imagery when the surface expression of that particular feature is embedded in a background of contrasting temperature properties. Cloud cover frequently presents a problem, obscuring large areas of the sea surface. It was also difficult to deduce flow directions from AVHRR images without the concomitant study of altimetry images. *In situ* measurements alone would not have been enough to establish the presence of this mature dipole structure inconclusively, due to the discrete nature of the horizontal water column measurements, as well as the time lapses between measurements. The sheer size of the vortex and rapid development thereof complicates effective *in situ* sampling and measurement of water column characteristics. These limitations are characteristic of the individual data sources however, and is not a reflection of the interpretation gleaned from their combined use.

The investigation into the oceanographic events occurring in the South-east Atlantic Ocean in early December 1996 conducted in this project has culminated in the description of the physical structure of an Agulhas dipole, the origin of the vortices at the retroflection region and their subsequent translation into the Cape Basin. This descriptive analysis naturally prompts the question:

What significant impact does the presence of a vortex dipole have on the oceanography of its immediate surroundings?

Indian Ocean Water enters the South Atlantic by both a ring-shedding process at the western end of the Agulhas Retroflection and through direct leakage via filaments and plumes from the Agulhas Current. This interocean exchange of heat and salt around South Africa is thought to be a key link in the maintenance of the global overturning circulation of the ocean (*De Ruijter et al., 1999*). Warm Agulhas rings are the most energetic ones shed from a western boundary current in the world ocean (*Olson and Evans, 1986; Goni et al., 1997*) and they act as a source of salt and kinetic and potential energy for the South Atlantic as they move into the Cape Basin (off south-eastern Africa). During their cross-Atlantic migration Agulhas rings interact with the ambient waters through various mixing processes, thus depositing their excess heat, salt and vorticity (*Arhan et al., 1999*). *Weijer et al. (1999)* have suggested that the location of the major input of interbasin products may be critical to the subsequent behaviour of the thermohaline circulation in the Atlantic Ocean. In an analysis of TOPEX/Poseidon altimetry *Schouten et al. (submitted)* have shown that rings lose more than half their energy in the first five months of their existence and about one third of all rings dissipate fully in the Cape Basin. The processes responsible for the rapid dissolution of these rings are not fully understood and scientists from the Institute for Marine and Atmospheric Research at Utrecht University (IMAU), the Netherlands Institute for Sea Research (NIOZ), the Royal Netherlands Meteorological Institute (KNMI), the University of Cape Town (South Africa) and the Free University (VU) are participating in the MARE (Mixing of Agulhas Rings Experiment) cruises which have been designed to study a specific Agulhas ring and the processes involved as it mixes with the ambient waters of the Cape Basin. More information about this project can be found at <http://www.nioz.nl/projects/mare/>.

During the course of this investigation into the origins of the dipole vortex observed in the South-east Atlantic in December 1996, various interactions of the Agulhas ring and its surrounding environment have been observed. The presence of the cyclone introduces secondary flows that enhance interaction between the ring, the current and quiescent South-east Atlantic water. These interactions are best depicted in *Figure 6.7* where the ring can be observed drawing a warm filament from the retroflection region, as an adjacent cyclone similarly draws a filament from the ring. Some of the water from the ring is thus “poached” by the cyclone and wrapped around its Benguela core water. Furthermore, a filament of cool South-east Atlantic water is swept between the Agulhas ring and the warm filament. Although the filament interactions are restricted mostly to the upper 100 m, the cyclonic eddy is significantly deep enough for a considerable amount of interaction between the central waters of the two eddies. In order to gauge the decay of all Agulhas rings, i.e. their contribution of heat and salt to the South Atlantic Ocean, an understanding of the degree and manner of mixing is crucial. The observations made during this investigation suggest that the presence of a cyclonic ringlet partner to an Agulhas ring will enhance the mixing of ring water with the surrounding Atlantic water. *Hooker and Brown (1994)* state that the proper calculation of ring energetics would need to be reconsidered when an anticyclone has a concomitant rotating cyclone partner, because the net angular momentum of the system will be reduced by the counterrotating companion. Thus a cyclonic partner would influence the decay of an Agulhas ring and a study of Agulhas ring mixing in the South-east Atlantic should include an investigation of any associated cyclonic ringlets encountered as well. It is possible that Agulhas rings previously described from AVHRR data could also have been dipoles, but their surface expressions were weak or unrecognisable because of the rapid heat loss to the atmosphere by rings as they move away from the retroflection region. An older eddy-pair would thus have similar sea surface temperature signals, only becoming recognisable on AVHRR images when surrounded by waters with a contrasting sea surface temperature signal (see *Figure 1.4*).

The unique circulation patterns that have resulted from the dipole presence leads one to wonder about the possible impact such an event could have upon the catch aspirations of the local fishing industries. It is possible to speculate upon the impact of the influx of warm water onto the Agulhas Bank, in conjunction with the removal

of this water from the Agulhas Bank, on Anchovy spawning. Cape Anchovy *Engraulis capensis* spawn serially on the western Agulhas Bank between September and February (Shelton, 1986; Melo, 1994). Their spawning products are then transported from the western Bank, around Cape Point and northwards along the West Coast to the recruitment grounds between St Helena Bay and the Orange River mouth (Hutchings, 1992). Previous work has suggested that anchovy prefer to spawn in temperatures between 16°C and 19°C (Shelton, 1986). Food availability is also important and on the western Agulhas Bank, copepods dominate the diet of anchovy (James, 1987). The conditions observed on the AVHRR image of 19 December 1996 (Figure 1.2) satisfy the temperature requirements, as well as promoting the continual presence of copepods on the western Agulhas Bank through the advection of the warm plumes from the east. These conditions would present an optimal spawning period for anchovy (Richardson et al., 1998).

The circulatory conditions induced by the presence of the dipole vortex are also conducive to the acceleration of spawning products, as well as their required diet products, to their recruitment grounds along the West Coast. A direct feed of the Agulhas Bank water into the coastal jet, west of the Cape Peninsula, is observed on 19 December 1996. The transport of warm water along the jet is visible up to the Cape Columbine region, which is the start of the recruitment grounds. Warm water is also recirculated by the cyclonic eddy towards the recruitment grounds. The combination of all these factors thus contribute to enhanced spawning success, as well as good recruitment of Anchovy during the latter half of December 1996. Adequate monitoring of these events for comparison with anchovy recruitment statistics is necessary for testing this hypothesis and could aid in the development of improved models for predicting anchovy catch quotas.

A study of historical AVHRR data of the retroflection region could lead to the discovery of more events such as the one described in this work and result in clearer insight into the genesis and subsequent development of vortex dipoles from the Agulhas retroflection region, as well as their role in the dispersal of heat and salt into the South Atlantic Ocean.

References

- Ahlnas, K., Royer, T.C., and T.H. George 1987 - Multiple dipole eddies in the Alaska Coastal Current detected with Landsat thematic mapper data. *J. Geophys. Res.* **92**(C12): 13,041-13,047.
- Arhan, M., Mercier, H. and J.R.E. Lutjeharms 1999 – The disparate evolution of three Agulhas rings in the South Atlantic Ocean. *J. Geophys. Res.* **104**(C9): 20,987-21,005.
- Armstrong, M.J. and R.M. Thomas 1989 – Clupeoids. In *Oceans of life off Southern Africa*. Payne, A.I.L. and R.J.M Crawford (Eds). Vlaeberg, Cape Town: 105-121.
- Bang, N.D. 1970a – Major eddies and frontal structures in the Agulhas Current retroflexion area in March, 1969. In *Proceedings of the Symposium on Oceanography in South Africa 1970*. Council for Scientific and Industrial Research: 16 pp.
- Bang, N.D. 1970b – Dynamic interpretations of a detailed surface temperature chart of the Agulhas Current retroflexion and fragmentation area. *S. Afr. Geogr. J.* **52**(12): 67-76.
- Bang N.D. 1973 - Characteristics of an intense ocean frontal system in the upwell regime west of Cape Town. *Tellus* **25**(3): 256-265.
- Bell, G.I. and L.J. Pratt 1992 – The interaction of an eddy with an unstable jet. *J. Phys. Oceanogr.* **22**: 1229-1244.
- Bennett, S.L. 1988 – Where three oceans meet: the Agulhas retroflexion region. Ph.D. thesis, Woods Hole; Massachusetts Institute of Technology / Woods Hole Oceanographic Institution: xxvii + 367 pp.

- Boudra, D.B. and E.P. Chassignet 1988 – Dynamics of Agulhas retroflection and ring formation in a numerical model. I. The vorticity balance. *J. Phys. Oceanogr.* **18**(2): 280-303.
- Boudra, D.B. and W.P.M. de Ruijter 1986 – The wind-driven circulation in the South Atlantic-Indian Ocean – II. Experiments using a multi-layer numerical model. *Deep-Sea Res.* **33**(4): 447-482.
- Boudra, D.B., Maillet, K.A. and Chassignet E.P. 1989 – Numerical modelling of Agulhas retroflection and ring formation with isopycnal outcropping. In *Mesoscale/Synoptic Coherent Structures in Geophysical Turbulence*. Nihoul, J.C.J and B.M. Jamart (Eds). Elsevier, Amsterdam: 315-335.
- Byrne, D.A., Gordon, A.L. and W.F. Haxby 1995 – Agulhas Eddies: a synoptic view using Geosat ERM data. *J. Phys. Oceanogr.* **25**(5): 902-917.
- Camp, D.B., Haines, W.E., Huber, B.A., Rennie, S.E. and A.L. Gordon 1986 – Agulhas Retroflection Cruise, November-December 1983. Hydrographic (CTD) Data. *Tech. Rep. Lamont-Doherty geol. Observatory LDGO-86-1*: 390pp.
- Chapman P., Duncombe Rae, C.M. and B.R. Allanson 1987 - Nutrients, chlorophyll and oxygen relationships in the surface layers at the Agulhas Retroflection. *Deep-Sea Res.* **34**(8A): 1399-1416.
- Chassignet, E.P. and D.B. Boudra 1988 – Dynamics of Agulhas retroflection and ring formation in a numerical model. II. Energetics and ring formation. *J. Phys. Oceanogr.* **18**(2): 304-319.
- Cheney, R., Miller, L., Agreen, R., Doyle, N. and J. Lillibridge 1994 – TOPEX/POSEIDON: The 2-cm solution. *J. Geophys. Res.* **99**(C12): 24,555-24,563.

- Cochrane, K.L. and L. Hutchings 1995 – A structured approach to using biological and environmental parameters to forecast anchovy recruitment. *Fish. Oceanogr.* **4**(2), 102-127.
- Cresswell, G.R. 1982 – The coalescence of two East Australian Current warm-core eddies. *Science* **215**(4529): 161-164.
- Darzi, M., Firestone, J.K., Fu, G., Yeh, E. and C.R. McClain 1991 – Current efforts regarding the SEAPAK Oceanographic Analysis Software System. *Proc. 7th Int. Conf. Interactive Process. Sys. Meteorol. Hydrol. Oceanogr.*: 109-115.
- Davey, M.K. and P.D. Killworth 1984 – Isolated waves and eddies in a shallow water model. *J. Phys. Oceanogr.* **14**: 1047-1064.
- De Ruijter, W.P.M., Biastoch, A., Drijfhout, S.S., Lutjeharms, J.R.E., Matano, R.P., Pichevin, T., van Leeuwen, P.J. and W. Weijer 1999 – Indian-Atlantic inter-ocean exchange: dynamics, estimation and impact. *J. Geophys. Res.* **104**(C9): 20,885-20,911.
- De Ruijter, W.P.M. and D.B. Boudra 1985 – The wind-driven circulation in the South Atlantic-Indian Ocean. 1. Numerical experiments in a one-layer model. *Deep-Sea Res.* **32**(5): 557-574.
- Duncan, C.P. 1968 – An eddy in the subtropical convergence southwest of South Africa. *J. Geophys. Res.* **73**(2): 531-534.
- Duncombe Rae, C.M. 1991 – Agulhas retroflection rings in the South Atlantic Ocean: an overview. *S. Afr. J. Mar. Sci.* **11**: 327-344.
- Duncombe Rae, C.M. 1994 – Agulhas retroflection rings in the South Atlantic Ocean. Ph.D. Thesis. Department of Physical Oceanography, University of Cape Town: x + 176 pp.

- Duncombe Rae, C.M., Shannon, L.V. and F.A. Shillington 1989 - An Agulhas ring in the South Atlantic ocean. *S. Afr. J. Sci.* **85**: 747-748.
- Duncombe Rae, C.M., Boyd, A.J. and R.J.M. Crawford 1992a – “Predation” of anchovy by an Agulhas ring: a possible contributory cause of the very poor yearclass of 1989. *S. Afr. J. Mar. Sci.* **12**: 167-173.
- Duncombe Rae, C.M., Shillington, F.A., Agenbag, J.J., Taunton-Clark, J. and M.L. Gründlingh 1992b – An Agulhas Ring in the South Atlantic Ocean and its interaction with the Benguela upwelling frontal system. *Deep-Sea Res.* **39**(11/12): 2009-2027.
- Evans, R.H., Baker, K.S., Brown, O.B., Smith, R.C., Hooker, S., Olson, D. and the Warm-Core Rings Program Service Office 1984 – Satellite images of warm-core ring 82-B sea surface temperature and a chronological record of major physical events affecting ring structure. *Scientific Report*. Warm-Core Rings Program Off., Woods Hole, Mass.: 25pp.
- Federov, K.N. and A.I. Ginzburg 1986 - “Mushroom-like” currents (vortex dipoles) in the ocean and in a laboratory tank. *Ann. Geophys.* **4**: 507-516.
- Feron, R.C.V., De Ruijter, W.P.M. and D. Oskam 1992 – Ring-shedding processes in the Agulhas Current system. *J. Geophys. Res.* **97**(C6): 9467-9477.
- Fine, R.A., Warner, M.J. and R.F. Weiss 1988 – Water mass modification at the Agulhas retroflection: chlorofluoromethane studies. *Deep-Sea Res.* **35**(3A): 311-332.
- Firestone, J.K., Fu, G., Darzi, M. and C.R. McClain 1990 – NASA’s SEAPAK Software for Oceanographic Data Analysis: An Update. *Proc. 6th Int. Conf. Interactive Inf. Process. Sys. Meteorol. Oceanogr. Hydrol.*: 260-267.
- Flierl, G.R. 1981 - Particle motions in large-amplitude wave fields. *Geophys. Astrophys. Fluid Dyn.* **19**: 39-74.

- Flierl, G.R. 1988 - On the instability of geostrophic vortices. *J. Fluid Mech.* **197**: 349-388.
- Flierl, G.R., Malanotte-Rizzoli, P. and N.J. Zabusky 1987 - Nonlinear waves and coherent vortex structures in barotropic beta-plane jets. *J. Phys. Oceanogr.* **17**: 1408-1438.
- Flierl, G.R., Stern, M.E. and J.A. Whitehead 1983 - The physical significance of modons: Laboratory experiments and general integral constraints. *Dyn, Atmos. Oceans* **7**: 233-263.
- Fuglister, F.C. 1972 - Cyclonic rings formed by the Gulf Stream 1965-66. In *Studies in Physical Oceanography 1*. Gordon, A.L. (Ed.). New York; Gordon and Breach: 137-168.
- Goni, G.J., Garzoli, S.L., Roubicek, A.J., Olson D.B. and O.B. Brown 1997 - Agulhas ring dynamics from TOPEX/POSEIDON satellite altimeter data. *J. Mar. Res.* **55**: 861-883.
- Gordon, A.L. 1985 - Indian-Atlantic transfer of thermocline water at the Agulhas retroflection. *Science* **227**(4690): 1030-1033.
- Gordon, A.L. 1986 - Inter-ocean exchange of thermocline water. *J. Geophys. Res.* **91**(C4): 5037-5046.
- Gordon, A.L. and W.F. Haxby 1990 - Agulhas eddies invade the South Atlantic: evidence from GEOSAT altimeter and shipboard Conductivity-Temperature-Depth survey. *J. Geophys. Res.* **95**(C3): 3117-3125.
- Gordon, A.L., Lutjeharms, J.R.E. and M.L. Gründlingh 1987 - Stratification and circulation at the Agulhas Retroflection. *Deep-Sea Res.* **34**(4): 565-599.

- Gordon, A.L., Weiss, R.F., Smethie, W.M. and M.J. Warner 1992 – Thermocline and intermediate communication between the South Atlantic and Indian Oceans. *J. Geophys. Res.* **97**(C5): 7223-7240.
- Gründlingh, M.L. 1979 – Observation of a large meander in the Agulhas Current. *J. Geophys. Res.* **84**(C7): 3776-3778.
- Gründlingh, M.L. 1988 – Two contra-rotating eddies of the Mozambique Ridge Current. *Deep-Sea Res.* **36**(1): 149-153.
- Gründlingh, M.L. 1995 – Tracking eddies in the southeast Atlantic and southwest Indian oceans with TOPEX/POSEIDON. *J. Geophys. Res.* **100**(C12): 24,977-24,986.
- Haidvogel, D.B., Beckman, A. and K.S. Hedstrom 1991 - Dynamical simulations of filament formation and evolution in the coastal transition zone. *J. Geophys. Res.* **96**(C8): 15,040-15,040.
- Harris, T.F.W. and N.D. Bang 1974 – Topographic Rossby waves in the Agulhas Current. *S. Afr. J. Sci.* **70**(7): 212-214.
- Harris, T.F.W., Legeckis, R. and D. van Foreest (sic) 1978 – Satellite infra-red images in the Agulhas Current System. *Deep-Sea Res.* **25**(60): 543-548.
- Harris, T.F.W. and D. van Foreest 1978 – The Agulhas Current in March 1969. *Deep-Sea Res.* **25**(5): 549-561.
- Helfrich, K.R., and U. Send 1988 - Finite amplitude evolution of two-layer geostrophic vortices. *J. Fluid Mech.* **197**: 331-348.
- Hendricks, J., Leben R., Born, G.H. and C. Kolinsky 1996 - EOF analysis of global TOPEX/POSEIDON data and implications for detection of global sea level rise. *J. Geophys. Res.* **101**(C6): 14,131-14,146.

- Hobson, D.D. 1991 - A Point vortex dipole model of an isolated modon. *Phys. Fluids A* **3**: 3027-3033.
- Hofmann, E.E., Hedstrom, S., Moisan, J.R., Haidvogel, D.B. and D.L. Mackas 1991 - Use of stimulated drifter tracks to investigate general transport patterns and residence times in the coastal transition zone. *J. Geophys. Res.* **100**(C8): 15,889-15,897.
- Hooker, S.B. and J.W. Brown 1994 - Warm core ring dynamics derived from satellite imagery. *J. Geophys. Res.* **99**(C12): 25,181-25,194.
- Hooker, S.B., Brown, J.W. and A.D. Kirwan Jr. 1995a - Detecting "dipole ring" separatrices with zebra palettes. *IEEE Trans Geosci. Remote Sens.* **33**: 1306-1312.
- Hooker, S.B., Brown, J.W., Kirwan Jr., A.D., Lindemann, G.J. and R.P. Meid 1995b - Kinematics of a warm-core dipole ring. *J. Geophys. Res.* **100**(C12): 24,797-24,809.
- Hutchings, L. 1992 - Fish harvesting in a variable, productive environment: searching for rules or searching for exceptions? In *Benguela Trophic Functioning*. Payne, A.I.L., Brink, K.H., Mann, K.H. and R. Hilborn (Eds). *S. Afr. J. mar. Sci.* **12**: 297-318.
- Ikeda, M. 1981 - Instability and splitting of mesoscale rings using a two-layer quasi-geostrophic model on an f -plane. *J. Phys. Oceanogr.* **11**: 987-998.
- Ikeda, M. 1991 - Wind-induced features in a coupled ice-ocean system. *J. Geophys. Res.* **96**(C3): 4623-4629.
- Ikeda, M. and W.J. Emery 1984 - Observations and modelling of satellite-sensed meanders and eddies off Vancouver Island. *J. Phys. Oceanogr.* **14**: 3-21.

- Ikeda, M., Mysak, L.A. and W.J. Emery 1984 – Observation and modelling of satellite-sensed meanders and eddies off Vancouver Island. *J. Phys. Oceanogr.* **14**: 3-20.
- James, A.G. 1987 - Feeding ecology, diet and field-based studies on feeding selectivity of Cape anchovy *Engraulis capensis* Gilchrist. In *The Benguela and Comparable Ecosystems*. Payne, A.I.L., Gulland, J.A. and K.H. Brink (Eds). *S. Afr. J. mar. Sci.* **5**: 673-692.
- Johannessen, J.A., Svensen, E., Sandven, S., Johannessen, O.M. and K. Lygre 1989 - Three-dimensional structure of mesoscale eddies in the Norwegian Coastal Current. *J. Phys. Oceanogr.* **19**: 3-19.
- Joyce, T.M. 1985 - Gulf Stream warm-core ring collection: An introduction. *J. Geophys. Res.* **90**: 8801-8802.
- Joyce, T., Backus, R., Baker, K., Blackwelder, P., Brown, O., Cowles, T., Evans, R., Fryxell, G., Mountain, D., Olson, D., Schlitz, R., Schmitt, R., Smith, P., Smith, R. and P. Wiebe 1984 – Rapid evolution of a Gulf Stream warm-core ring. *Nature* **308**: 1265-1287.
- Kamenkovitch, V.M., Koshlyakov, M.N. and A.S. Monin 1986 – *Synoptic eddies in the ocean*. Dordrecht; D. Reidel: ix + 433 pp.
- Kennelly, M.A., Evans, R.H. and T.M. Joyce 1985 - Small-scale cyclones on the periphery of a Gulf Stream warm-core ring 82B. *J. Geophys. Res.* **90**(C5): 8845-8857.
- Kloosterziel, R.C., Carnevale, G.F. and D. Phillippe 1993 - Propagation of barotropic dipoles over topography in a rotating tank. *Dyn. Atmos. Oceans.* **19**: 65-100.

- Largier, J.L., Chapman, P., Peterson, W.T. and V.P. Swart 1992 – The western Agulhas Bank: circulation, stratification and ecology. In *Benguela Trophic Functioning*. Payne, A.I.L., Brink, K.H., Mann, K.H. and R. Hilborn (Eds). *S. Afr. J. Mar. Sci.* **12**, 319-339.
- Larichev, V.D. and G.M. Reznik 1976 - Two-dimensional Rossby soliton: An exact solution. *Polymode News* **19**: 3.
- Legeckis, R. and A.L. Gordon 1982 – Satellite observations of the Brazil and Falkland currents – 1975 to 1976 and 1978. *Deep-Sea Res.* **29**(3A): 375-401.
- LillibrIDGE, J., Leben, R. and F. Vossepoel 1997 – Real-Time Altimetry from ERS-2. *Proc. 3rd ERS Symp., Florence, Italy, March 1997*.
- Lutjeharms, J.R.E. 1981a – Features of the southern Agulhas Current circulation from satellite remote sensing. *S. Afr. J. Sci.* **77**(5): 231-236.
- Lutjeharms, J.R.E. 1981b – Satellite studies of the South Atlantic upwelling system. In *Oceanography from Space*. Gower, J.F.R. (Ed.). Plenum, New York: 195-199.
- Lutjeharms, J.R.E. 1987 – Die Subtropiese Konvergensie en Agulhasretrofleksievaart (SCARC). *S. Afr. J. Sci.*, **83**: 454-456.
- Lutjeharms, J.R.E. 1996 – The Exchange of Water Between the South Indian and South Atlantic Oceans. In *The South Atlantic: Present and Past Circulation*. Wefer, G., Berger, W.H., Siedler, G. and Webb D.J. (Eds). Springer-Verlag, Berlin, Heidelberg: 125-162.
- Lutjeharms, J.R.E., Catzel, R. and H.R. Valentine 1989 – Eddies and other border phenomena of the Agulhas Current. *Continental Shelf Res.* **9**(7): 597-616.
- Lutjeharms, J.R.E. and J. Cooper 1996 – Inter-basin leakage through Agulhas Current filaments. *Deep-Sea Res.* **43**(2): 213-238.

- Lutjeharms, J.R.E., de Ruijter, W.P.M, Ridderinkhof, H., van Aken, H., Veth, C, van Leeuwen, P.J., Drijfhout, S.S., Jansen, J.H.F. and G-J. A. Brummer 2000 – MARE and ACSEX: new research programmes on the Agulhas Current System. *S. Afr. J. Sci.* **96**, 105-110.
- Lutjeharms, J.R.E. and A.L. Gordon 1987 - Shedding of an Agulhas ring observed at sea. *Nature* **325**(7000): 138-139.
- Lutjeharms, J.R.E. and C.P. Matthysen 1995 – A recurrent eddy in the upwelling front off Cape Town. *S. Afr. J. Sci.* **91**: 355-357.
- Lutjeharms, J.R.E. and H.R. Roberts 1988 – The Natal Pulse: an extreme transient on the Agulhas Current. *J. Geophys. Res.* **93**(C1): 631-645.
- Lutjeharms, J.R.E. and P.L. Stockton 1987 - Kinematics of the upwelling front off southern Africa. In *The Benguela and Comparable Ecosystems*. Payne A.I.L., Gulland, J.A. and K.H. Brink (Eds). *S Afr J Mar Sci* **5**: 35-49.
- Lutjeharms, J.R.E. and H.R. Valentine 1988 - Evidence for persistent Agulhas rings southwest of Cape Town. *S. Afr. J. Sci.* **84**(9): 781-783.
- Lutjeharms, J.R.E. and R.C. van Ballegooyen 1984 – Topographic control in the Agulhas Current system. *Deep-Sea Res.* **31**(11): 1321-1337.
- Lutjeharms, J.R.E. and R.C. van Ballegooyen 1988a – The retroflexion of the Agulhas Current. *J. Phys. Oceanogr.* **18**(11): 1570-1583.
- Lutjeharms, J.R.E. and R.C. van Ballegooyen 1988b – Anomalous upstream retroflexion in the Agulhas Current. *Science* **240**(4860): 1770-1772.
- Lutjeharms, J.R.E. and N.M. Walters 1985 – Ocean colour and thermal fronts south of Africa. In *South African Ocean Colour and Upwelling Experiment*, Sea Fisheries Research Institute. Shannon, L.V. (Ed.): 227-237.

- McCalpin, J.D. 1987 - On the adjustment of azimuthally perturbed vortices. *J. Geophys Res.* **92**(C8): 8213-8225.
- McCartney, M.S. 1977 – Subantarctic mode water. In *A Voyage of Discovery*. Angel, M. (Ed.). New York; Pergamon: 103-119 (Supplement to *Deep-Sea Res.*).
- McCartney, M.S. and M.E. Woodgate-Jones 1991 – A deep-reaching anticyclonic eddy in the subtropical gyre of the eastern South Atlantic. *Deep-Sea Res.* **38**(S1): S411-S443.
- McClain, C.R., Fu, G., Darzi, M. and J. Firestone 1992 – PC-SEAPAK Users Guide, Version 4.0. *NASA Tech. Memo 104557*. Natl. Space and Aero. Admin., Goddard Space Flight Center, Greenbelt, Md.
- McClain, E.P., Pichel, W.G. and C.C. Walton 1985 – Comparative performance of AVHRR-based multichannel sea surface temperatures. *J. Geophys. Res.* **90**(C6), 11,587-11,601.
- McWilliams, J.C. 1983 - Interactions of isolated vortices, II, Modon generation by monopole collision. *Geophys, Astrophys, Fluid Dyn.* **24**, 1-22.
- McWilliams, J.C. and G.R. Flierl 1979 - On the evolution of isolated non-linear vortices. *J. Phys. Oceanogr.* **9**: 1155-1182.
- Melo, Y.C. 1994 - Multiple spawning of the anchovy *Engraulis capensis*. *S. Afr. J. Mar. Sci.* **14**: 313-319.
- Mied, R.P. and G.J. Lindemann 1979 - The propagation and evolution of cyclonic Gulf Stream rings. *J. Phys. Oceanogr.* **9**, 1183-1206.
- Mied, R.P. and G.J. Lindemann 1982 - The birth and evolution of cyclonic Gulf Stream rings. *J. Phys. Oceanogr.* **12**: 213-230.

- Mied, R.P., Kirwan Jr., A.D. and G.J. Lindemann 1992 - Rotating modons over isolated topographic features. *J. Phys. Oceanogr.* **22**: 1569-1582.
- Mied, R.P., McWilliams, J.C. and G.J. Lindemann 1991 - The generation and evolution of mushroom-like vortices. *J. Phys. Oceanogr.* **21**: 1569-1582.
- Nilsson, C.S. and G.R. Cresswell 1981 - The formation and evolution of East Australian Current warm-core eddies. *Progr. Oceanogr.* **9**: 133-183.
- Nof, D. 1983 - On the migration of isolated eddies with application to Gulf Stream rings. *J. Mar. Res.* **41**: 399-425.
- Olson, D.B. 1980 - The physical oceanography of two rings observed by the Cyclonic Ring Experiment. Part II: Dynamics. *J. Phys. Oceanogr.* **10**(4): 514-528.
- Olson, D.B. 1991 - Rings in the ocean. *Annu. Rev. Earth planet. Sci.* **19**: 283-311.
- Olson, D.B. and R.H. Evans 1986 - Rings of the Agulhas Current. *Deep-Sea Res.* **33**(1): 27-32.
- Olson, D.B., Fine, R.A. and A.L. Gordon 1992 - Convective modification of water masses in the Agulhas. *Deep-Sea Res.* **39**(S1): S163-S181.
- Olson, D.B., Schmitt, R.W., Kenelly, M. and T.M. Joyce 1985 - A two-layer diagnostic model of the long-term physical evolution of Warm-Core Ring 82B. *J. Geophys. Res.* **90**(C5): 8813 - 8822.
- Ou, H.W. and W.P.M. De Ruijter 1986 - Separation of an inertial boundary current from a curved coastline. *J. Phys. Oceanogr.* **16**(2): 280-289.
- Pedlosky, J. 1979 - *Geophysical Fluid Dynamics*. Springer-Verlag, New York: 624pp.

- Penven, P., Lutjeharms, J.R.E., Marchesiello, P., Weeks, S.J. and C. Roy (submitted) – Generation of cyclonic eddies by the Agulhas Current in the lee of the Agulhas Bank. *Geophys. Res. Lett.*
- Peterson, W.T., Hutchings, L., Huggett, J.A. and J.L. Largier 1992 – Anchovy spawning in relation to the biomass and the replenishment rate of their copepod prey on the western Agulhas Bank. In *Benguela Trophic Functioning*. Payne, A.I.L., Brink, K.H., Mann, K.H. and R. Hilborn (Eds). *S. Afr. J. mar. Sci.* **12**: 487-500.
- Peterson, R.G. and L. Stramma 1991 – Upper-level circulation in the South Atlantic Ocean. *Progr. Oceanogr.* **26**: 1-73.
- Ring Group 1981 – Gulf Stream cold-core rings: their physics, chemistry, and biology. *Science* **212**(4499): 1091-1100.
- Pond, S. and G.L. Picard 1986 – *Introductory Dynamical Oceanography*. Pergamon Press Inc., New York, p. 73.
- Rintoul, S.R. 1991 – South Atlantic interbasin exchange. *J. Geophys. Res.* **96** (C2): 2675-2692.
- Richardson, A.J., Mitchell-Innes, B.A., Fowler, J.L., Bloomer, S.F., Verheye, H.M., Field, J.G., Hutchings, L. and S.J. Painting 1998 – The effect of sea temperature and food availability on the spawning success of the Cape anchovy *Engraulis capensis* in the southern Benguela. *S. Afr. J. mar. Sci.* **19**: 275-290.
- Robinson, I.S. and T. Guymer 1996 – Observing Oceans from Space. In *Oceanography: An Illustrated Guide*. Summerhayes, C.P. and S.A. Thorpe (Eds). Manson Publishing Ltd, London: 69-88.
- Rouault, M. and J.R.E. Lutjeharms 1994 – Air-sea interaction in the marine atmosphere boundary layer: a new South African research venture. *S. Afr. J. Sci.* **90**, 11-12.

- Roubicek, A.J., Garzoli, S.L., Richardson, P.L., Duncombe Rae, C.M. and Fratantoni 1998 – Benguela Current Experiment, R/V *Seward Johnson* Cruise SJ9705. *NOAA Data Rep.* ERL AOML-33, 215 pp., Atlantic Oceanogr. and Meteorol. Lab., Miami, Fla.
- Schouten, M.W., de Ruijter, W.P.M., van Leeuwen, P.J. and J.R.E. Lutjeharms (submitted) – Translation, decay and splitting of Agulhas rings in the south-eastern Atlantic ocean. *J. Geophys. Res.*
- Schumann, E.H. and I.L. Van Heerden 1988 – Observations of Agulhas Current frontal features south of Africa, October 1983. *Deep-Sea Res.* **35**(8A):1355-1362.
- Shannon, L.V. 1966 - Hydrology of the south and west coasts of South Africa. *Investl Rep. Div. Sea Fish. S. Afr.* **5**: 22 pp + 30pp of Figures.
- Shannon, L.V., Agenbag, J.J., Walker, N.D. and J.R.E. Lutjeharms 1990 – A major perturbation in the Agulhas retroflexion area in 1986. *Deep-Sea Res.* **37**(3): 493-512.
- Shannon, L.V. and D. Hunter 1988 – Notes on Antarctic Intermediate Water around Southern Africa. *S. Afr. J. Mar. Sci.* **6**: 107-117.
- Shannon, L.V., Lutjeharms, J.R.E. and J.J. Agenbag 1989 – Episodic input of Subantarctic water into the Benguela region. *S. Afr. J. Sci.* **85**(5): 317-322.
- Shannon, L.V. and G. Nelson 1996 – The Benguela: Large Scale Features and Processes and System Variability. In *The South Atlantic: Present and Past Circulation*. Wefer, G., Berger, W.H., Siedler, G. and D.J. Webb (Eds). Springer-Verlag Berlin Heidelberg: 163-210.
- Shelton, P.A. 1986 - Fish spawning strategies in the variable southern Benguela Current region. Ph.D. thesis, University of Cape Town: [vi] + 327 pp.

- Sheres, D., and K.E. Kenyon 1989 - A double vortex along the California coast. *J. Geophys. Res.* **94**(C4): 4989-4997.
- Shillington, F.A., Hutchings, L., Probyn, T.A., Waldron, H.N. and W.T. Peterson 1992 – Filaments and the Benguela frontal zone: offshore advection or recirculating loops? In *Benguela Trophic Functioning*. Payne, A.I.L., Brink, K.H., Mann, K.H. and R. Hilborn (Eds). *S Afr. J. mar. Sci.* **12**: 207-218.
- Signell, R.P. and W.R. Geyer 1991 - Transient eddy formation around headlands. *J. Geophys. Res.* **96**(C2): 2561-2575.
- Simpson, J.J. and R.L. Lynn 1990 - A mesoscale eddy dipole in the offshore California Current. *J. Geophys. Res.* **95**(C8): 13,009-13,022.
- Smith, D.C., IV and A.A. Bird 1991 - The interaction of an ocean eddy with an ice edge jet in a marginal ice zone. *J. Geophys. Res.* **96**(C3): 4675-4689.
- Smith, D.C., IV and G.P. Davis 1989 - A numerical study of eddy interaction with an ocean jet. *J. Phys. Oceanogr.* **19**: 975-986.
- Solomon, H. 1978 - Detachment and recombination of a current ring with the Kuroshio. *Nature* **274**: 580-581.
- Stern, M.E. 1975 - Minimal properties of planetary eddies. *J. Mar. Res.* **33**: 1-13.
- Stockton P. and J.R.E. Lutjeharms 1988 – Observations of vortex dipoles on the Benguela upwelling front. *S. Afr. Geogr.* **15**: 27-35.
- Swart, V.P. and J.L. Largier 1987 – Thermal structure of Agulhas Bank water. In *The Benguela and Comparable Ecosystems*. Payne, A.I.L., Gulland, J.A. and K.H. Brink (Eds). *S. Afr. J. mar. Sci.* **5**: 243-253.

- Thompson, B.J. and G.A. Gotthardt 1971 - Life cycle of a North Atlantic eddy (abstract). *Eos Trans. AGU* **52**: 241pp.
- Valentine, H.R., Duncombe Rae, C.M., Van Ballegooyen, R.C. and J.R.E. Lutjeharms 1988 – The Subtropical Convergence and Agulhas Retroflexion Cruise (SCARC) data report. *Rep. S. Afr. Coun. Scient. Ind. Res. T/Sea* **8804**: 10 pp. + tables + figures.
- Valentine, H.R., Lutjeharms, J.R.E. and G.B. Brundrit 1993 – The water masses and volumetry of the southern Agulhas Current region. *Deep-Sea Res.* **40**(6): 1285-1305.
- Van Heijst, G.J.F. and J.B. Flor 1989 - Dipole formation and collisions in a stratified fluid. *Nature* **340**, 212-215.
- Van Leeuwen, P.J., de Ruijter, W.P.M. and J.R.E. Lutjeharms 2000 – Natal Pulses and the formation of Agulhas rings. *J. Geophys. Res.* **105**(C3), 6425-6436.
- Walker, N.D. 1990 – Links between South African summer rainfall and temperature variability of the Agulhas and Benguela Current systems. *J. Geophys. Res.* **95**(C3): 3297-3319.
- Warm Core Rings Executive Committee 1982 – Multidisciplinary program to study warm-core rings. *Eos Trans. AGU* **63**: 834-836.
- Weijer, W., de Ruijter, W.P.M., Dijkstra, H.A. and P.J. van Leeuwen 1999 – Impact of interbasin exchange on the Atlantic overturning circulation. *J. Phys. Oceanogr.* **29**: 2266-2284.
- Yi, Y. 1995 - Determination of gridded mean sea surface from altimeter data of TOPEX, ERS-1, and GEOSAT. Ph.D. Thesis. Department of Geodetic Science and Surveying, The Ohio State University, Columbus, Ohio.

Appendix 7

The two-layer model

The calculations in the following discussion are based on a model of a ring consisting of two layers of fluid with different density. According to *Olson et al. (1985)* this type of model is commonly used in oceanography and meteorology. The application of this model allows for the use of the combined CTD and XBT temperature data set in order to determine ring characteristics.

The two-layer model is based on two layers of fluids of different densities $\rho_1 < \rho_2$. Differences in level (h) in the surface of the lower layer are adjusted by a reduced pressure $\delta p = (\rho_2 - \rho_1)gh$. Adjustment processes are then the same as if a reduced gravity $g' = g(\rho_2 - \rho_1)/\rho_2$ were acting. For Agulhas rings the interface in the two-layer model is approximated by a single thermocline isotherm in the ring and the pressure field set up by the deformation of the thermocline is given by $p = \rho g' h$, where h is the depth of an isotherm indicative of the thermocline.

The momentum balance for the radially symmetric flow in an idealised ring is between the centripetal acceleration, the Coriolis acceleration, and the pressure gradient at equilibrium. The azimuthal velocity in the ring is then approximated by the solution to the gradient balance relation

$$\frac{v^2}{r} + fv = g' \frac{\partial h}{\partial r}$$

where v denotes the azimuthal velocity, f the Coriolis parameter, and r the radius from the centre of the pressure distribution. Boundary conditions that $v = 0$ when $r = 0$ and $h = h_\infty$ when $r \rightarrow \infty$ are applied.

An empirical g' , depending on the accurate reproduction of the dynamic height structure in the ring, can be found by regressing the dynamic height versus the isotherm depth (*Olson et al., 1984; Joyce et al., 1984*). Following the example of *Olson et al. (1985)*, the regression of the depth of the 8°C to the 14°C isotherm with the geopotential anomaly relative to the 900db isobar (the deepest CTD and XBT data

available for all stations), was plotted for CTD stations 13 to 35 and XBT stations 2 to 34 of the cruise data. The result for the 10°C isotherm is

$$D_{900} = 0.0106h + 7.1822$$

It is useful to introduce a number of different scales that provides a baseline for the inter-comparison of different rings (*Olson, 1991*). These are the Rossby number, the Burger number and the Richardson number. A scaled version of the gradient velocity balance equation then assumes the form

$$(R_o)^2 + R_o = B'$$

where $R_o = \frac{U}{fL}$ is a Rossby number for gradient flow and $B' = g' \frac{\delta h}{f^2 L^2}$ is a Burger number for the interface displacement ($\delta h = h - h_\infty$) across the ring. The velocity (U) and length scale (L) are chosen to be the maximum velocity and the radius at which the maximum velocity occurs. This scaling relates the degree of non-linearity (or the departure from geostrophic balance) as

$$R_o = -1/2 \pm -1/2(1+4 B')^{1/2}$$

The Rossby number R_o here is positive for cyclonic flows and negative for anticyclonic flows. These dimensionless numbers can also be used to provide other interesting information about the rings.

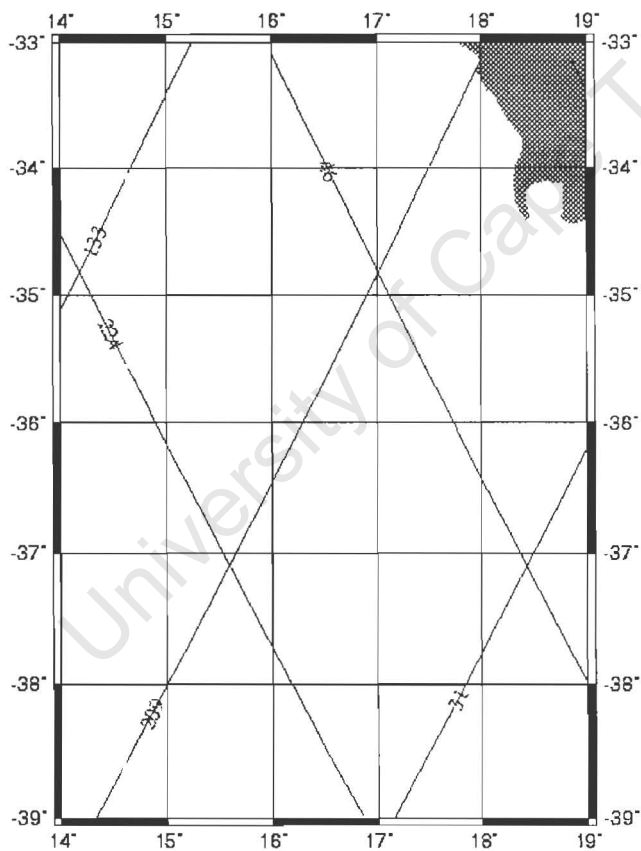
When the deviation of the interface height (indicated by the displacement Burger number B') is of the order of the interface depth (indicated by a traditional Burger number, $B = g' \frac{h}{f^2 L^2}$), i.e. $B' \approx B$, then the Richardson number, $R_i = g' \frac{h}{U^2}$, approximately represents the ratio of the potential energy to the kinetic energy of the ring (*Olson, 1991*). It is also useful to note that $B = R_i(R_o)^2$. In the two-layer model, the Rossby radius can be derived as $R_d = \frac{(g'h)^{1/2}}{f}$ which indicates the distance over which the gravitational tendency to flatten the free surface is balanced by the tendency of the coriolis acceleration to deform the surface (*Pedlosky, 1979*).

Appendix 99

Satellite Overpass Times corresponding to altimetry images used in this document:

TOPEX/Poseidon

TOPEX Repeat Groundtracks

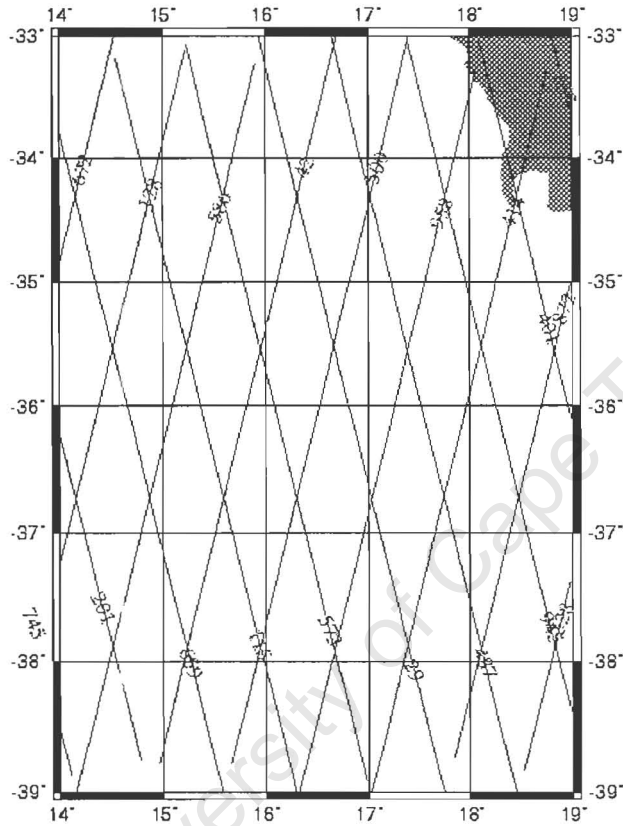


The following table contains overflight dates and times for *TOPEX cycle 155* to *TOPEX cycle 157*. Each set of latitude and longitude coordinates specify the location where each pass first enters the above plot. These coordinates also represent the positions that the overflight dates and times are for. Overflight times are accurate to within 10 seconds.

Pass number	Longitude	Latitude	Date			Time (GMT)		
			Cycle 155	Cycle 156	Cycle 157	Cycle 155	Cycle 156	Cycle 157
31	17.1358	-39.0302	29/11/96	09/12/96	19/12/96	08:11:56	06:10:28	04:08:59
46	16.5369	-34.0249	29/11/96	09/12/96	19/12/96	22:40:26	20:38:58	18:37:09
133	13.7557	-35.5151	03/12/96	13/12/96	23/12/96	07:47:06	05:45:38	03:44:09
209	14.2303	-39.1356	06/12/96	16/12/96	26/12/96	06:58:06	04:56:38	02:55:09
224	13.9139	-34.3818	06/12/96	16/12/96	26/12/96	21:26:46	19:25:18	17:23:49

ERS-2

ERS-2 Repeat Groundtracks



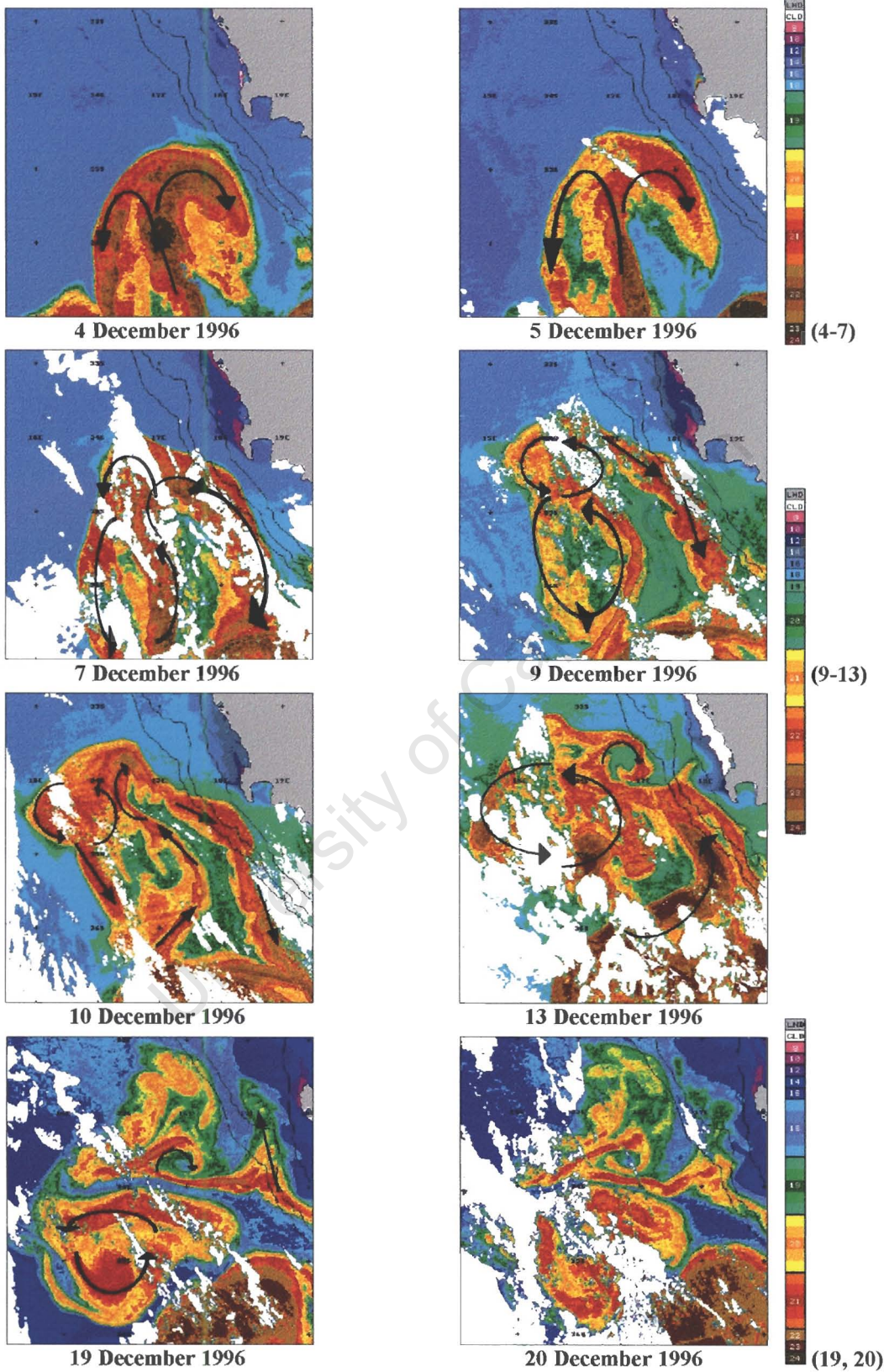
The following table contains overflight dates and times for *ERS-2 cycle 17*. Each set of latitude and longitude coordinates specify the location where each pass first enters the above plot. These coordinates also represent the positions that the overflight dates and times are for. Overflight times are accurate to within 10 seconds.

Pass number	Longitude	Latitude	Date	Time (GMT)
29	17.8206	-39.2425	26/11/96	21:46:53
42	17.7171	-32.9083	27/11/96	09:01:03
115	16.3141	-39.0436	29/11/96	21:52:43
128	15.2184	-33.1119	30/11/96	09:06:53
201	14.7811	-38.7559	02/12/96	21:58:33
214	13.8627	-32.8172	03/12/96	09:12:33
328	19.2512	-36.4938	07/12/96	08:47:43
401	19.1267	-36.5544	09/12/96	21:39:03
414	18.7636	-33.2620	10/12/96	08:52:33
487	18.5120	-39.1870	12/12/96	21:44:03
500	17.4237	-32.9150	13/12/96	08:58:13
573	16.9938	-38.9324	15/12/96	21:49:53
586	15.8964	-33.2318	16/12/96	09:04:03
659	15.6385	-39.1825	18/12/96	21:55:33
672	14.5490	-32.9253	19/12/96	09:09:43
745	14.1074	-38.8836	21/12/96	22:01:23
786	19.1919	-39.0023	23/12/96	08:45:33
859	19.2727	-34.6118	25/12/96	21:36:43
872	19.2662	-34.0481	26/12/96	08:49:53
945	19.1547	-38.9080	28/12/96	21:41:33
958	18.0578	-33.2696	29/12/96	08:55:23

The above information was obtained from the Colorado Centre for Astrodynamics Research Satellite Altimeter Groundtrack Program at:

<http://www-ccar.colorado.edu/~hendricj/gtrack.html>

Appendix 999



Sequence of high resolution AVHRR SST images depicting the genesis and translation of a vortex dipole from the Agulhas Retroflection region.